Magnetotransport Studies of Metal-Organic Molecule-Metal Structures: Electronic Transport Through Molecular Films of Alkanedithiols and Valence Tautomers

William Charles Rice

A dissertation submitted to the faculty of the University of North Carolina at Chapel Hill in partial fulfillment of the requirements for the degree of Doctor of Philosophy in the Department of Physics.

Chapel Hill, North Carolina
2012

Approved by:

Professor Frank Tsui

Professor Wei You

Professor Jianping Lu

Professor Yue Wu

Professor Rene Lopez

©2012
William Charles Rice
ALL RIGHTS RESERVED

ABSTRACT

WILLIAM CHARLES RICE: Magnetotransport Studies of Metal-Organic Molecule-Metal Structures: Electronic Transport Through Molecular Films of Alkanedithiols and Valence Tautomers
(Under the direction of Professor Frank Tsui)

Considerable recent research interest has focused on developing molecule-based device structures for spintronics applications. In addition to having long lifetimes of the electron spin which make them ideal for spintronics, molecules offer the possibility for synthetically customizing their properties to suit device requirements. Integrating molecules into architectures which can exploit these controllable properties, understanding intrinsic transport and magnetotransport within the molecules, and manipulating interfaces are the current challenges in the field.

In the first part of this project, the technique of nanotransfer printing (nTP) with polymer stamps was used to print Au thin film electrodes onto self-assembled monolayers (SAMs) of alkanedithiols, carbon chains with sulfur-based thiol end groups. A systematic study was conducted to determine the dependence of transport properties on the length of the alkane chains and the area of the printed Au electrodes. Current−voltage (I−V) curves analyzed with the Simmons model determined the height of tunneling barrier associated with the molecule (alkane) to be 3.5 ± 0.2 eV with an upper bound of 2.4 eV for the counterpart at the interface (thiol). The former is consistent with the theoretical value of

∼3.5−5.0 eV. The results demonstrated that nTP is a promising technique for producing scalable and permanent metal-molecule-metal junctions for molecule-based electronics.

In the second part of this research, cobalt-based valence tautomers (VTs), which have two distinct stable magnetic forms that can be switched as a function of temperature and light, were studied for their magnetotransport behaviors. The molecules were spin-coated to form the spacer layer of a spin valve which showed a magnetoresistance (MR) effect controlled by the tautomeric switching behavior. The effective switching on or off of the MR, corresponding to the anti-parallel magnetization state of the spin valve, was observed to undergo a pronounced shift as a function of the magnetic field strength, correlating to the reported tautomeric temperature transition between 150K and 180K. Additionally, asymmetries in the MR as a function of both magnetic field sweep direction and voltage bias direction demonstrate that the VT has a bias direction-dependent spin-polarization, a novel result that makes it suitable for use in a multi-state memory component.

ACKNOWLEDGEMENTS

I am thankful for the help and support of many amazing people. First, I would like to thank my advisor, Professor Frank Tsui, for his guidance in this research. His knowledge and recognition of the relevant landmarks helped me to find an oasis in an uncharted, barren terrain. I am especially grateful for the time he spent with me perfecting our methods and techniques. With his help I was able to greatly expand my knowledge and develop a greater appreciation for the subtleties and details required in research.

I would also like to thank my committee: Professors Wei You, Yue Wu, Rene Lopez, and Jianping Lu for their efforts in making this research come together.

I extend thanks to our collaborators in the National Science Foundation Center for Molecular Spintronics which provided funding for this work. In particular, thanks to Prof. David Shultz and Dr. Rob Schmidt for introducing me to the valence tautomer. I enjoyed working with them on this project spanning the Research Triangle. Other members of the collaboration I wish to thank are Profs. Marco Buongiorno-Nardelli, Dan Dougherty, Joe Tracy, as well as Daniel Stasiw, Geoff Lewis, and Alex Pronschinske. Also, thanks to Kevan Julye for helping me in the lab in the summer of 2011.

Additional thanks to current and former members of the Tsui group: Dr. Liang He, Dr. Brian Collins, Matt Wolboldt, Derek Vermeulen, Mark Moog, Jeff Haller, David Harris, Michelle LaBrecque, Mitchell Cobb, Andy Fuller, Alex Mellnik, Dmitry Spivak, Corey Konold, and Robert Call.

Also, I would like to specifically thank Professor Wei You for his excellent efforts in advancing our collaboration on campus at UNC in working with alkanedithiols. Special thanks to other members of our collaborative team in the You Group at UNC: Especially to Dr. Jeremy Niskala for his research on alkanedithiol self-assembled monolayers which is included in this work. Thanks for Dr. Paul Hoertz for his efforts in the collaboration in 2007-2009. Also thanks to graduate students Robert Bruce, Travis LaJoie, Josh Yablonski, Yanni Jie, Peng Dai, and Andrew Stuart.

Thanks to Dr. Hayden Black for his assistance with spin-coating and discussions about OFET techniques. Also thanks to Dr. Kwan Skinner for his advice on preparing photolithographic substrates.

Also, acknowledgements to the Chapel Hill Area Nanofabrication Laboratory (CHANL) for the use of equipment that made this research possible: Drs. Carrie Donley, Bob Geil, Amar Kumbhar, and Wallace Ambrose.

Additional thanks to members of the Lopez lab: Drs. John Tumbleston, Abay Dinku, Kristen Alexander, Rudresh Ghosh, Emily Ray, and Yingchi Liu. Thanks to the Lopez lab for the use of their equipment and also especially for the use of the glovebox.

I would also like to thank members of the Wu group: Drs. BJ Anderson and Magdalena Sandor for their friendship and encouragement.

I would also like to thank my family: To my parents, Coleman and Nancy Rice, and brother, Coley Rice, thank you for always being there for me. Thanks to my children, Charles and Sonia, for their smiles and their patience.

Finally, I wish to thank my wife, Meghan. Without you, none of this would have been possible. Thank you for your unwavering support and dedication through the good times and the tough times. You have made every day a better day for me.

TABLE OF CONTENTS

LIST OF TABLES xi

LIST OF FIGURES xii

Chapter I: Introduction and Motivation 1

I.1. Introduction to Spintronics 1

I.2. Introduction to Molecular Electronics 11

I.3. Molecular Spintronics 12

I.3.a) Introduction 12

I.3.b) Organic Semiconductors 13

I.3.c) Considerations in Making Devices from Organic Semiconductors 14

I.3.d) Molecular Spin Valves 19

I.4. Organization of this Work 21

I.4.a) Alkanedithiols 22

I.4.b) Cobalt-based Valence Tautomers 23

References 25

Chapter II: Preparation Procedures and Experiments 28

II.1 Alkanedithiol Self-Assembled Monolayer Sample Preparation 28

II.2 Valence Tautomer Sample Preparation 33

II.3 Conducting Atomic Force Microscopy (cAFM) Measurements 42

II.4 Probe Station Measurements 44

II.5 Low-Temperature and Vacuum Magnetotransport Measurements 46

System I: Joule-Thomson Cooling Chamber 46

System II: Liquid Flow Cryostat 49

II.7 Magneto-Optic Kerr Effect (MOKE) Experiment 51

References 54

Chapter III: Tunneling through Alkanedithiol Self-Assembled Monolayers 55

III.1. Introduction 55

III.2. Conducting Atomic Force Microscope Study of Molecular Tunnel Junctions made with Nanotransfer Printed Electrodes 57

Monolayer and nTP Characterization 57

III.3. Dependence of Tunneling Characteristics on Molecular Length 60

III.4. Simmons Modeling of I-V Behavior 61

Statistical approach for Simmons model fits 63

Results from the Simmons Model 69

III.5. Dependence of Tunneling Characteristics on the Area of the Printed Au Electrode 77

III.6. MOKE measurements of Metal-Molecule- Metal Junctions made with Ferromagnetic Metals 87

III.7. Conclusion 88

References 91

Chapter IV: Valence Tautomeric Switching Behavior in a Spin Valve 95

IV.1. Review of Valence Tautomer Properties and Characteristics 96

IV.2. Structure of Spin-valves made with Valence Tautomers 99

Optimization of Spincoating Procedure for making Valence Tautomer Thin Films 101

Magnetoresistive Effects Observed in Co-VT-Py Junctions 103

IV.3. Valence Tautomeric Switching Behavior in a Spin Valve 108

IV.4. Results and Discussion of Valence Tautomeric Switching 123

Spin Rectification 131

IV.5. Parallel Resistors Model 131

IV.6. I-V Measurements at Specific Magnetic Configurations 145

IV.7. Discussion of Results from I-V Measurements 145

IV.8. Light Effect 160

IV.9. 4K Behavior 162

Chapter V: Summary and Conclusion 170

V.1. Alkanedithiols 170

V.2. Cobalt-based Valence Tautomers 171

References 174

LIST OF TABLES

III.1. Summary of tunneling parameters…….76

IV.1. Rectifying Logic Table……129

LIST OF FIGURES

Figure I-1. Density of States Diagrams 6

Figure I-2. Diagrams of Magnetoresistance 10

Figure I-3. Energy Band Diagram of a Metal-Molecule Interface 18

Figure I-4. Metal-Molecule Interface Hybridization 20

Figure II-1. Nanotransfer Printing Method 30

Figure II-2 Cross-section view of photolithographic nTP sample 32

Figure II-3. Valence Tautomer Sample Structure 33

Figure II-4. Circuit Diagram for 4-terminal Measurements 44

Figure II-5. Experimental Set-up for the Magneto-Optic Kerr Effect (MOKE) 50

Figure III-1. Images of nTP arrays of Au-decanedithiol-Au junctions 58

Figure III-2. Representative I-V curves taken by cAFM 58

Figure III-3. Characteristic I-V behavior 60

Figure III-4. Statistical distributions of Simmons model parameters 65

Figure III-5. Example of statistical distributions of Simmons model fits 67

Figure III-6. Results of Simmons analysis 70

Figure III-7. Schematic diagrams of alkanedithiol monolayers on Au 72

Figure III-8. Tunneling exponent versus the length of the alkane chain 73

Figure III-9. Dependence of tunneling current on nTP contact size 77

Figure III-10. Dependence of zero-bias resistance R0 on the area of the nTP pads 79

Figure III-11. Lognormal distributions of zero-bias resistance (R0) for MMM junctions at various pad sizes 80

Figure III-12. Distributions of log of zero-bias resistance (R0) for Au/decanedithiol/Au tunnel junctions versus nTP pad sizes with the pads made using two different types of stamps 81

Figure III-13. Characteristic surfaces of various transfer printed features 86

Fig. IV-1 Diagram showing the energy potential wells corresponding to the two bistable forms of a valence tautomer molecule 96

Fig. IV-2 Magnetic tunnel junction of Co-VT-permalloy 98

Fig. IV-3 Molecular structure of the two forms of the cyanopyridyl valence tautomer 99

Fig. IV-4 Histograms showing variations in resistance values as a function of concentration of VT in dichloromethane 101

Fig. IV-5 Plot of TMR vs. magnetic field for sample CC38 103

Fig. IV-6 Plot of resistance vs. field along with MOKE data for the individual ferromagnetic electrode layers (sample CC38) 104

Fig. IV-7 Plots of differential resistance (dI/dV) showing an example of negative magnetoresistance 106

Fig. IV-8 Magnetotransport scan at 200K. 111

Fig. IV-9 Magnetotransport scan at 80K (Bias= ±10mV, ±20mV). 112

Fig. IV-10 Magnetotransport scan at 80K. (Bias= ±30mV, ±40mV). 113

Fig. IV-11 Magnetotransport scan at 80K. (Bias= ±50mV, ±60mV). 114

Fig. IV-12 I-V curve (green) and differential conductance (purple) for sample CC149 at 200K. 116

Fig. IV-13 Temperature dependence of differential resistance for sample CC149. 117

Fig. IV-14 Comparison of the scaled differential resistance vs bias for separate cooling runs. 119

Fig. IV-15 Plot of resistance vs. temperature, including resistance for the parallel and anti-parallel magnetizations for sample CC38 121

Fig. IV-16 Plot of MR vs. temperature for sample CC38 122

Fig. IV-17 Change in magnetic susceptibility times temperature plotted versus temperature for a variety of valence tautomeric crystals 123

Fig. IV-18. Comparison of the magnetic switching fields observed at temperatures of 200K and 80K - on either side of the valence tautomeric transition (150K) 126

Fig. IV-19. Comparison of the magnetic switching fields observed at temperatures of 200K and 80K 128

Fig. IV-20. Temperature-dependent shifts of the switching fields 129

Fig. IV-21. Mott parallel resistor model 132

Fig. IV-22. Parallel resistor model 133

Fig. IV-23 Schematic representation of observed spin rectification effect 139

Fig. IV-24 Difference in resistance values of parallel configurations of ferromagnetic electrodes during magnetotransport scans 140

Fig. IV-25 Diagram of results from the parallel resistors model with actual expected resistance values for the state MR21 141

Fig. IV-26 Schematic diagram of the extended parallel circuit. 143

Fig. IV-27 Results from 80K I-V measurements 146

Fig. IV-28 Results from 200K I-V measurements 147

Fig. IV-29 Model of MR versus bias for AP configurations of different magnetic field sweep directions 148

Fig. IV-30 Bias dependent shifting of the switching fields 150

Fig. IV-31 Upsweep at 200K. 152

Fig. IV-32 Plots of differences in differential conductance at 100K for AP configurations. 153

Fig. IV-33 Example of shifting of the switching field during the magnetic field downsweep 154

Fig. IV-34 MR data taken at 100K. 155

Fig. IV-35 I-V sweeps taken at 180K. 156

Fig. IV-36 MR data taken at 180K. 157

Fig. IV-37 Light experiment. 160

Fig. IV-38 MR data taken at 4K. 162

Fig. IV-39 MR data taken at 4K. 163

Fig. IV-40 I-V data from 4K. 164

Fig. IV-41 Possible scenarios in which the tautomer couples anti-ferromagnetically 166

Chapter I: Introduction and Motivation

I.1. Introduction to Spintronics

Spintronics is a rapidly developing area of current research exploring how to make use of the spin of the electron for information encoding in electronic devices. The additional degree of freedom offered by using the spin in electronic devices has many advantages. Devices can be made having lower power requirements, higher performance (e.g. by increased data processing speeds), and less heat dissipation. In addition, the use of spin allows for reduction of device size requirements which increases component densities for greater miniaturization. All of these factors are beneficial to meeting the future demands of a global economy where, as a result of becoming increasingly starved for resources, premiums will be placed on the efficiencies of electronic devices. When scales of production and consumption of these electronic devices reach large values, even small improvements to their efficiencies can have a significant impact. Thus, in addition to providing the obvious advantages of greater functionality and improved performance, the improvements offered by spintronics can reduce the potential for future crises by promoting economic stability.

Another promising aspect of spintronics is that by manipulating electron spin, devices can be made on the quantum level. This gives rise to quantum logic, and there is great promise for the development of quantum computers once spin manipulation is better

controlled. Quantum computers make use of quantum operations to perform calculations. Quantum states can be exploited in order to store information in quantum bits. Many operations can be performed simultaneously on many different states, unlike conventional digital computers. This allows for an orders of magnitude increase in computing power.

An even further advantage to using electron spin can is that memory elements can be made nonvolatile. Nonvolatile magnetically controlled memory elements retain their information even when power to the element has been turned off, unlike conventional transistor-based memories which require constant power to remain in a given informational or operational state. For computer memory, this has the appealing advantage that random access memory (RAM) would no longer need to be loaded from a separate, permanent media into the operating memory and then require power to be maintained there. Instead, using a spintronics-based magnetic random access memory (or MRAM) the information is already present and can be accessed immediately. Thus, there is a significant reduction in power consumption. This would eliminate the need to wait to "boot-up" when allowing memory to be filled while starting a computer, for example. Once the computer is running, there is no need for power to be spent to refresh the memory.

Other possibilities for improvements to existing computer architectures through spintronics can be developed by making reprogrammable logic, the so-called "logic-on-a-chip". Conventional logic devices that are combined to form a computer chip, such as AND, OR, NAND or NOR gates could be made from spintronics-based non-volatile components. If so, they would be able to have their logic operations changed from one type to the other by

the operating system in real-time. Subsequently they would stay in their new configurations indefinitely until reset or rechanged, ready to perform the newly programmed operation. This would greatly improve processing speeds, and the chip could even reconfigure itself to reach maximum possible speeds to meet a specific applications, for example. Thus, there would be an enormous flexibility in the range of applications that could be met by this type of chip.[1]

The research field of spintronics developed initially based on early discoveries made by Meservey and Tedrow on the nature of quantum tunneling of electrons between superconductors and ferromagnets[2], and by Julliere on magnetic tunnel junctions.[3] This was followed by the important discovery of giant magnetoresistance by Fert[4] and Grünberg[5], work for which they received the Nobel Prize in Physics in 2007. Giant magnetoresistance (GMR) is the change in the resistance to current flow through a stacked structure of magnetic thin films, brought about by manipulating the magnetic moments of the thin films. It occurs as a result of quantum-based spin scattering of the electric current.

The first large-scale commercialization of a spintronics product was done by IBM in 1997[1] with the use of GMR in read-heads in magnetic hard drives. Subsequent applications include flash memory and non-volatile MRAM, in addition to other emerging technologies under development such as spin-torque transfer or STT RAM.

These existing and commercially viable spintronics technologies make use of a fundamental device called a spin valve. Johnson and Silsbee discovered in 1985 that electrons flowing out of a ferromagnetic metal have spins that are aligned in the direction

of magnetization within the metal.[6] Electrons having all of their spins aligned, i.e. their magnetic moments are all oriented in a specific direction, are said to be spin-polarized. A spin valve is designed to operate using a spin-polarized current of electrons which flows out of a metal and which is then made to pass through an insulator or semiconductor to another electrode on the opposite side. The resistance to the current flow through this tri-layer structure will be affected by the magnetization alignment of the opposite electrode. When the valve is turned "on", the magnetization of the opposite electrode is parallel to the electrode from which the electrons are flowing. Electrons can then flow freely into the opposite electrode since their spins are already aligned with the magnetization in this electrode. If the magnetization is aligned in the opposite direction, the electrode magnetizations become anti-parallel, and the current flow is reduced. Thus, the spin valve is "off". These two modes of "on" or "off" can be controllably exploited in a device.

The mechanism of operation of the spin valve can be more completely understood based on the density of spin states that are available in the two metal layers. For a normal, non-ferromagnetic metal, the spins of the electron have no preferred spin orientation regardless of any external applied magnetic field. As a result, at the Fermi level, there is a net equal number of spins aligned in a direction parallel to the field (typically referred to as the "up" direction) as there is in a direction anti-parallel to the field (typically referred to as the "down" direction). This is shown by the green density of states diagram of Fig. I-1(a). In contrast, a ferromagnetic metal has a density of electron spin states with a majority of electron spins polarized in the aligned up direction with the external magnetic field at the Fermi level, as shown in the density of states diagram shown in red and blue in Fig. I-1(b).

The distribution of the majority versus the minority spin states is shifted in the ferromagnetic metal, so that a lesser amount of filled minority down spin states exists at the Fermi level.

The operation of a spin valve is shown by the diagrams in Fig. I-1(c). A first ferromagnetic metal is now paired up with a second ferromagnetic metal which forms the opposite electrode on the right side of Figure 1(c). The two metals are separated by an insulating spacer layer. When the magnetizations of the two metals are aligned (parallel) as in Fig. I-1(c)(i), electrons can flow from the majority (up) spin state of the one electrode to the greater available states for the majority spin in the opposite electrode. Likewise, minority (down) spin states can flow from the first electrode to a proportionally equivalent number of available states on the opposite electrode. When the magnetization of the second electrode has been reversed, as in Fig. I-1(c)(ii), the magnetic layers are aligned anti-parallel. Only a certain number of electrons flowing from the majority state of the left electrode are able to flow into the right electrode, because the number of majority spin states in the right electrode is now greatly reduced, reducing the number of states available to receive the incoming electrons. Thus for parallel alignment, a higher current flows thus giving a lower resistance, and for anti-parallel alignment, a lower current flows thus giving a higher resistance.

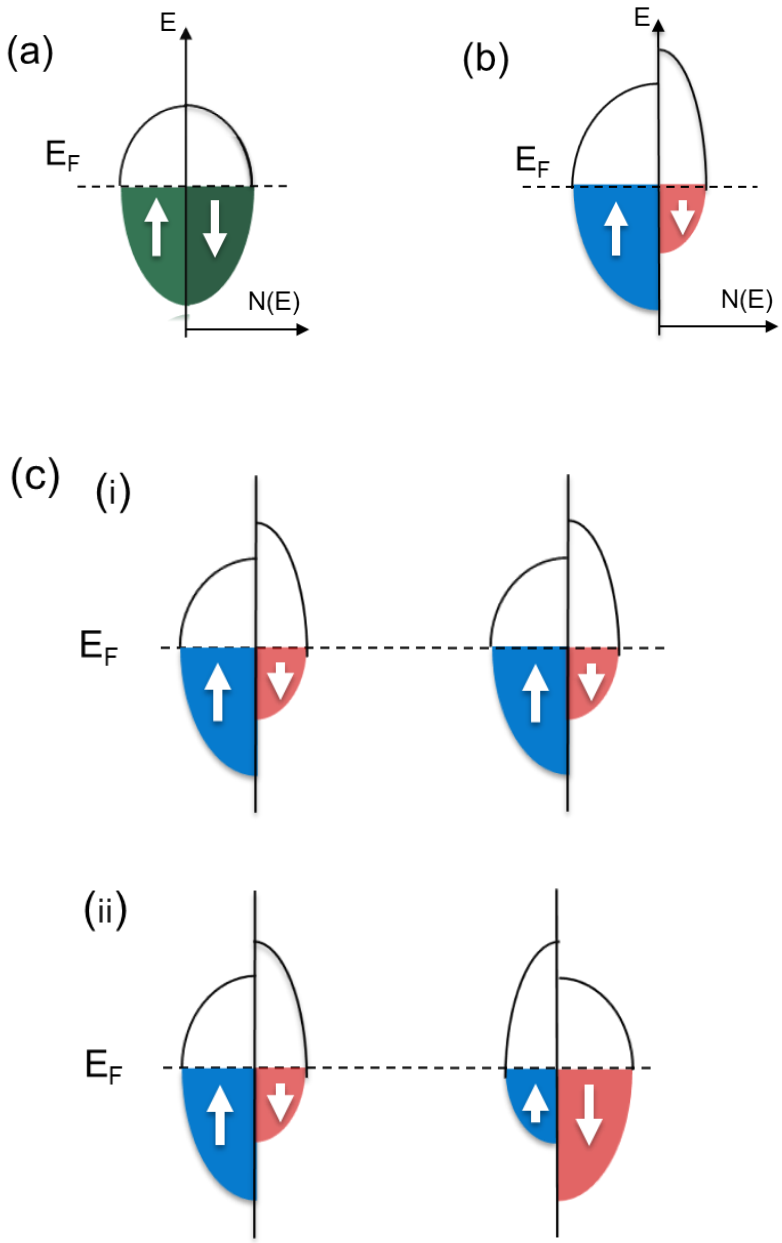

Figure I-1. (a) Density of states for a normal metal (green) and (b) a ferromagnetic metal (blue and red). Energy is plotted vs. number of states N(E) for up and down spins. The normal metal has equal numbers of spin up and spin down states, resulting in no net magnetization, while the ferromagnetic metal has disproportionate numbers of spin up and spin down states so that it can be magnetized in the majority spin direction (up as shown). (c) Parallel and Anti-Parallel alignment configurations for a spin valve: i) Parallel alignment. Electrons flow from a proportionate number of states for majority and minority. ii) Anti-parallel alignment. Lower numbers of electrons can flow because a lower number of states is available for them to go into (majority) or out of (minority).

The magnetoresistance effect is quantified as follows:

$$MR = \frac{\Delta R}{R_P} = \frac{R_{AP} - R_P}{R_P}$$

Where R_{AP} is the resistance in the anti-parallel configuration, and R_P is the resistance in the parallel configuration. Based on the Jullière model[3], the spin polarization of a metal layer can then be determined from its spin-dependent density of states at the Fermi level (see Figure 1):

$$P = \frac{D_{\uparrow}(E_F) - D_{\downarrow}(E_F)}{D_{\uparrow}(E_F) + D_{\downarrow}(E_F)}$$

The MR effect can now be further reduced into its spin-polarization components. Using the independent polarizations P_1 and P_2 for the two individual metal layers, the MR can be expressed as, based on the analysis worked out by Tedrow and Meservey[2]:

$$MR = \frac{\Delta R}{R_P} = \frac{R_{AP} - R_P}{R_P} = \frac{2P_1P_2}{(1 - P_1P_2)}$$

Thus, the MR is a function of the spin polarizations of the individual metals.

In the creation of a spin valve device, it is important to be able to have control over the manner in which the electrons flow through the intermediate layer. There can be different mechanisms of transport of the electrons through the intermediate layer. It is also possible that the conduction is dominated by holes as the charge carriers as opposed to electrons.

Most spin-valves are designed to make use of quantum non-resonant tunneling because the electrons can essentially go through the barrier of the intermediate spacer layer with very minimal interactions. “Non-resonant” refers to the fact that there are no

available electronic states that the wavefunctions of the electrons could resonate with in the intermediate layer. Electrons tunneling in this way, without interaction, are most likely to preserve their spin orientation. However, spin valves have been constructed using the various other transport mechanisms. For example, electrons can travel by hopping conduction from site to site within the intermediate layer. Other types of transport include, for example, thermionic emission and field-emission tunneling.[7,8]

Regardless of the transport mechanism, it is ultimately the number of the spins and how well they maintain their spin orientation during transport which will determine the size of the magnetoresistance effect. To increase the number of spins, materials can be selected that have a greater level of spin polarization. Ferromagnetic metals have a range of different spin polarizations. For example, iron has a spin polarization of 45%, permalloy has 48%, and cobalt 42%.[9] A good deal of current research is being devoted to finding and developing materials that have spin polarizations of 100% - so-called half-metals which are fully spin-polarized at the Fermi level. These materials would be ideally suited to operation in a spin-valve or other spin-based device.

Once a suitable spin-valve device has been made, the device's functionality is measured by sweeping the magnetic field. This makes it possible to set the individual polarization configurations of the electrodes, either parallel or anti-parallel, as shown in Fig. I-1(c). While sweeping the field, the current can be measured as it passes through the spin valve, and once the individual states change, the current and thus the resistance will change. This resistance can be plotted as a function of magnetic field as shown in Fig. I-2.

As a field is swept from a maximum positive to a maximum negative and then back to a maximum positive again, the alignment will go from parallel up to antiparallel to parallel down when the field is decreasing in the negative direction and from parallel down to antiparallel to parallel up again when the field is increasing in the positive direction. In the diagram of Fig. I-2, the magnetizations of the two electrodes are plotted independently (green and orange), where the unit is arbitrary and has been normalized and offset for viewing purposes. As shown in the diagram, there are four independent alignment states indicated by the vertical arrows which show the magnetization direction of the two electrodes. These states correspond to the sweep directions as indicated. The blue and red plots show the magnetoresistance for a cobalt permalloy ideal spin valve. The maximum magnetoresistance of 50% is achieved during the two anti-alignment windows: at negative field (red) during the negative-sweeping magnetic field, and at positive field (blue) for the positive-sweeping magnetic field. The individual switching fields, plotting in the bottom magnetization plot, are called the coercive fields of the ferromagnetic metal electrodes and can vary as a function of thickness, roughness, and impurities in the metal films. For the most part, a permalloy metal thin film of approx. 100nm depositing by thermal evaporation will have a low coercive field of 5-10 Oe and a cobalt metal thin film of similar thickness will have a higher coercive field (up to 50-100 Oe). As shown in the diagrams, the permalloy switches before the cobalt to create the anti-alignment window when the field is swept.

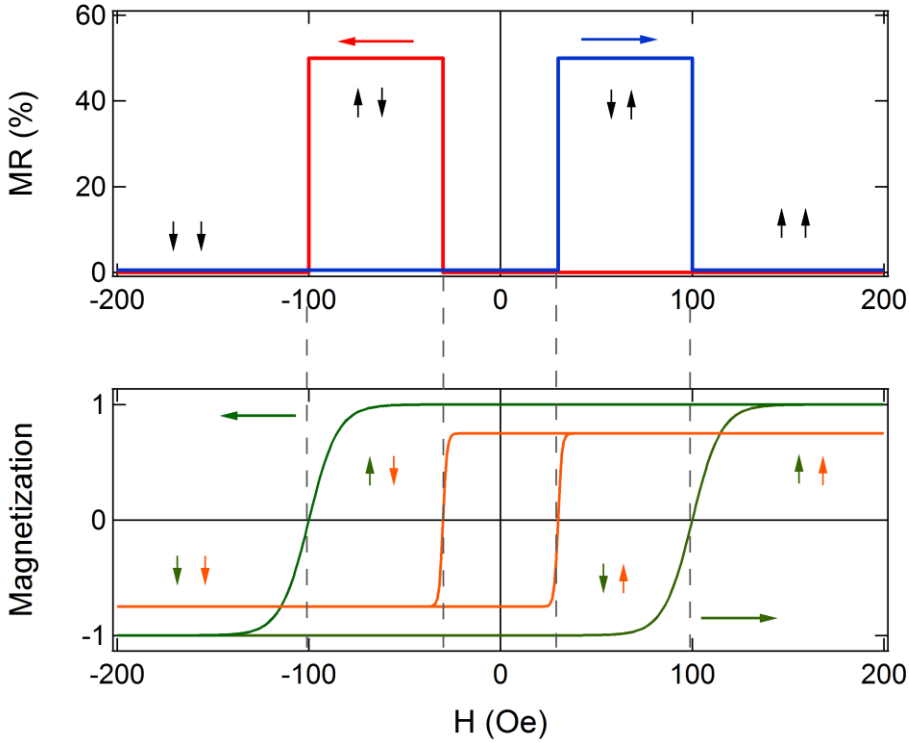

Figure I-2. Diagrams showing magnetoresistance behavior as it relates to the individual magnetizations of the ferromagnetic electrodes in a spin valve. Starting from the parallel configuration at maximum positive field, the softer switching layer (orange, bottom plot) switches first, once the field direction is reversed to become negative, to create the anti-parallel configuration. The harder switching layer (green, bottom plot) switches next to create the parallel configuration, which remains until the field is swept back through zero to the opposite field direction when switching can occur again to make another antiparallel window on the opposite side.

There are many problem areas that need to be improved in making viable spintronics devices. The main focuses are optimizing electron spin lifetimes, detection of spin coherence, transport of spin-polarized carriers over sufficient lengths and across interfaces, and control of spins on fast time scales.[10]

I.2. Introduction to Molecular Electronics

Molecular electronics is for the most part an interdisciplinary field combining research in physics, chemistry and engineering. While the use of electron spin has its own unique appeal and advantages as described above, the use of molecules in electronic devices offers its own additional advantages. The primary advantage is the possibility for reduction of size dimensions. Current electronic dimensions are running up against fundamental size limitations. Existing silicon-based electronics will not be able to be scaled down much less than 10nm in the future. Molecules, at length scales on the order of a nanometer, are at a dimension already below the anticipated finite limit for silicon. Research into molecular electron transport holds promise as a solution to take over in devices once developmental limits in conventional systems have been reached.

An additional advantage of molecules is that they are inexpensive. Using the proper combinations of modern methods and abundantly common natural resources, the supply of organic-based molecules is practically infinite. This is necessary to compete with and provide a smooth future transition from electronics based on silicon, the earth's second most abundant element behind oxygen.

Molecules can also have mechanical properties that make them appealing. For example, they can be made flexible so that they can be worn as clothing. They can also be disposable, integrated into devices for one-time use and then discarded without significant cost to the user.[11]

By manipulating molecules through chemistry, they can be given a wide range of tunable, adjustable functions. Thus, unique device platforms can be created that are based only on the intrinsic molecular behavior. Organic semiconductors have been observed to absorb and emit light while transporting charge, which has enabled them to be used in photovoltaic cells, organic light-emitting diodes (OLEDs) and organic field effect-transistors (OFETs).

The next foreseeable and anticipated stage of applications for molecular electronics will be in developing molecules that can be used specifically for spintronics applications.

I.3. Molecular Spintronics

I.3.a) Introduction

Organic molecules are appealing for use in spintronics for a variety of reasons. Most importantly, they can preserve spin information over extremely long times. This is due to the weak spin-orbit coupling, weak hyperfine interaction, and relatively strong electron-phonon coupling.[12] The most promising types of molecules for use in spintronics devices belong to a class of molecules called organic semiconductors, which are appealing because they can combine the known versatility of inorganic semiconductors for specific electronic applications with the additional possibility of greater functionalization of molecules. A description of the basic properties of organic semiconductors, as well as the challenges in the use of these molecules in electronics, are described in the following.

I.3.b) Organic Semiconductors

One class of molecules that is particularly attractive for use in spintronics devices is that of organic semiconductors. It is envisioned that organic semiconductors could be used in existing applications having the same requirements their inorganic counterparts, such as the channel of a FET device for example. However, organic semiconductors are considerably more complicated than inorganic semiconductors. Characterization techniques successful for inorganic spin electronics cannot be used for organic materials. New measurement and analytical techniques are being developed.

In addition to the challenges inherent in determining spin-dependent transport behaviors in organic semiconductors , more fundamental challenges still need to be overcome in determining the device fabrication and device architecture needed for good characterization of the molecule. The main challenges of ongoing research still lie in determining basic transport behaviors in organic semiconductors and in making good contacts to the molecules. This reality has led to one of the primary objectives of the first study presented in this work, where a relatively new method of contacting molecules, nanotransfer printing, was used.

Many different techniques have been applied for making contacts to molecules, often producing a wide variety of reported results for basic electrical conduction behaviors of the molecules. The result presented here on nanotransfer printing varies from other reported results using different techniques designed for the same type of measurement.

This nanotransfer-printing result[13] serves as a good representative example of the current level of research in the field of molecular spintronics: the urgent need to overcome the challenges of making good contacts on molecules to allow for spin-dependent transport.

I.3.c) Considerations in Making Devices from Organic Semiconductors

It is well known that in inorganic semiconductors, due to the energy-dispersion relationships, there is a low effective mass and high mobility. The conduction and valence bands are curved. Electrons and holes can move freely. In contrast, in organic semiconductors, delocalized 2p and π-electrons make up the molecular orbitals. These electrons have their motion restricted to the molecular orbitals which themselves have very little overlap from one molecule to the next. The molecular equivalent to conduction and valence bands are the energy bands of the highest occupied molecular orbital (HOMO) and lowest unoccupied molecular orbital (LUMO). These bands are relatively flat as a result of the low overlap. There is low dispersion and a large effective mass, so that the electrons have low mobility and move sluggishly.[14]

Band structure calculations by density functional theory and local density approximation have been made for molecular crystals of organic semiconductors. These calculations are always done on models for pure crystals, and reveal bands that are flat and have little overlap. However, in the reality of the experiment, it is very challenging to grow crystals so that they are pure to match the theoretical calculations. Any impurities will only

serve to further localize electrons, causing them to stay put in specific sites for a long time. It is only by thermal energies acting over time that electrons can be made to hop out and move to another location.[14]

The defect sites described above, where impurities localize the electrons, can also affect the spin polarization of electron current passing through them. This occurs by so-called spin-spin scattering. By the Pauli exclusion principle, defect sites can contain up to two electrons. For two electrons to occupy the same site, one has to have spin up and the other has to have spin down. The defect sites are also called "traps" since as mentioned above the electrons become localized and may remain in place for long periods of time. When there are no electrons already in the trap, an electron can go into the trap and then out at a later time without losing its spin polarization. When there is an electron already there, a moving electron (with opposite spin) can hop into the trap to join the other one, but when it leaves the trap its spin could be oriented in either spin up or spin down directions, so the spin in this case is scattered by the single electron that was already in the trap.[14]

Hyperfine interactions are another way that the spin can lose its polarization. An electron interacting with the nucleus of an atom in its near vicinity can enter into a spin precession due to a magnetic field on the order of 10 mT. Any hyperfine coupling could be dominated by a small outside magnetic field. This effect is the basis for a phenomenon called organic magnetoresistance (OMAR).[14,15]

One important consideration in creating structures for a spin valve is conductivity mismatch. Sometimes this is also referred to as impedance mismatch. Due to resistance values that do not match between the metal and the semiconductor, where resistance is significantly higher by many orders of magnitude in the semiconductor, it is not possible to inject electrons into the semiconductor.[16] Essentially there are two parallel paths for each spin (up and down), but because of the large resistance of the semiconductor dominating, the resistance for the paths are approximately the same. A solution to this problem is to place a tunnel barrier between metal and the semiconductor.[17] This allows tunneling into and out of the semiconductor, preserving spin.

Another way of getting spins into the semiconductor layer, although less able to be controlled than the tunneling barrier, is to create an interface layer between the metal and the semiconductor. For example, it has been shown that the creation of an interfacial layer including a Schottky barrier allows for electrons to become injected into the layer, thus overcoming the disadvantages of the conductivity mismatch.

Another important consideration in understanding organic spin valves involves the alignment of the energy levels of the metal and organic semiconductor. As a result of the discrete and localized energy bands in the molecule and even in the LUMO, it is difficult to determine when energy level alignment is occurring. Levels within the band gap of the molecule itself can contribute to the transport by hopping.

Not only do the intermediate sites exist in the molecular layer as previously described, but in addition, conduction can occur via injection of electrons into the LUMO as well as injection of holes into the HOMO. There is also the possibility for the chemical

reaction of the molecule with the metal electrode to cause additional states to form.[18] Furthermore, dipoles are also known to form at the interface, and these dipoles and image potentials can be quite significant in their influence on any tunneling or other transport behavior as a result of the low dielectric constants of most organic materials.[19,20]

Constructing energy level diagrams is also hard to do because of the so-called "pillow effect" occurring at the interface where the metal electrode's wave function is repelled by the first molecular layer (see Figure 4). This can introduce a change to the both the anticipated level of the metal work function and the HOMO level of the molecule. The vacuum level can be shifted by as much as 1 volt due to this effect. It is possible to actually change the interface dipole by allowing polar molecules to absorb on the ferromagnetic metal electrode.[19]

Additionally, it has been reported that phonons and magnons can become active at the interface due to the attachment of molecules to a metallic surface.[21,22] These are expected to reduce any MR effect at higher temperatures.

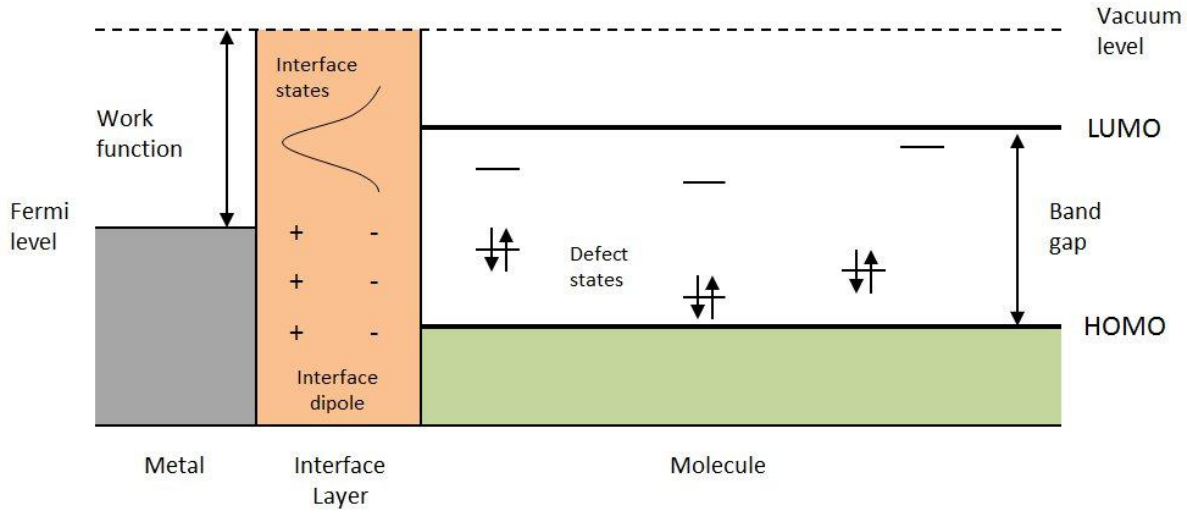

Figure I-3. Energy band diagram of a Metal-Molecule interface. An interface layer is created, which has dipoles that modify the work function of the metal, lowering it by up to 1 volt. In addition, interface states are created by chemical reaction, and defect/impurity states are distributed across the HOMO-LUMO gap. These interface states can form electron traps which cause spin-spin scattering when they become filled. Note that the band structure of the LUMO itself may not form a continuous layer (even without the interface) and may have only discrete, isolated bands due to non-overlapping adjacent molecular orbitals (Adapted from ref. [14]).

For the reasons mentioned above, mainly the localization of the electrons at defect sites and the scant overlap of the molecular orbitals causing low dispersion and low mobilities, organic semiconductors have spin lifetimes that are long but diffusion lengths that are short. Experimentally reported values bear this out. Since the spins do not travel far, it is likely that potential molecular spintronics applications requiring long spin diffusion lengths will be limited. Instead, with organic materials the focus will be on interfacial properties. As mentioned above in reference to Fig. I-3, interface properties can be manipulated and controlled experimentally. Combining the control of the interface with that of the spin-dependent states may lead to new devices.[23]

I.3.d) Molecular Spin Valves

Molecule-based organic spin valves have been around for one decade. The first organic spin-valve was demonstrated in 2002 by Dedui and associates in sexithienyl.[24] The spin diffusion length was determined to be 200nm. They claimed the first direct evidence of spin-polarized injection and spin coherent transfer in organic semiconductors.

Subsequent research into organic spin valves focused on the use of *tris*[8-hydroxy-quinoline]aluminum, or Alq3, as the intermediate layer, motivated by work done by Xiong[12] et al., who demonstrated a 40% magnetoresistance effect. Dediu *et al.*[25] were able to obtain room-temperature magnetoresistance in an Alq3 spin valve. Both of these valves demonstrated inverse MR, however. The presence of the molecule induces this type of inverse effect.

More recent work by Barraud *et al.*[19] in 2010 brought the largest reported size of the MR up to 300% in an Alq3-based structure using a nano-indent made into the Alq3 layer. This time the MR they reported was positive. Barraud developed a model to explain how the MR could in fact change from positive to negative – even for this same basic device structure and geometry – based on interface considerations.

It is possible for the MR to change sign mainly as a result of the interface dipole and image forces forming as a result of the metal/molecule coupling. A weighted density of states can be used to model the hybridization of the spin-polarized states that form. This weighted DOS depends on the various coupling energies between the electrode and the states of the molecule that participate in the coupling. The donor-bridge-acceptor model describes this system.[26] The states of the donor and acceptor are the ones which affect the

coupling behavior. It is important to note that the main term describing the transition results from the bulk behavior between the donor and acceptor, and the bulk behavior may be described by a wide variety of different transport mechanisms.

It has been determined based on this model that when the absolute value of a spin hybridization weighted DOS is much larger than the energy difference between the donor or acceptor state and the Fermi level, an energy difference which is brought on by the interface dipole and/or image forces, the MR effect is inverted. However, when the DOS is much less than the energy difference, the MR is positive. So the control over the interface and the resulting hybridization affects the sign of the MR. A hybridized interface is shown in Fig. I-4.

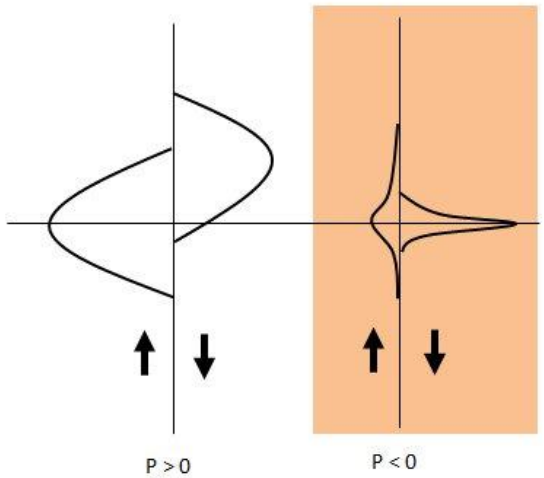

Figure I-4. Hybridization of the spin density of states which can occur at the interface. (Adapted from ref.[19])

Other significant work on organic spin valve structures has been done by Epstein et al. on V(TCNE)[27] and rubrene to make a spin polarizer, and also an all-organic

based spin valve[28]. Work done by de Jong et al.[29] with spin valves made from C_{60} molecules showed a MR resulting definitively from hopping transport between the discrete states of the C_{60} molecules.

I.4. Organization of this Work

Two separate metal – organic molecule – metal structures are examined in this work. The first is a vertical stack structure that uses a self-assembled monolayer of alkanedithiols as the intermediate layer. The second is a vertical spin-valve structure that has a thin film of cobalt-based valence tautomer molecules as the intermediate layer. The structure and functionality of these molecules, their suitability and potential for use in an organic spin-valve as a magnetic tunnel junction, and known behaviors of each will be discussed in the remaining two sections of this chapter. Chapter 2 discusses the procedures for fabrication of the device structures and the experimental procedures for measuring them. Chapter 3 describes metal-molecule-metal junctions made from self-assembled monolayers of alkanedithiols using the novel method of nanotransfer printing. Chapter 4 examines a valence tautomer spin-valve and discusses the unique effects, which have never been seen before, of the tautomer behavior on the magnetotransport. Chapter 5 summarizes the relevant new findings from the two molecular electronic structures.

Molecules Studied

I.4.a) Alkanedithiols

The first part of this study of magnetotransport through metal-molecule-metal structures focuses on alkanedithiol as the molecule in the interlayer. Alkanedithiol is comprised of a carbon chain, the alkane, which can be of varying numbers of carbons and hence varying length. Attached to the carbon chain at each end are thiol groups. The thiol group is a sulfur-hydrogen bond which can form a strong covalent bond with a metal surface. As has been known since early research was done on these types of molecules in the seventies, alkanedithiols can form well-ordered self-assembled monolayers (SAMs) on metal surfaces. These self-assembled monolayers are a uniquely organized system that provides a building block for an electronic, or more specifically, a spintronic device.

When the molecules are dissolved in a solution of ethanol at a specific density and allowed to soak with a metallic surface present in the liquid, they will organize themselves on the surface of the metal by bonds forming between the thiols at the end of the chains and the metal. After enough bonds have formed in sufficient density on the metal surface, the molecular chains will start to interact with each other via Van der Waals repulsive forces between neighboring molecules. Subsequently, the forces will cause the molecules to lift up in the direction out of the plane of the metal surface. Eventually, after the density of the molecules attaching to the surface has reached a saturation, the molecules will all become

oriented in parallel to each other at a specific angle relative to the plane of the metal surface. A highly uniform single-molecule layer is the result.

This uniform structure offers possibilities for an organic electronic or even a spin-valve device in that it can provide an insulating layer. The thickness of the layer can be controlled simply by varying the number of carbons in the alkane chain. In addition, it was recently determined that after a photolithographic system was fabricated and used to connect electrodes to the self-assembled monolayer, electron current through the barrier occurs via non-resonant quantum tunneling.[30,31] These results were supported by the work of other researchers using conducting tip atomic force microscopy (cAFM).[32,33]

In the work presented in this study, cAFM was also used to examine the transport behavior of alkanedithiol SAMs. A novel method of nanotransfer printing was developed for preparing electrodes.[13,34] The method proved to be a way to make reliable contact to the alkanedithiol SAMs. A stable tunneling device structure was made which was scalable by area size of the nanotransfer-printed contacts. The reliability of the contacts enabled characterization of the intrinsic electronic conduction properties of the molecules.

I.4.b) Cobalt-based Valence Tautomers

For the second part of this study, the magnetotransport behavior of a certain class of molecules called valence tautomers was examined. Specifically researched were valence tautomers made from cobalt dioxolene complexes. These complexes have been

synthesized and investigated by collaborator Professor David A. Shultz in the Chemistry Department at NC State University. Valence tautomers are unique molecules in that they exhibit two bistable forms which are switchable as a function of temperature, pressure and light. The switch is caused by an intramolecular ligand-metal charge transfer that is coupled with a metal-based spin crossover. The conversion is accompanied by an increase in the total spin of the molecule from S=1/2 in a low-spin Co(III) form to S=5/2 in a high-spin Co(II), and a molecular expansion due to bond length elongation.

The unique magnetic transitioning behavior makes the molecule a very promising candidate for a spintronics device in that a device could be planned as a spin filter with only one ferromagnetic contact. A molecule layer in contact with this ferromagnetic layer would have a direct influence on the spins that could pass through the two layers because of its own allowable spin states. Essentially, MR behavior would be observed with only one ferromagnetic contact.

A spin-valve made from a thin film of these valence tautomers showed magnetoresistance behavior as a function of the valence tautomeric transition. Both the high-spin and low-spin forms of the tautomer distinctively influenced the magnetic switching behavior of the spin valve. The result was a magnetically activated device that is also uniquely controllable by temperature, light, and electric field. The influence of the tautomeric transition on the magnetotransport behavior of a spin valve is completely novel and has never been observed before.

References

1 Prinz, G. Device physics - Magnetoelectronics. *Science* **282**, 1660-1663, doi:10.1126/science.282.5394.1660 (1998).

2 TEDROW, P. & MESERVEY, R. SPIN-DEPENDENT TUNNELING INTO FERROMAGNETIC NICKEL. *Physical Review Letters* **26**, 192-&, doi:10.1103/PhysRevLett.26.192 (1971).

3 JULLIERE, M. TUNNELING BETWEEN FERROMAGNETIC-FILMS. *Physics Letters a* **54**, 225-226, doi:10.1016/0375-9601(75)90174-7 (1975).

4 BAIBICH, M. *et al.* GIANT MAGNETORESISTANCE OF (001)FE/(001) CR MAGNETIC SUPERLATTICES. *Physical Review Letters* **61**, 2472-2475, doi:10.1103/PhysRevLett.61.2472 (1988).

5 BARNAS, J., FUSS, A., CAMLEY, R., GRUNBERG, P. & ZINN, W. NOVEL MAGNETORESISTANCE EFFECT IN LAYERED MAGNETIC-STRUCTURES - THEORY AND EXPERIMENT. *Physical Review B* **42**, 8110-8120, doi:10.1103/PhysRevB.42.8110 (1990).

6 JOHNSON, M. & SILSBEE, R. INTERFACIAL CHARGE-SPIN COUPLING - INJECTION AND DETECTION OF SPIN MAGNETIZATION IN METALS. *Physical Review Letters* **55**, 1790-1793, doi:10.1103/PhysRevLett.55.1790 (1985).

7 Wang, W., Lee, T. & Reed, M. Mechanism of electron conduction in self-assembled alkanethiol monolayer devices. *Physical Review B* **68**, doi:10.1103/PhysRevB.68.035416 (2003).

8 Sze, S. M. Physics of Semiconductor Devices. (1981).

9 Tsymbal, E., Mryasov, O. & LeClair, P. Spin-dependent tunnelling in magnetic tunnel junctions. *Journal of Physics-Condensed Matter* **15**, R109-R142, doi:10.1088/0953-8984/15/4/201 (2003).

10 Wolf, S. *et al.* Spintronics: A spin-based electronics vision for the future. *Science* **294**, 1488-1495, doi:10.1126/science.1065389 (2001).

11 Sanvito, S. Spintronics goes plastic. *Nature Materials* **6**, 803-804, doi:10.1038/nmat2050 (2007).

12 Xiong, Z., Wu, D., Vardeny, Z. & Shi, J. Giant magnetoresistance in organic spin-valves. *Nature* **427**, 821-824, doi:10.1038/nature02325|10.1038/nature02325 (2004).

13 Niskala, J. N., Rice, W.C., Bruce, R.C., Merkel, T., Tsui, F., You, W. Tunneling Characteristics of Au-Alkanedithiol-Au Junctions formed via Nanotransfer Printing (nTP). *Journal of American Chemical Society* (2012).

14 Szulczewski, G., Sanvito, S. & Coey, M. A spin of their own. *Nature Materials* **8**, 693-695, doi:10.1038/nmat2518 (2009).

15 Wagemans, W., Bloom, F., Bobbert, P., Wohlgenannt, M. & Koopmans, B. A two-site bipolaron model for organic magnetoresistance. *Journal of Applied Physics* **103**, doi:10.1063/1.2828706|10.1063/1.2828706 (2008).

16 Schmidt, G. Concepts for spin injection into semiconductors - a review. *Journal of Physics D-Applied Physics* **38**, R107-R122, doi:10.1088/0022-3727/38/7/R01|10.1088/0022-3727/38/7/R01 (2005).

17 Rashba, E. Theory of electrical spin injection: Tunnel contacts as a solution of the conductivity mismatch problem. *Physical Review B* **62**, R16267-R16270, doi:10.1103/PhysRevB.62.R16267 (2000).

18 Hwang, J., Wan, A. & Kahn, A. Energetics of metal-organic interfaces: New experiments and assessment of the field. *Materials Science & Engineering R*, 1-31 (2009).

19 Barraud, C. *et al.* Unravelling the role of the interface for spin injection into organic semiconductors. *Nature Physics* **6**, 615-620, doi:10.1038/NPHYS1688 (2010).

20 Akkerman, H. *et al.* Electron tunneling through alkanedithiol self-assembled monolayers in large-area molecular junctions. *Proceedings of the National Academy of Sciences of the United States of America* **104**, 11161-11166, doi:10.1073/pnas.0701472104|10.1073/pnas.0701472104 (2007).

21 Wang, W. & Richter, C. Spin-polarized inelastic electron tunneling spectroscopy of a molecular magnetic tunnel junction. *Applied Physics Letters* **89**, doi:10.1063/1.2360908|10.1063/1.2360908 (2006).

22 Tautz, F. *et al.* Strong electron-phonon coupling at a metal/organic interface: PTCDA/Ag(111). *Physical Review B* **65**, doi:10.1103/PhysRevB.65.125405|10.1103/PhysRevB.65.125405 (2002).

23 Sanvito, S. MOLECULAR SPINTRONICS The rise of spinterface science. *Nature Physics* **6**, 562-564, doi:10.1038/nphys1714 (2010).

24 Dediu, V., Murgia, M., Matacotta, F., Taliani, C. & Barbanera, S. Room temperature spin polarized injection in organic semiconductor. *Solid State Communications* **122**, 181-184, doi:10.1016/S0038-1098(02)00090-X (2002).

25 Dediu, V. *et al.* Room-temperature spintronic effects in Alq3-based hybrid devices. *Physical Review B* **78**, doi:10.1103/PhysRevB.78.115203 (2008).

26 Nitzan, A. & Ratner, M. Electron transport in molecular wire junctions. *Science* **300**, 1384-1389, doi:10.1126/science.1081572 (2003).

27 Li, B. *et al.* Room-temperature organic-based spin polarizer. *Applied Physics Letters* **99**, doi:10.1063/1.3651329 (2011).

28 Li, B., Kao, C., Yoo, J., Prigodin, V. & Epstein, A. Magnetoresistance in an All-Organic-Based Spin Valve. *Advanced Materials* **23**, 3382-+, doi:10.1002/adma.201100903 (2011).

29 Tran, L. A., Le, Q. T., Sanderink, J. G. M., van der Wiel, W. G. & de Jong, M. P. The Multistep Tunneling Analogue of Conductivity Mismatch in Organic Spin Valves. *Advanced Functional Materials* **2012** (2012).

30 Akkerman, H., Blom, P., de Leeuw, D. & de Boer, B. Towards molecular electronics with large-area molecular junctions. *Nature* **441**, 69-72, doi:10.1038/nature04699|10.1038/nature04699 (2006).

31 Akkerman, H. *et al.* Self-assembled-monolayer formation of long alkanedithiols in molecular junctions. *Small* **4**, 100-104, doi:10.1002/smll.200700623|10.1002/smll.200700623 (2008).

32 Cui, X. *et al.* Reproducible measurement of single-molecule conductivity. *Science* **294**, 571-574, doi:10.1126/science.1064354 (2001).

33 Engelkes, V., Beebe, J. & Frisbie, C. Analysis of the causes of variance in resistance measurements on metal-molecule-metal junctions formed by conducting-probe atomic force microscopy. *Journal of Physical Chemistry B* **109**, 16801-16810, doi:10.1021/jp052348s|10.1021/jp052348s (2005).

34 Niskala, J. *PhD Thesis* (2010).

Chapter II: Preparation Procedures and Experiments

II.1 Alkanedithiol Self-Assembled Monolayer Sample Preparation

Self-assembled monolayers (SAMs) of alkanedithiols were prepared on silicon wafers coated with a 1 micron layer of silicon oxide, onto which approx. 60nm of gold was thermally evaporated. The gold layer forms a bottom electrode onto which the SAM could readily form. The method of nanotransfer printing was used to make a top electrical contact onto the molecules in the layer. A full study of SAMs made from alkanedithiols having different molecular chain lengths (varying number of carbons) was performed using conducting atomic force microscopy. An additional study was performed on samples made with a varying nanotransfer-printed electrode area sizes. The results of these studies are presented in chapter 3. The essential components of the procedures used to perform the nanotransfer printing are reported here, for other more specific details about SAM preparation please consult the references[1-4], and specifically the PhD thesis by Jeremy Niskala.

Once the monolayer had been prepared using the methods described in the references, the nanotransfer printing was done using perfluoropolyether (PFPE) elastomeric stamps having an array of raised features. These stamps were synthesized by drop-casting liquid PFPE prepolymer (from Liquidia Technologies) onto a planar mold, followed by UV-curing (125 mW/cm^2) for 4 minutes. The stamp was peeled away from the mold, resulting

in a raised array of uniform features. Stamps could be made with differently sized circular or square features.

Two types of PFPE were used to make the stamps, a low-viscosity PFPE and a high-viscosity PFPE. The low-viscosity PFPE, since it is formed from lower molecular weight precursors, has a higher crosslink density and a higher elastic modulus (~ 7 MPa) when compared to that of the high-viscosity counterpart (~ 4 MPa). The elastic moduli of the PFPE were obtained from stress-strain measurements using an Instron 5566 analyzer at ambient conditions.

The flexible polymer stamp sheet, once it had been made from the mold, was then cut into approx. 1cm x 1cm squares which were then taped onto a glass slide with the arrays exposed. Next the stamps were placed into a thermal evaporator inside an mBraun glovebox for thermal evaporation. The glovebox contained a nitrogen environment which provided an inert atmosphere. The evaporation of 20nm Au was done starting at 1 angstrom per second for the first 1nm, following by 10 angstroms per second for remainder. The higher deposition rate was necessary to allow good accumulation of metal on the PFPE surface because its low surface energy leads to low adsorption and high metal migration rates.

Once the evaporation was complete, the PFPE stamps were removed from the glass slides. This way, the stamp's flexibility could be used during printing (See Figure 1 (a) and (b)). To make the transfer, the stamp was placed on top of the SAM so that the array makes contact with the molecules. Then, with stamp resting on the SAM under its own weight, the back of the PFPE stamp was tapped by hand in order to make a good transfer. Next, the

whole assembly is placed into a vacuum (10^{-6} Torr) for one hour to remove any air that may have been trapped between the transferred Au film and the monolayer. Once it has been taken out of the vacuum, the stamp is peeled from the substrate, leaving the electrode array attached to the surface of the monolayer.

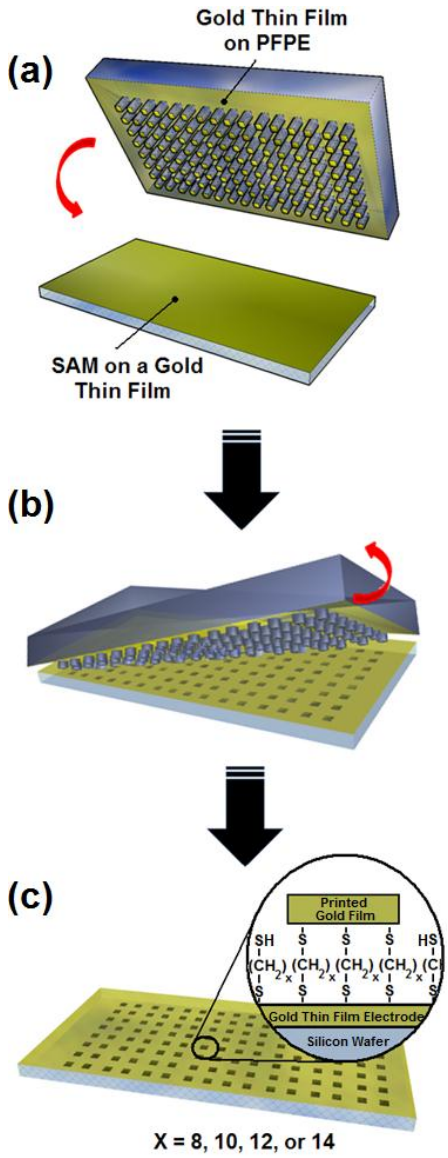

Figure II-1 Method of nanotransfer printing. A polymer stamp is used to apply an array of metal electrodes onto a self-assembled monolayer on a gold thin film. (from ref. [5])

Photolithographic Samples

In order to be able to perform measurements on nanotransfer-printed arrays in a low-temperature cryostat as well as ultimately in a magnetic field for a spin-valve based device, additional modifications had to be made to the device architecture. The main purpose of the modifications was to make it so that wires could be attached onto the sample in order to form the necessary conducting paths to the nanotransfer-printed electrodes as well as the bottom electrode, so that four-terminal measurements could be performed on the junctions via the connecting wires.

To accomplish the task, a crossbar geometry was used. First, the bottom electrode was made of a single bar extending across the silicon-silicon oxide wafer instead of a gold film covering the entire wafer. Next, the SAM layer was made using the method described above, and then the nanotransfer-printing was done to form an array of 50 micron pads over top of the SAM-coated bottom bar. The pad size was usually much larger (at 50 microns lateral dimension) than those made for conducting AFM, due to the limitations of the photolithography. After the pads were transferred, photolithography was performed to create a layer of photoresist into which approx. 12 micron wells were defined to open onto the top electrode pads. Next, a layer of conducting polymer, PEDOT:PSS, was spincoated onto the sample. Crossbars of metal layers could then be made to extend across and into

the well. This was done by depositing metal through a shadow mask. The purpose of the spincoated layer of the PEDOT:PSS was to make a conducting path to the nanotransfer printed pad that would also act as a protective layer to prevent shorting from occurring when the metal was deposited. The nanotransfer printed pads form cracks through which the atoms could go during evaporation, forming metallic filaments that short the junction. This crack formation is detailed in the results section of Chapter 3. The PEDOT polymer molecules are large enough to block the cracks and prevent this shorting. An additional step that had to be performed once the top electrode was deposited was oxygen plasma in order to remove residual PEDOT from areas surrounding the top electrode. This would then isolate the individual crossbars to prevent them from shorting to each other.

The device architecture is shown in Fig. II-2 in a cross-sectional view. Additional details about the fabrication of these types of samples can be found in the references.[3]

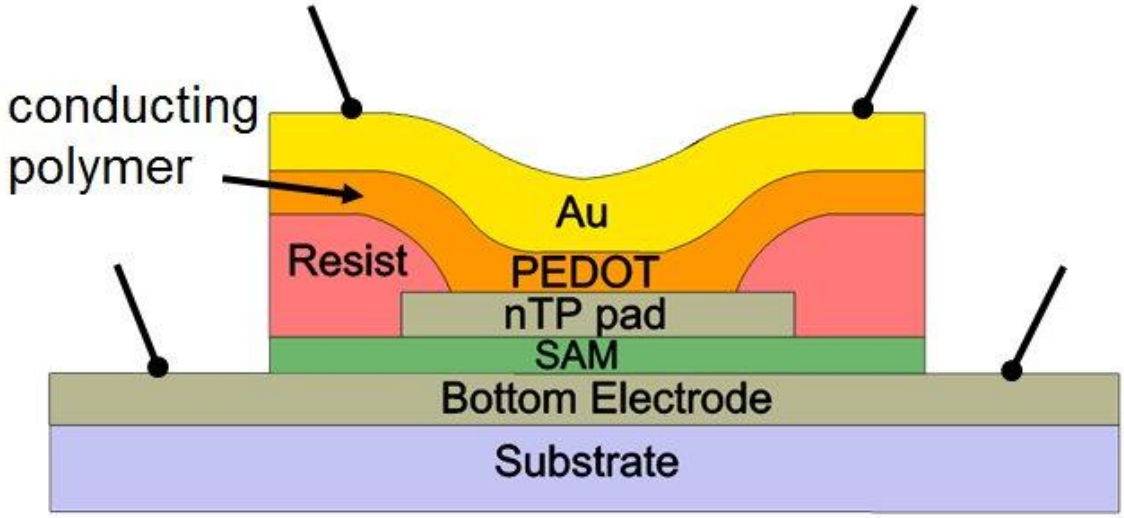

Figure II-2 Cross-section view of the photolithographic nTP sample showing positions of the 4 connecting wires for 4-terminal measurements.

II.2 Valence Tautomer Sample Preparation

The valence tautomer molecules themselves were prepared in the lab of North Carolina State University Chemistry Professor David Shultz. Methods used to prepare the samples have been reported in the literature.[6] The valence tautomers were made in batches of approx. 300 to 400 mg at a time, and transported to UNC-Chapel Hill for use in preparing samples. They were stored in vials as a dark crystalline powder.

Metal-molecule-metal trilayer samples were designed in order to be able to fully explore the known switching behaviors of the valence tautomer molecules as a function of temperature, light and magnetic field. The trilayer was made from a sandwich of a thin film of the valence tautomers between ferromagnetic metal electrodes in a crossbar geometry. The crossbars make it easy to perform a four-terminal electrical measurement. In addition, the entire device was made on glass substrates. This was planned so that, when the metal film for the bottom electrode was made sufficiently thin and hence transparent, the tautomer interlayer could be illuminated in order to produce the known light-induced tautomeric transition. A diagram of the crossbar structure is shown in Fig. II-3.

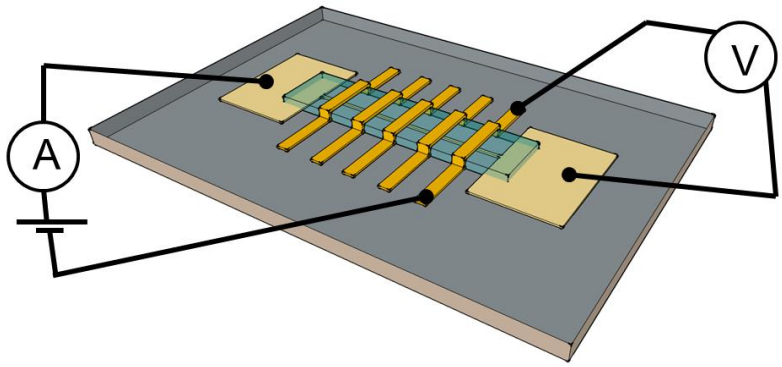

Figure II-3 Valence Tautomer Sample Structure. Crossbars made on top of the valence tautomer thin film enable four-terminal measurements to be made. The substrate is glass so that light can be shone through the bottom electrode, which is made sufficiently thin in order to be transparent, to illuminate the tautomer thin film to induce the tautomeric transition.

Like the alkanedithiol samples, these samples were first examined using probes on the probe station. Subsequently, if a promising sample was found, leads were attached in order for the sample to be mounted into the cryostat for measurements under vacuum, at low temperatures, and in a controllable magnetic field.

Sample preparation was done in the cleanroom at all times. The cleanroom used was the one operated by the Chapel Hill Analytical and Nanofabrication Laboratory (CHANL) on campus in Chapman Hall at UNC-Chapel Hill. This cleanroom is a class-100 ??? facility.

To prepare the substrates, standard microscope glass slides (e.g. Fisherbrand Plain Microscope Slides precleaned, catalog no. 12-550-A3, size 25 x 75 x 1.0mm) were cleaved widthwise into separate pieces, each approx. 15mm x 25mm, using a diamond scribe. Each slide could make 4 to 5 substrates, depending on how well the breakage occurred. These individual substrates were then cleaned by sonication in an acetone bath in a small petri dish for approx. 3 minutes to remove any small shards of glass that may have broken off during the cleaving process. After that, they were rinsed with methanol for a few seconds, followed by another rinse with deionized water. Next they were dried by a flow of nitrogen gas.

The samples were then taken for preparation of the bottom electrode by photolithography. First, an approx. 3 micron layer of the negative photoresist JSR NFR-016 was made on the glass substrate by spincoating in a G3P Spincoat machine (Specialty Coating Systems, Inc., Indianapolis, Indiana) at 3,000 rpm for 30 seconds. The substrates were then subjected to a pre-exposure bake on a hot plate at approx. 100 °C for one

minute. This temperature was slightly higher than the one specified by the manufacturer (90 °C), but produced the best results. The higher temperature may have been necessary due to the increased thermal insulation of the glass compared to the more frequently used standard silicon wafers. Another possibility is that due to the amount of usage to which the hotplate was subjected, a layer of baked on material caused additional thermal losses so that a higher temperature setting was needed.

Following the pre-bake, the substrates were then taken for exposure in a Karl Suss MA6/BA6 mask aligner with a 375W lamp. Substrates were exposed in hard contact mode at 100 microns gap distance. The photomask used for exposure was a design having a dogbone shape with two squares on the ends. The middle connecting piece between the square ends was designed to make a thin 25 micron-wide wire for the bottom contact (see Fig. II-3). The squares were each approx. 5x5mm and the wire length in the middle 15mm.

After exposing for 14 seconds, the substrates were taken for a post-exposure bake of 1 minute again on the hotplate at approx. 100 °C. They were allowed to cool, then developed by gentle agitation in a bath of MFP-319 developer for one minute. Next, they were placed in a bath of deionized water and moved back and forth for 10 seconds, then rinsed with a gentle flow of deionized water for another 5 seconds. After that, a gentle flow of nitrogen gas was used to dry them.

Then the substrates were examined under a Nikon Eclipse LV150 optical microscope at 5x zoom to check for integrity of the bottom electrode. Specifically, they were examined to make sure there were no residues of photoresist in the wire section which should have

developed away, and also to see that there was no residual photoresist, visible by the diffraction pattern it produced, in the areas of the squares.

After photolithography, the substrates were ready for metallization. A layer of 3nm titanium followed by a layer of approx. 35nm gold was deposited using a Kurt Lesker PVD 75 sputtering machine. The gold layer thickness was selectively varied depending on the objectives of the sample batch being prepared. The function of the gold layer was to allow for an overall increased conductivity in the bottom electrode. By depositing a layer of gold first before the layer of the ferromagnetic permalloy was deposited, the overall resistance would be lower than if the entire contact was permalloy. The gold makes a better electrode because it does not oxidize and produces very smooth films. It was thought that permalloy deposited directly onto titanium (needed as a wetting layer) would continue to maintain the rough growth of the titanium deposition, whereas the gold on the titanium would tend to smooth out any rough features by filling in the peaks and valleys.

The use of the gold indeed allowed an improvement upon earlier versions of the electrode which had as much as 10 times higher resistance, thus lowering the resistance from kiloohms to hundreds of ohms (200 to 400 ohms). This was partly because a thicker layer was being made with the gold, but also because of the aforementioned properties of the gold layer.

Once the titanium and gold had been deposited, the samples were removed from the sputtering machine and taken to a nitrogen-filled glovebox with an enclosed thermal evaporator. The glovebox is an mBraun model MB-EVAP. The glovebox plus thermal

evaporator is used to prevent the ferromagnetic permalloy from oxidizing before the valence tautomer film has been applied to it. The substrates were taken into the glovebox and then into the thermal evaporator which was pumped down to $1x10^{-7}$ Torr for the deposition. A single permalloy pellet from Kurt J. Lesker company (?) was placed onto a R.D.Mathis thermal evaporation boat, part number S8A-.015W. Evaporation of the permalloy began once a power of approx. 35% was reached, after slowly ramping the power manually at 10% per minute. The deposition rate slowly increased to as high as 4 angstroms per second after the deposition started. The power was increased so as to keep the deposition rate from falling, but not necessarily to increase it beyond the initial maximum value reached once the deposition had started. The intended permalloy layer thickness was approx. 25nm. After deposition, it was possibly to see through the metal layers by eye.

Next, the samples were transferred inside the glovebox to an attached solvent chamber portion of the box for spincoating of the valence tautomer film. This section has a built-in floor-recessed spincoater, model G3P-8, manufactured by Specialty Coating Systems, Inc. of Indianapolis, Indiana. Lift-off of the photoresist to produce substrates with only the back electrode needed to be performed prior to spincoating. This was done by putting the substrates into closed containers filled with acetone and letting them sit for approx. 3 hours. After that time, the substrates could be agitated or stirred for easy removal of any residual metal flakes to reveal the patterned back electrode. The substrate was then transferred into a separate container of toluene for a rinsing step. To do this, the substrate was just stirred slightly in the container filled with toluene. The substrates were then set aside to dry in the solvent chamber. Usually this takes only a couple of minutes.

With the substrates ready for spincoating, the solutions of the cyanopyridyl valence tautomer were prepared in the desired concentration level. It was determined that saturation occurs at approximately 11.2 g/L by observing when the precipitate cannot be fully dissolved. Usually 1 mL of the solution was sufficient to spincoat 7 samples, so the starting quantity of VT ranged from 10mg to 25mg for this batch size. The VT was weighed out in the lab on a scale into a 20mL glass scintillation vial before transfer into the glovebox. The vial was left open during transfer into the box, while cycling in vacuum to get to a nitrogen environment, in order to remove any air remaining in the vial on the VT. Hypodermic needles were used to extract toluene of the right amount to obtain the intended mixing ratio.

Once the toluene was transferred, the solution was mixed by gently rolling the vial back and forth. Then the needle was placed into the vial in order to draw the solution into the syringe. Once the solution was in the syringe, the needle was removed, and spincoating could be done by using the syringe as a dropper. The appropriate speed was selected, usually 500rpm for 20 seconds. A study to find the optimum spin speeds and times, as well as the optimum concentrations with different solvents, was conducted, and results are presented in Chapter 4. The solution was dropped onto the substrate to fully cover it, and then the spincoater was started. Once spincoating was complete, the substrates were set aside to dry thoroughly. Usually several hours were given for this, if not allowing them to dry overnight.

After the films were spincoated, they were usually transparent and slightly greenish in color. The VT solution when mixed in the vial or syringe appears very dark blue with a slight greenish tinge. The solution is so dark it might be considered black. Only when looking at a very thin region can the color be determined. Some of the thicker films formed on substrates from higher concentrations were dark, and it was even possible to form a very thick layer (10s of microns thick) that was completely black and opaque from a saturated solution of dichloromethane.

For deposition of the top contact, the samples were taken to the cleanroom of the Shared Materials Instrumentation Facility at Duke University, where a CHA Solution e-beam evaporator was used to deposit the cobalt top contact. This evaporator has a source-to-substrate distance of 15 inches, and the starting vacuum pressure was $5x10^{-6}$ Torr. The metal was deposited onto the substrates through a thin aluminum sheet metal shadow mask designed to make five crossbars perpendicular to the bottom electrode wire. To mount the shadow mask, it was taped down using two small 1-2mm wide strips of Capton tape. The substrates themselves were mounted 3 each onto glass slides using double-sided tape. After deposition, the five crossbars of the top contact were each approximately 350 microns wide, although later an improved mask was made to have 200 micron wide crossbars.

Prior to mounting the shadow mask, a synthetic Q-tip soaked in acetone was used to wipe away the VT film in a band parallel to the wire of the bottom electrode several millimeters on either side of it. Also, the film that had formed on top of the square end of

the bottom electrode was wiped away. The purpose of the wiping was to allow a clean surface so that the ends of the crossbar would have a good adhesion to the glass substrate for later placing probes or attaching leads. It had been discovered that attaching wires using silver paste onto an electrode which was deposited directly on top of the VT film did not work well because the roughness of the VT film caused poor adhesion. This caused the wire to break away and fall off of the substrate during later measurements.

For the deposition, 100nm of cobalt was deposited at a deposition rate of 1 angstrom per second, followed by 250nm of gold at a deposition rate of 10 angstroms per second. The gold was deposited, as before for the bottom contact, for improved conductivity. For this contact, however, as thick a layer as desired could be made because there was no longer a limitation. In fact, it was desirable to have a thicker layer to allow for better coverage of the rough surface of the spincoated film. 250nm of gold was arbitrarily chosen based on the usage limits of the facility. Resistances across the top contact were consistently 10 ohms or less.

After the top contact was made on the samples, the samples were examined at first in the probe station to determine I-V behavior. Promising candidates that were not shorted ($< 1\Omega$) or open ($>1\times10^{12}\ \Omega$) and showed interesting I-V characteristics were selected to be wired up and put into the cryostat for vacuum measurements at low temperature, under a variable magnetic field, and with illumination by light. An experiment using the Magneto-Optic Kerr Effect (MOKE) was performed to determine the magnetic switching behavior of

the ferromagnetic metal layers. All of these measurement procedures are described in their respective sections below.

II.3 Conducting Atomic Force Microscopy (cAFM) Measurements

Conductive atomic force microscopy (cAFM) measurements were carried out on alkanedithiol SAMs in order to determine I-V behavior. The majority of these measurements were performed by collaborator Jeremy Niskala. Reference is made to his PhD thesis[3] and relevant publications[4]. A brief description of the technique is included here in the following.

The cAFM measurements were made using an Asylum atomic force microscope (Asylum MFP-3D,*Asylum Research*) with an Orca dual gain cantilever holder and customized Ti/Au coated silicon cantilevers (Budget Sensors, Tap300Al). In an effort to minimize contact resistance between the conductive tip and printed feature, substantially large area AFM cantilevers (≥80 nm diameter) were manufactured. Custom coating of the cantilevers was performed using a Kurt J. Lesker PVD 75 magnetron sputtering system. The cantilevers were mounted onto a glass slide using double sided tape with the tip exposed. 25 nm of Ti was sputtered onto the tips followed by 200 nm of Au (substrate temperature ~ 30°). The spring constant of the newly formed tips was calculated to be ~ 73 N/m. The tip diameter was confirmed by SEM. For contact mode I-V measurements, a survey height map was first gathered in tapping mode to define the position of each feature. The tip was then brought

to direct contact with each individual feature in contact mode using ~ 10 nN of compressive force to ensure complete contact while minimizing contact-based resistance. Each junction was scanned through a bias range while detecting current. A single I-V curve was gathered for each junction before moving to the next junction. Depending on the sample, this process was repeated on 20 – 150 features per substrate. Conductive measurements were obtained in contact mode using a loading force of ~ 5 - 10 nN. Loading with forces ≥ 20 nN resulted in shorted devices while the AFM tip forced the transfer printed electrode into direct contact with the bottom electrode. Disengaging the tip and then re-loading with ~ 5 - 10 nN again resulted in a functional device. As a control, bare gold surfaces were contacted with a custom conductive AFM tip which included a 1 MΩ resistor in series. This experiment was done to ensure that both the applied force of the tip and the area of the tip were sufficient enough to produce reliable results while contacting the surface. The surface was contacted as before with ~ 5 - 10 nN of tip force using three separate custom coated AFM tips.[3]

Conductive mapping of the features was gathered in tapping mode under a 1.0 V surface bias and a grounded conductive tip. The 2D conductive map was superimposed over the corresponding height map (gathered simultaneously) to show a contrast in the junction's current on and off the transfer printed feature using. Superposition of the 2D conductive map and height map, data flattening, and 3D image rendering was performed using the Argyle Light software (*Asylum Research*.).[3]

II.4 Probe Station Measurements

Metal/SAM/metal devices were measured on an Alessi Industries probe station for a four-terminal measurement. The four probes were two Alessi Industries probes and two Signatone Model S-600 probes. The circuit for the I-V measurement included a DC source and an AC function generator for measurement of the differential conductance with a lock-in amplifier. The DC source was a Keithley 230 Programmable Voltage Source, and the AC function generator was a Wavetek Model 270 12MHz Programmable Function Generator. The function generator was connected across the primary windings of a conventional transformer to step down the input voltage in order to output a sine wave at the secondary winding. In addition to stepping down the input voltage to a desired range of usually less than 25mV peak-to-peak, the transformer was used to isolate the AC function generator from the circuit. This was necessary to prevent any feedback into the circuit that might affect the controller electronics. In some cases, controller electronics of other voltage sources had operated to offset the AC signal when the DC target output voltage was to be zero or within a range of zero that corresponded to value of the AC peak.

The DC source was connected in series to the secondary winding on the transformer, followed by connection to one side of the top electrode crossbar on the SAM device via the probe. Next a probe was connected to the back (bottom) electrode on the sample wafer, and this leg of the circuit then went to an op-amp based current converter/amplifier hard-wired to convert the input current into a voltage signal at a magnitude of 100 times or 1 times its input current. The output voltage signal from the current amplifier was branched to a Keithley 2182A Nanovoltmeter, to read the voltage-converted DC current signal, and,

on the other side of the branch, to a Stanford Model SR830 Lock-In Amplifier to read the modulated current signal occurring at the specific DC voltage. The DC voltage across the other two terminals (top electrode to bottom electrode) was recorded by a Keithley 6514 Electrometer. A National Instruments Labview program ran the various meters using GPIB interfaces and recorded the data for the I-V and differential conductance measurements.

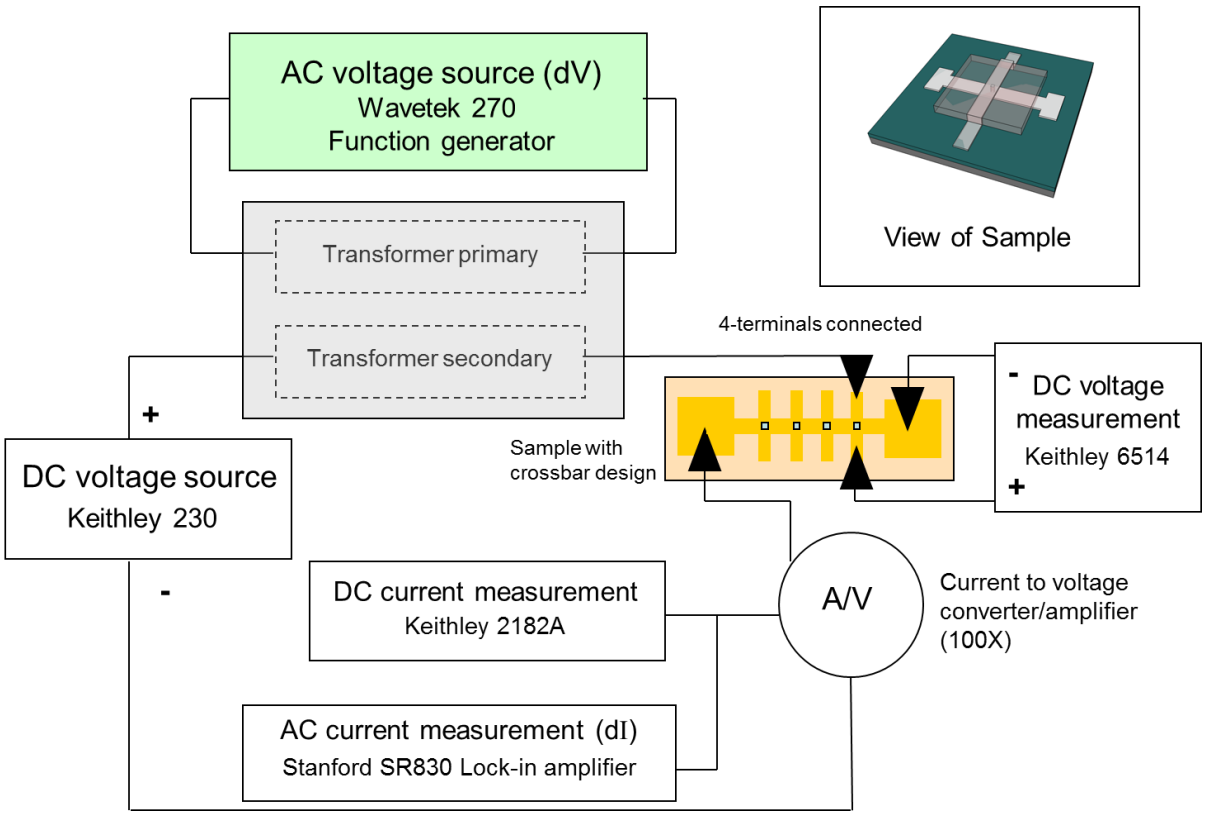

Figure II-4 Circuit diagram for 4-terminal measurements. Circuit as shown was used on the probe station. This same circuit was used to conduct magnetotransport measurement with an additional lock-in amplifier to measure the AC voltage (dV). The additional lock-in amplifier was connected in parallel with the DC voltage measurement.

II.5 Low-Temperature and Vacuum Magnetotransport Measurements

For low-temperature vacuum magnetotransport measurements, two separate systems were used. Both systems had vacuum and cooling equipment that could be put into the magnetic field produced by either of two separate electromagnets. The electromagnets each had their own electronic control system. The systems are described separately in the following two sections.

System I: Joule-Thomson Cooling Chamber

To put the sample into vacuum, a small, custom-built vacuum chamber was used (approx. 5”x3”x2”). The chamber was designed to accommodate a Micro Miniature Refrigerator manufactured by MMR (MicroMiniature) Technologies of Mountain View, CA. It is capable of cooling a sample down to liquid nitrogen temperature (77K). The design makes use of small capillaries for the flow of gas inside a glass sample mounting arm. When the gas reaches the sample mounting location, the capillary expands out into a small expansion chamber, allowing cooling of high-pressure nitrogen gas by the Joule-Thompson effect.

The gas used comes from a high purity nitrogen (99.999%) compressed gas cylinder from National Welders. A silicon diode affixed to the gold sample mounting pad inside the MMR chamber at the cooling point (gas expansion point) is used to monitor the sample temperature. To reach a specific set point temperature, a Lakeshore 330 Temperature

Controller monitors the temperature using the diode, and increases or decreases the voltage output to a heater circuit also located underneath the gold sample mounting pad. The heater is capable of heating against the cooling effect and can bring the sample temperature rapidly from 77K to room temperature, for example, if desired. The sample holder wafer with the sample mounted onto it is mounted onto the sample mounting pad using Dow-Corning 340 silicone heat sink compound (a type of thermal grease).

To obtain the necessary vacuum, approx. $5x10^{-6}$ Torr for most measurements, a turbo pump system was built consisting of a Varian DS102 roughing pump and a Varian Turbo-V 70D Macro Torr turbo pump controlled by a Varian Turbo V-70 controller. A Granville-Phillips 270 Gauge Controller was used to determine the pressure by reading either an MKS ion gauge or a Duniway Stockroom DST-06M thermocouple mounted inside the vacuum system. A 3/8" inside diameter rubber tube connected the vacuum pump system to the vacuum chamber.

The chamber is small enough so that it can also be placed between the poles of an electromagnet in order to perform magnetic field measurements on the sample. Control of the magnet is done using a Labview program (as described in the MOKE section), and electrical measurements are performed at different applied fields, as discussed below.

To mount the sample, was necessary to create leads going from the electrodes of the sample to soldered connections on a feedthrough in the walls of the vacuum chamber to perform measurements using the same measurement equipment above as was used on the probe station.

To make electrical connections into the vacuum chamber, two different mounting schemes were used. For the first type of mounting, primarily used for initial measurements of SAMs, the sample wafer was first affixed to a separate sample holder. The holder was actually another separate wafer with a 1 micron silicon oxide. Photolithographic patterns were made on it so that wires could be connected by either wirebonding or soldering. Larger wires were soldered onto one side of the pads of the photolithographic pattern. These wires could then make a continuous contact across the pads to 0.010" diameter aluminum wires which were attached onto the opposite end of each pad by wirebonding. The wires that were wirebonded would then be connected over to the sample containing the SAM as shown in the picture. The wirebonder used is a Kulicke and Soffa model no. 1413.

The reason wirebonding was used was to prevent any heating which would have been necessary if larger wires had to be soldered directly onto the sample containing the SAM. The thermal conductance of the silicon wafer would have easily allowed the temperature on the SAM to exceed 40°C, which was a temperature reported to cause the monolayer to degrade.[7] (check ref)

A second mounting scheme was also developed. It was used mainly to mount the samples of valence tautomer thin films. As mentioned above, the crossbar contacts for the electrodes were prepared such that the metals deposited for the top and bottom contacts were directly applied to the glass substrates. The top contact was made to go from the surface of the glass, up onto the VT film over the bottom electrode, and then back down to the glass substrate on the other side.

Copper wires manufactured by the Belden company, 40 AWG gauge with insulation coating, were stripped at both of their ends under a microscope using a razor blade to prepare them for placement on the samples. All wires were soldered at one end to a mounting terminal pin block designed to fit into a corresponding terminal block on the cryostat. The other ends of the wires were then affixed to the sample on the edge of the glass substrate approx. 1-2mm from their stripped ends using small pieces of masking tape (approx. 1mm x 1mm). Each wire was positioned so that its stripped end was resting on the corresponding end of a top electrode or one of the two squares of the bottom electrode. The masking tape pieces were prepared by putting the tape onto a glass slide, and then cutting out the square with a razor blade.

Once the wires were held in position by the tape pieces, a small drop of silver conductive adhesive paste, stock number 42469 from the Alfa Aesar company of Ward Hill, MA, was applied to the end of the wire to fully cover it and overlap the electrode metal layer below it. A whittled, sharpened end of a wooden Q-tip was used to make a spear to carry and apply the drop of Ag paste. Once all wire ends had been covered in this manner, the sample was covered with a glass dish and allowed to dry for a minimum of 8 hours, usually overnight.

System II: Liquid Flow Cryostat

Magnetotransport measurements were performed on valence tautomers using a flow cryostat, model RC102 from Cryo Industries of America, Inc. The cryostat operates

using a controlled flow or dripping of liquid nitrogen or liquid helium into an approx. 1 inch diameter pipe chamber inside the larger 3 inch diameter vacuum chamber. The sample is mounted on a copper cold finger extending out underneath the liquid collection area. The vacuum is obtained using the same vacuum turbo pump system described above.

There are twenty-four wire leads which extend out from the sample mounting block for making electrical connections to the sample. These wires connect to an insulated 24-wire cable that then connects to a custom-built breakout box. Triax cables are used to make connections from the breakout box to the meters for performing the measurements.

The substrates were mounted using the Dow-Corning 340 silicone heat sink compound to a 1”x1”x0.2” copper block that could be bolted to the cold finger of the cryostat for good thermal conductivity. The sample could be positioned over a 0.25 inch diameter hole in the copper block so that two adjacent crosshairs could be illuminated by laser light through the hole from beneath the sample and through windows in the wall of the vacuum chamber aligned with the hole.

When the system was running, it was possible to control the flow of liquid using a needle valve on the transfer line, in order to minimize the flow while still obtaining the required cooling power. With the system optimized this way, the cooling could be continued for as much as 20 hours at a time using liquid nitrogen. The temperature could be set to a desired temperature set-point and maintained there by a Lakeshore Model 335 Temperature Controller.

II.7 Magneto-Optic Kerr Effect (MOKE) Experiment

Magnetization studies were carried out using an experimental set-up that measures the Magneto-Optic Kerr Effect. In our experiment, a birefringent photoelastic modulator (PEM) modulates the reflected laser beam, in order to separate the polarization components of rotation and ellipticity in the reflected beam using lock-in techniques. Both components are proportional to the magnetization in the sample.

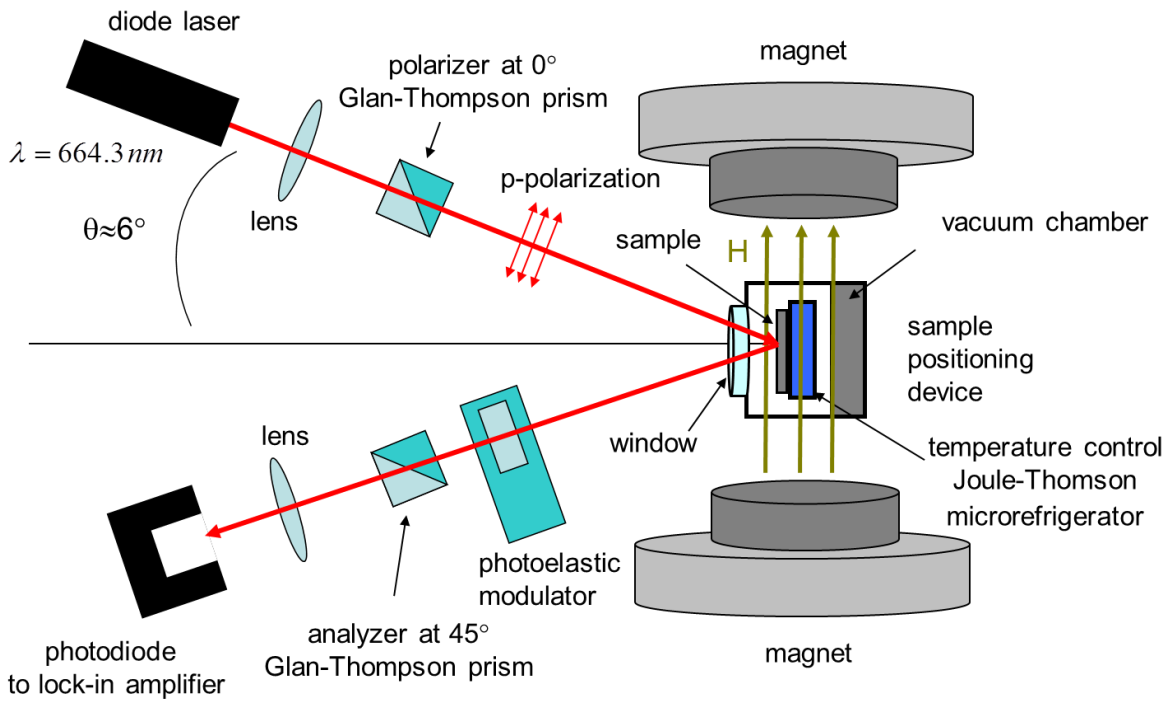

Figure II-5. Experimental Set-up for the Magneto-Optic Kerr Effect (MOKE). The laser spot size for the experiment was approx. 50 microns full-width half max.

In the conventional set-up for our longitudinal MOKE experiment, as shown in the diagram, the laser output from a diode laser (K-Space Associates) at a wavelength of 664nm

passes through a focusing lens and then through a Glan-Thompson prism polarizer set at 0° that polarizes the laser light in the incident plane (p-polarization). The laser beam then reflects off of the sample mounted perpendicular to the plane of incidence in the vacuum chamber between the poles of an electromagnet. The reflected beam then passes through the bi-refringent photoelastic modulator (or PEM) (Hinds Instruments model PEM-90, with modulation frequency of 50kHz and set to $\lambda/2$) and then an analyzer, also a Glan-Thompson prism, set at 45° rotation from the polarizer. The light is focused through a lens onto a photodiode.

The signal from the photodiode is passed to two lock-in amplifiers, one using a reference source supplied from the PEM controller at 1x the PEM modulation frequency (1ω = 50kHz) and a second using a reference source from the PEM controller at 2x the PEM modulation frequency (2ω = 100kHz). The two signals are deconvoluted by the lock-in amplifiers. They correspond to the change in ellipticity (1ω) and rotation (2ω) undergone by the incident polarized light as a result of the MOKE effect. In our analysis, we focused primarily on the 2ω Kerr rotation signal. The system is designed to operate as described in the literature.[8]

The magnet is driven by a Kepco Power Supply ATE 100-10M. The DC signal from the photodiode is input into a Hewlett-Packard 3456A Digital Voltmeter. The entire experiment is operated by a Labview program. The main function of the program is sweeping of the magnetic field by increasing or decreasing the output of the power supply which controls the current through the electromagnet. Positioning is also controlled on the sample surface via two stepper motors that change the horizontal and/or vertical location

of the sample. Positioning onto the individual device or region of interest was aided with the use of a CCD camera, an Adimec MX12P.

References

1 Hoertz, P., Niskala, J., Dai, P., Black, H. & You, W. Comprehensive investigation of self-assembled monolayer formation on ferromagnetic thin film surfaces. *Journal of the American Chemical Society* **130**, 9763-9772, doi:10.1021/ja800278a|10.1021/ja800278a (2008).

2 Niskala, J. & You, W. Metal-Molecule-Metal Junctions via PFPE Assisted Nanotransfer Printing (nTP) onto Self-Assembled Monolayers. *Journal of the American Chemical Society* **131**, 13202-+, doi:10.1021/ja9047152 (2009).

3 Niskala, J. PhD Thesis, "Molecular Spintronics: Design, Fabrication, and Characterization". *University of North Carolina at Chapel Hill* (2010).

4 Niskala, J. N., Rice, W.C., Bruce, R.C., Merkel, T., Tsui, F., You, W. Tunneling Characteristics of Au-Alkanedithiol-Au Junctions formed via Nanotransfer Printing (nTP). *Journal of American Chemical Society* (2012).

5 Niskala, J. *et al.* Tunneling Characteristics of Au−Alkanedithiol−Au Junctions formed via Nanotransfer Printing (nTP). *Journal of the American Chemical Society* **134**, 12072-12082 (2012).

6 Schmidt, R. D. Investigation of the Electronic and Magnetic Properties of Electron Exchange: Exchange Coupled Donor-Bridge-Acceptor Biradicals and Novel Magnetic Behaviors of Bis(pyridyl) Cobalt Dioxolene Valence Tautomers. *PhD Thesis* (2010).

7 Akkerman, H., Blom, P., de Leeuw, D. & de Boer, B. Towards molecular electronics with large-area molecular junctions. *Nature* **441**, 69-72, doi:10.1038/nature04699|10.1038/nature04699 (2006).

8 SATO, K. MEASUREMENT OF MAGNETO-OPTICAL KERR EFFECT USING PIEZO-BIREFRINGENT MODULATOR. *Japanese Journal of Applied Physics* **20**, 2403-2409, doi:10.1143/JJAP.20.2403 (1981).

Chapter III: Tunneling through Alkanedithiol Self-Assembled Monolayers

III.1. Introduction

One of the most fundamental challenges to the rapidly developing field of molecular electronics is making good electrical contacts onto molecules. A good electrical contact allows scientific characterization of intrinsic molecular electronic properties and has the reproducibility and stability necessary for production of a working device. Currently many different techniques are being utilized to make metal contacts onto molecules; however, these techniques have produced a wide range of different resultant behaviors and reliability. Usually imperfections due to impurities, defects, variations in the number of molecules contacted, and changes to the metal-molecule interface including hybridization or modification of the density of states of the molecule are to blame. A consistent, functional technique for making contacts that are permanent and leave the molecules unperturbed is thus very desirable.

One structure of particular interest in the field of molecular electronics for its promise as a potential way to improve interfaces is that of the self-assembled monolayer (SAM). SAMs have been studied since the 1970s, and their behavior is well known. A monolayer of molecules (in this study alkanedithiols) can be allowed to form on a metal surface by soaking the surface in a solution containing the molecules. Due to the covalent

bonds forming to anchor the end groups (thiols) of the molecules onto the metal, the molecules become evenly distributed over the metal. Subsequent van der Waals interactions between the molecules cause them to align in parallel extending off the surface of the metal. The result is a well-ordered monolayer that can provide an insulating layer for an electronic device having electronic properties intrinsic to the molecules forming the monolayer. However, as mentioned above, suitable electrical contacts need to be fabricated onto the top of the monolayer.

Nanotransfer printing using polyfluoropolyether (PFPE) elastomeric stamps provides an inexpensive and simple method to create good electrical contacts onto a self-assembled monolayer of alkanedithiols. With this method, the molecules can be studied to determine their intrinsic behavior while at the same time, a permanent device architecture is created. This method does not require the use of any additional layers to protect the SAM from damage, as has been previously required when making permanent contacts. Arrays of thin metal film electrodes can be transferred without damage to the underlying monolayer as described in Chapter 2. The electrode sizes can be varied over a wide range from 200nm diameters to 7 micron squares so that the entire process can be scaled as needed for applications.

This chapter describes a study which used conducting atomic force microscopy (cAFM), with the conducting tip applied to the top nanotransfer-printed electrode as described in Chapter II, in order to determine the electrical properties of alkanedithiols in tunnel junctions. The stable junctions have reproducible I-V behavior showing symmetrical

tunneling barriers. This indicates consistent quality of both the bottom contact onto which the monolayer is formed from ethanol solution and the top contact made by nanotransfer-printing.

Electrical tunneling parameters for the individual segments of the molecule, the alkane and the thiol end groups, could then be determined by varying the overall length of the molecule, as a function of the number of carbons included in the alkane chain, from octanedithiol (C8) to tetradecanedithiol (C14). The parameters were calculated using the Simmons tunneling model. Additionally, scalability of the device structure was explored by varying the area of the nanotransfer-printed electrodes.

III.2. Conducting Atomic Force Microscope Study of Molecular Tunnel Junctions made with Nanotransfer Printed Electrodes

Monolayer and nTP Characterization

The alkanedithiol self-assembled monolayers (SAMs), made using the procedures described above in Chapter 2 and in the published references[1-4], were characterized by X-ray photoelectron spectroscopy (XPS) and electrochemical reductive desorption measurements with a standard three-electrode electrochemical cell,[2] demonstrating the monolayer to be dense and the molecules to be vertically aligned as previously reported.[3]

As described above, the nanotransfer-printed gold electrode arrays were printed from the PFPE stamps onto the SAMs on the gold films. The arrays are well-defined over several square millimeters as shown in Fig. 1. The gold on the PFPE stamp transfers easily onto the SAM as a result of the strong chemical affinity between the Au and the thiol end group of the molecule. Thiols are known to bond covalently to gold, and it is believed that this type of strong bonding is occurring to facilitate the transfer. After sonication for 1 minute in THF, the electrodes did not show any signs of degradation. In addition, the scotch tape adhesion test[5-7] was performed on the nanotransferred pads, and they could not be removed.

AFM topography and conductivity images were made of the nTP gold surfaces of the pads, revealing the electrical properties of the junctions to be stable as shown in Fig. III-1(d). Conducting AFM was performed, as described in section II.3 above, on individual pads to produce I-V curves for the individual metal-molecule-metal junctions as shown in Fig. III-2. These I-V measurements were found to be highly repeatable, with up to 96% of the MMM junctions having tunneling-shaped I-V curves. The remaining 4% of curves were electrically shorted, with an occasional junction having a resistance as much as 1000 times higher than the average resistance. Possible causes of the shorted junctions are the nanotransfer pushing down into the SAM to contact the bottom gold film and defects in the SAM. Possible causes of the high resistance junctions are defects, impurities and/or other sources of bad contacts at the thiol/Au interface preventing or obstructing electron transmittance. The data from the defective junctions (4% of all the junctions) were discarded from further analysis since they do not show the intrinsic behavior of the junctions.

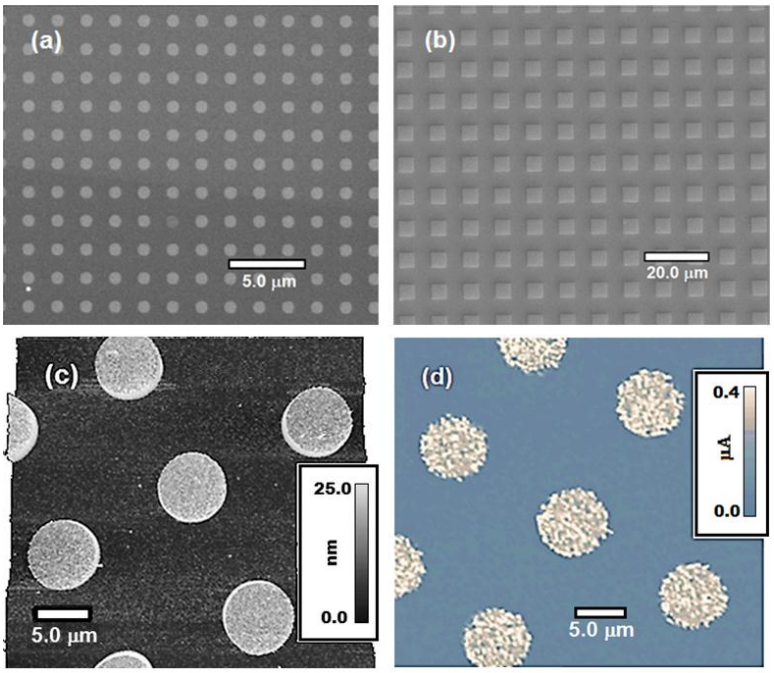

Figure III-1 Images of nTP arrays of Au-decanedithiol-Au junctions. (a) SEM image of 1 micron diameter junctions. (b) 5 micron square junctions (c) AFM images of 7 micron diameter junctions (d) conductive mapping at a sample bias of +1V.

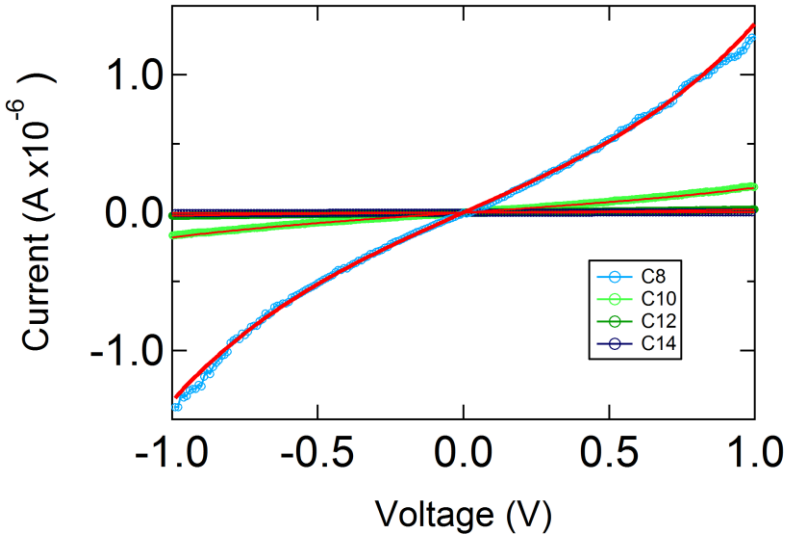

Figure III-2 Representative I-V curves taken by cAFM for different molecule lengths of the alkanedithiols. Red lines are Simmons model fits described in section III.4.

III.3. Dependence of Tunneling Characteristics on Molecular Length

The I-V behaviors of the Au-alkanedithiol-Au junctions fabricated by nTP as measured by cAFM show the characteristics of a nonresonant tunneling transport mechanism, the details of which are described in chapter 1. This type of transport behavior is consistent with results reported in previous studies[8]. To study the dependence on molecular length, 200 nm diameter nTP contacts on SAMs were chosen. The nTP contacts of this size were chosen because they produced I-V curves which gave consistent results for the area size when the area was allowed to be a free fitting parameter using the Simmons model. This is described in greater detail below

As shown in Fig. III-2, typical I-V curves are linear at low bias and become exponential at high bias. By plotting the curves on log-log scale as in Fig. III-3(a), it is clear the current exhibits exponential dependence on molecule length for any given bias. The curves show very good symmetry with respect to the direction of the bias voltage (open and closed symbols in Fig. III-3(a)), indicating that the two metal-thiol interfaces are nearly identical. The values of zero-bias resistance, R_0, have been determined from the slopes of the linear I-V behavior at low bias between +0.3V and -0.3V, and averaged for a given top contact size and molecular length, each from at least 50 independent junctions. The linearity of this low-bias regime is justified by examining the correlation coefficient of the linear term of a 3rd order polynomial fit. The linearity of this range is in agreement with results obtained in the literature.[9] The result for 200 nm diameter contacts is shown in Fig. III-3(b), demonstrating exponential dependence on molecular length.

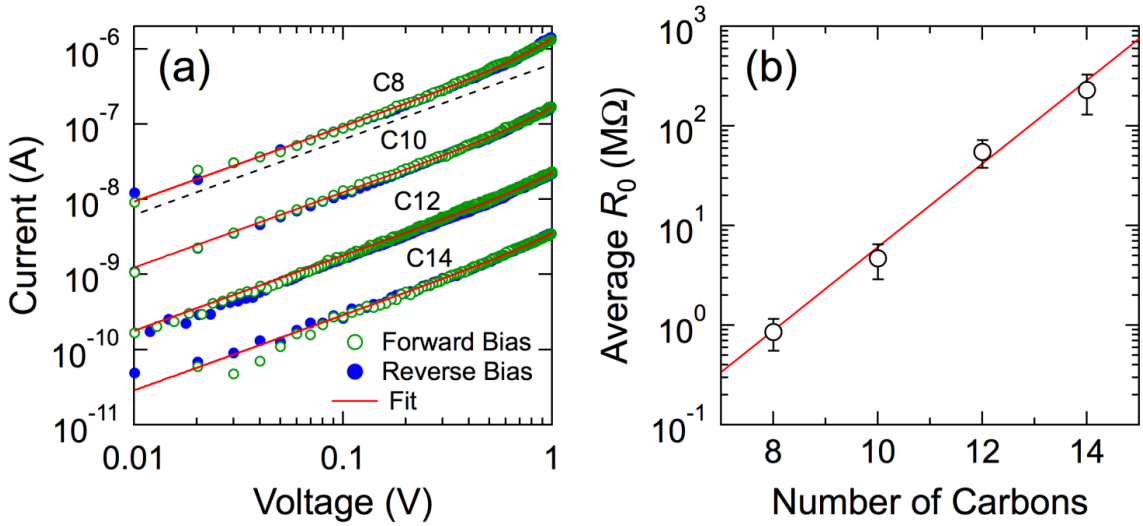

Figure III-3. Characteristic I-V behavior for 200 nm diameter nTP contacts versus molecular length in Au-alkanedithiol SAM-Au junctions. (a) Representative I-V curves (absolute values) for various alkane molecules. Open and closed circles indicate forward and reverse bias, respectively; the solid lines correspond to the Simmons model fits described in the text. The dashed line corresponds to linear behavior. (b) Averaged zero-bias resistance versus molecular length of alkane. The solid red line is a linear fit to the semilog plot.

III.4. Simmons Modeling of I-V Behavior

The I-V curves measured from the MMM junctions were analyzed using the Simmons model,[10,11] following the version modified by Wang *et al.*[12] In this model, the tunneling current through a thin layer of insulator between two metal contacts is given by

$$I = \left(\frac{qA}{4\pi^2 \hbar d_0^{\,2}}\right)\left\{\left(\Phi - \frac{qV}{2}\right)\exp\left[-\frac{2(2m)^{\frac{1}{2}}}{\hbar}\alpha\left(\Phi - \frac{qV}{2}\right)^{\frac{1}{2}} d_0\right]\right.$$

$$\left. -\left(\Phi + \frac{qV}{2}\right)\exp\left[-\frac{2(2m)^{\frac{1}{2}}}{\hbar}\alpha\left(\Phi + \frac{qV}{2}\right)^{\frac{1}{2}} d_0\right]\right\}, \qquad \text{Eq. (III.1)}$$

where A is the top printed contact/junction area, m and q are the respective electron mass and charge, d_0 is the distance between the two metal contacts, Φ is the barrier height of the insulator, α is an adjustable parameter to account for the effects of barrier shape and the electron effective mass within the insulator, and V is the bias. At low bias, the Simmons equation can be simplified, giving the zero-bias resistance as

$$R_0 = \left(\frac{8\pi^2 \hbar d_0}{A q^2 \beta_0} \right) \exp\left(\beta_0 d_0\right), \qquad \text{Eq. (III.2)}$$

where the tunneling decay coefficient β_0 is given by

$$\beta_0 = \frac{2\sqrt{2m}}{\hbar} \alpha \sqrt{\Phi}. \qquad \text{Eq. (III.3)}$$

In order to further examine the molecular tunneling barrier, the I-V measurements were fit to Eq. (III.1) using a Levenburg-Marquardt χ^2-minimization program. Specifically, Φ, α, and d_0 were the adjustable fitting parameters for the effective barrier height, shape, and width, respectively, whereas the contact area A was defined by the area of the top printed contact. The minimization algorithm not only converges slowly but also tends to reach various local χ^2-minima, owing in part to the presence of correlations between the parameters. To overcome the latter limitation, a statistical approach was employed, such that for each individual I-V curve, multiple fits were performed systematically with the initial values for each of the fitting parameters scanned over the respective range of literature values. The resulting parameters from the best fits (i.e., fits with the lowest χ^2 values) and their distributions were obtained, from which the best fit values for Φ, α, and d_0 were determined. The statistical approach is detailed as follows.

Statistical approach for Simmons model fits

As mentioned above, the use of the Simmons equation (III.1) in combination with the Levenburg-Marquardt χ^2-minimization programs used in conventional analytical software platforms to fit the I-V curves resulted in the limitations of slow convergence and different sets of parameters which the program considered to be a solution. Most of the analysis was done using the χ^2-minimization routine in Igor Pro, but the χ^2-minimization routine in Mathematica was also used and gave similar unsatisfactory results.

The reason for the multiple sets of solutions occurring is because there are strong correlations between the parameters of α, d_0, and A when all four fitting parameters of the Simmons model are allowed to be free in the fitting algorithm. The barrier height, Φ, is less strongly correlated to the other three parameters and therefore can be more easily and more reliably determined.

As a result of these correlations between parameters, the parameter differential space has a very low slope in a wide parameter space surrounding its minimum and thus parameters can be varied over a wide region with very little change to the χ^2 value. The Levenburg-Marquardt algorithm works by having to determine a slope in order to calculate how to change the parameters to move towards the minimum. In the absence of a change in slope as is the case in a wide minimum trough, the algorithm must make a large change to one of the parameters to find a sloping border of this trough. In other words, it has to

find a slope to begin with so that it can modify parameters in order to move towards a minimum based on the slope it found. This results in the algorithm repeatedly having to make relatively large changes to parameters, and this can sometimes result in the algorithm overshooting a true minimum.

In addition, again due to the correlation of the parameters, the parameter space could be thought of as a very low wide trough with the additional complication of having multiple smaller, low, wide basins of local minima interspersed throughout the flat plain of the trough. These local minima, though not the true minimum, are enough to satisfy the algorithm that it has found the true minimum. This is in part due to the way the algorithm has been programmed and in part due to practical limitations on computer power and time.

Because of the limits of the method as well as the limits of practicality, it was decided to select a range of starting values for each of the parameters and to step sequentially through each of these values, thus allowing for all possible combinations of these values as the starting point for the algorithm. In this way, the probability of the algorithm jumping into the true minimum, when making its iterative correction to the parameters, was greatly increased. Thus, by charting the resultant statistics of the algorithm's low-χ^2 results, distributions were generated. Based on the assumption that the algorithm would successfully (1) move towards and (2) sometimes find the true minimum more often than not, the resulting probability distribution should show increased number of points surrounding the true parameter value.

A test was created to determine the validity of the method. First, the Simmons equation was used to create an I-V curve. This I-V curve was then fit using the method. Each time the fitting algorithm was run by the program, it found a local minimum, but not necessarily the same one as it would find with a different set of starting values. This verified the need for the statistical approach, since even with an I-V curve generated by the equation itself, the true input parameters could not be determined. When the statistical approach was employed, probability distributions with peaks at the true input values used to create the curve to be tested were indeed found (see Figure 4). For five test curves, the barrier height was found exactly to within 1% of its actual input value every time, while α, d_0 were within 5% and the area within 10%. The reliability for the barrier height Φ is the best because it is less strongly correlated to the other three variables, which are each correlated to each other.

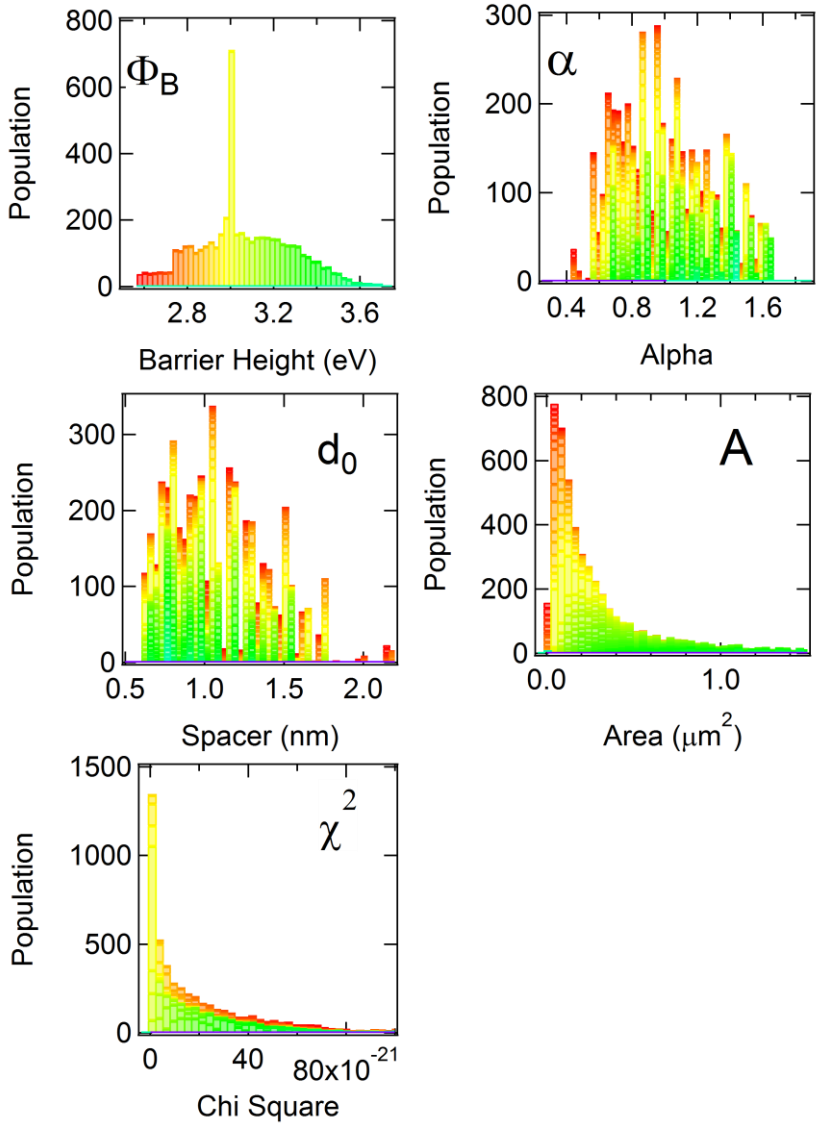

Figure III-4. Statistical distributions of Simmons model parameters based on a collection of fits that were backfitted to an I-V curve generated using the Simmons equation (1). The barrier height Φ shows a clear distribution and peak at the true value. Colors correspond to a range of the barrier height values Φ. The colors show where the bin values for Φ become distributed for the other parameters.

As seen in Fig. III-4, is clear that for a given Φ value, the other parameters are distributed through their range of values (e.g. yellow colored points corresponded to the Φ peak are actually widely dispersed in the plot for d_0). This results because of the correlation

of parameters. Next, in order to make use of the peak value for Φ, each set of four parameter values that includes the peak Φ value is then used to make another set of distributions. From these peak values, the final fits are obtained. In this way, the initial input values to the original equation could be found again by the backfitting method.

As can be seen in the plots in Fig. III-4, the distributions for the area do not follow the same general distribution pattern as the other parameters. The area follows a log-normal distribution, while α and d follow a Gaussian distribution. This is due to the linear dependence of current on the area parameter the Simmons equation (III.1). As mentioned above, the method of analyzing the peak from the statistical distribution was only successful in finding the area to better than 10% from the actual value, whereas greater accuracy was obtained from the other parameters.

Nonetheless, in an initial investigation, the area was allowed to be a free parameter in the fits for I-V curves from many different pad sizes using the statistical method. Unlike the other pad sizes, fits of the 200nm area I-V curves returned 100% area coverage within statistical error for all of the fits. This result is given greater credibility by the AFM image data, which showed the area for the 200nm pads to be consistently of very high uniformity – unlike the other, larger pad sizes. Beyond these initial indications provided by the free-parameter study, it was additionally proven, based on subsequent analysis of the electronic measurements presented in this chapter, to be justifiable to keep the area fixed at the expected value for 200nm pads.

When the Simmons fits were done for the actual I-V curves, with the area held fixed at 200nm diameter, the parameter space was scanned as described above, and histograms similar to those shown for the backfitting analysis were generated for Φ, α, and d_0. The lowest χ^2 results were plotted as a distribution as shown in Figure 4. From these distributions, the peak values were determined. The peaks represent the highest frequency of occurrence of the individual parameter from all of the scans through the parameter space. These values are the ones which the fitting algorithm iterated towards since the scanning method has arrived at these values more often. A set of peak parameter values was determined for each junction. Multiple junctions of the same type (e.g. C8 or C12) could then be further analyzed in this way in order to obtain statistics. From the statistical results, conclusions could be reached about the electrical behavior of the molecule, as described in the next section.

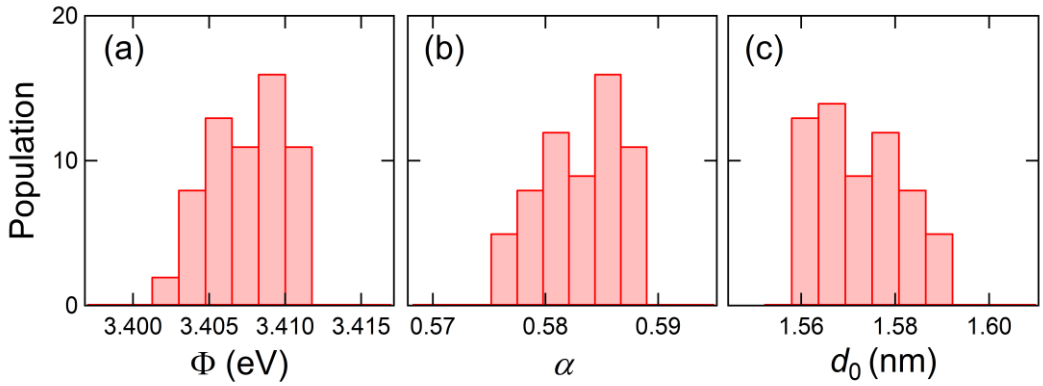

Figure III-5. Example of statistical distributions of Simmons model fits: histograms of the best-fit parameters (minimum χ^2) for an I-V curve obtained from a 200 nm diameter Au/C12-dithiol/Au junction. The measured I-V curve and the Simmons fit are shown in Fig. III-3. The best values for each I-V curve were obtained from the averages of the

distributions, and for this example they are: (a) Φ = 3.407 $\pm$ 0.003 eV, (b) α = 0.583 $\pm$ 0.004, (c) d_0 = 1.572 $\pm$ 0.009 nm at the minimum χ^2 values between 1.09538×10^{-16} and 1.09540×10^{-16}.

Results from the Simmons Model

The results of the analysis for junctions with 200 nm diameter nTP contacts are shown in Fig. III-6. The barrier height Φ increases with increasing molecular length, and as the carbon chain becomes longer than C12, the barrier height begins to saturate toward a value of 3.5 eV. The barrier shape parameter α, in contrast, exhibits an opposite trend with lengthening carbon chain: it decreases and then appears to saturate toward a value of 0.57. This observation suggests that the alkane chain has a higher tunneling barrier with a different shape (lower α value) than the thiol end groups. The spacer distance also decreases linearly with respect to the length of the carbon chain. This linear behavior for d_0 validates the analysis. It also makes it possible to obtain quantitative values for the size of thiol (d_{th}) and the projected spacing of each C-C perpendicular to the Au electrodes ($d_\perp$), i.e., $d_0 = N\,d_\perp + 2\,d_{th}$, where N is the number of carbons. Specifically, the vertical intercept of the linear fit (line in Fig. III-4(c)) at zero number of carbons (N = 0) gives a value of 0.60 $\pm$ 0.04 nm for $2d_{th}$ and thus 0.30 $\pm$ 0.02 nm for d_{th}, while the corresponding slope yields a projected C-C spacing perpendicular to the bottom Au electrode ($d_\perp$) of 0.081 $\pm$ 0.008 nm. The size of thiol (d_{th}) matches values in the literature, but $d_\perp$ is roughly 0.02 to 0.05 nm shorter than previously reported values.[13,14] It is generally accepted that alkanethiolates

form ordered ($\sqrt{3} \times \sqrt{3}$)R30° domains on Au films with the alkane chains oriented roughly 26 – 31° from normal (Fig. III-5(a)), as a result of van der Waals interactions.[15-19] Various calculated values for the unit length of alkyl along the alkane chain $d_{\parallel}$ have been reported,[13,14] ranging from 0.128 nm to 0.109 nm. Using these values combined with $d_{\perp}$ from our analysis, the corresponding tilt angle θ for the alkane chain resulting from the nTP process is determined (from $\cos q = d_{\wedge} / d_{\parallel}$) to be between 41° and 50°. The noticeably larger value is perhaps not surprising given the relatively forceful nature of the transfer printing process.

It is likely that the SAM layer becomes compressed under the printing force when the top Au electrode is pressed onto the receiving monolayer during printing. It is also possible for the SAM layer to collapse during printing, leading to "gauche-like" or other monolayer defects.[20] However, since this would lead to a very large number of shorted devices, this scenario is inconsistent with the small number of shorts measured in our MMM junctions and unlikely for the densely packed, crystalline-like SAMs produced in this study. The most probable SAM deformation in this system would be a systematic increase in the SAM's tilt angle from normal under the applied printing force. Several prior studies have demonstrated presence of an ordered tilt-chain deformation in SAM, where a SAM layer is compressed toward the substrate in a lever-like action under an externally applied force.[21-24]

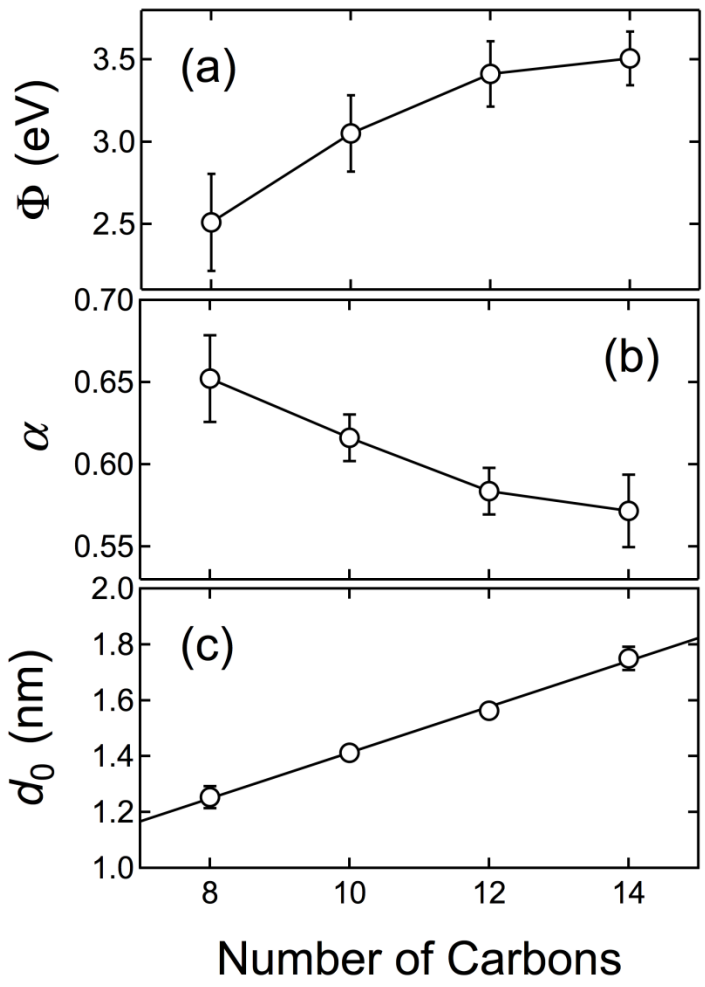

Figure III-6. Results of Simmons analysis: dependence of tunneling parameters on the length of alkane chain for Au-alkanedithiol-Au junctions with 200 nm diameter nTP Au contacts. The line in (c) is a linear fit to the points.

A simple multi-barrier model, where the alkane barrier is sandwiched between two identical thiol barriers, as depicted in Fig. III-7(b), can be used to model the behavior of the thiol and alkane portions of the molecule in the tunneling barrier.[25,26] For coherent tunneling through a series of barriers, the overall decay coefficient β_0 is related to the individual decay coefficients, β_{al} and β_{th} for alkyl and thiol, respectively, through the expression

$$\beta_0 d_0 = \beta_{\text{th}} d_{\text{th}} + \beta_{\text{al}} N d_{\perp} + \beta_{\text{th}} d_{\text{th}} . \quad (4)$$

Here, the effect of dielectric constants is neglected. By substituting Eq. (4) into the expression for R_0 in Eq. (2), it is evident that the slope of the linear fit in Fig. III-3(b) corresponds to the decay coefficient for alkyl β_{al} with a value of 0.98 $\pm$ 0.11 per $d_{\perp}$ or 1.21 $\pm$ 0.18 Å^{-1} (using $d_{\perp}$ from our analysis above). This value is consistent with those documented in the literature.[27-31] The values for the tunneling exponent, $\beta_0 d_0$, have also been determined from the Simmons fits (Fig. III-6), and the resulting dependence of $\beta_0 d_0$ versus the length of carbon chain is shown in Fig. III-6 for 200 nm diameter nTP junctions. From the line fit of the behavior, specifically from the slope and the vertical intercept of the fit, the respective values for β_{al} (again using $d_{\perp}$ from our analysis) and β_{th} have been determined. The results are β_{al} = 1.16 $\pm$ 0.10 Å^{-1} and β_{th} = 1.00 $\pm$ 0.14 Å^{-1}. The former decay coefficient agrees with our analysis for R_0 (above) and with literature values.[32,33] The excellent agreement further demonstrates the validity of our Simmons fits. However, the value for β_{th} is significantly higher than a previously reported value of 0.05 Å^{-1}.[13] The effects associated with a very low β_{th} are described in the discussion of tunneling parameters below.

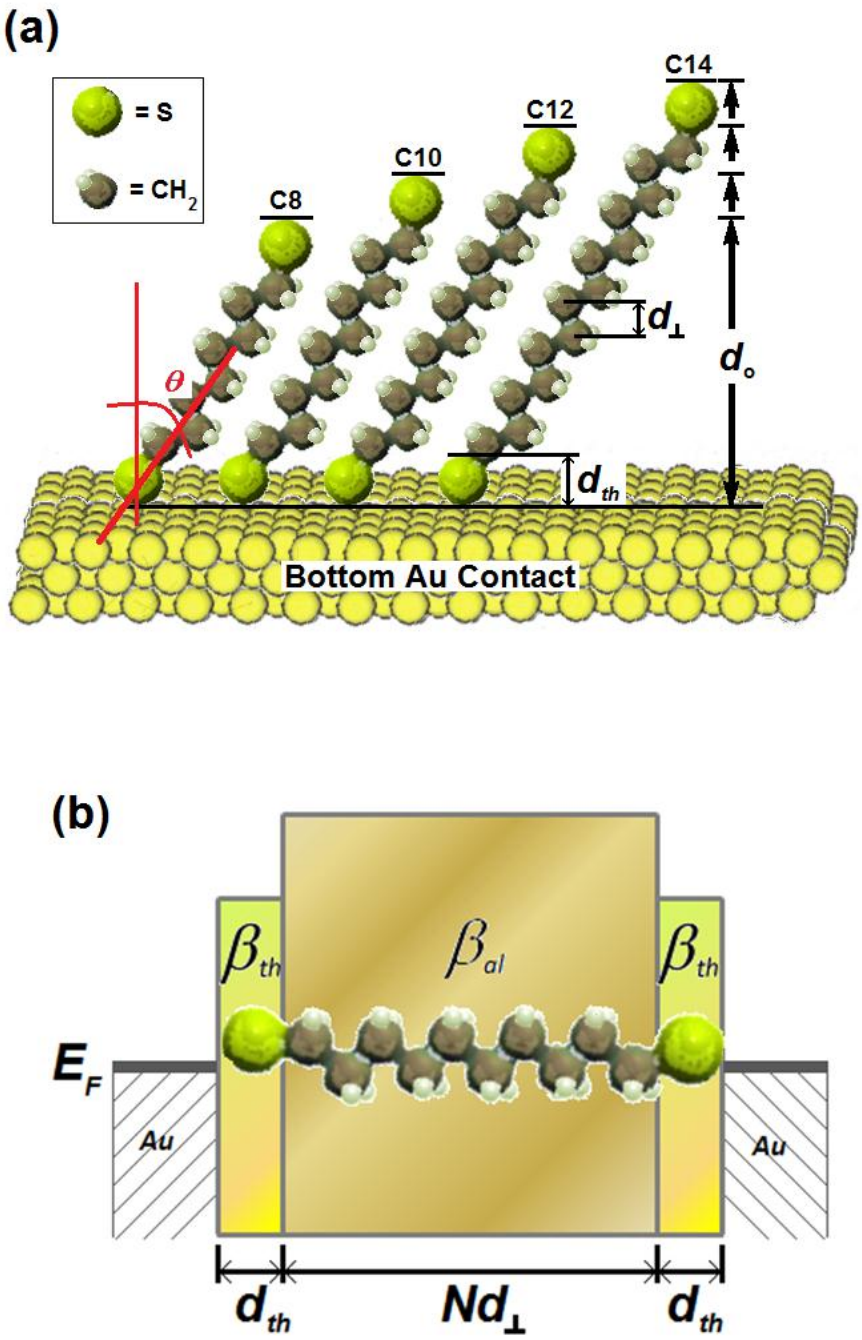

Figure III-7. Schematic diagrams of alkanedithiol monolayers on Au. (a) C8 – C14 alkandithiols on Au surface tilted by angle θ with dimensions d_{th}, $d_{\perp}$, and d_0 shown and defined in the text. (b) Multi-barrier tunneling model for alkanedithiol.[25,26] E_F is the Fermi energy of the Au electrodes.

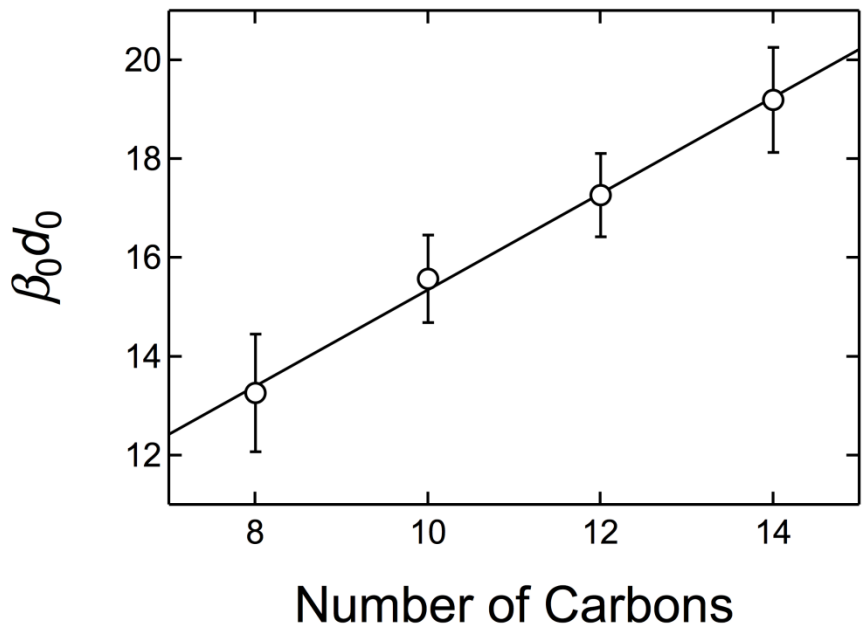

Figure III-8. Tunneling exponent versus the length of the alkane chain. The line is a linear fit of the points.

Using the results obtained for the Simmons fits relative to the length of the alkane chain, it is possible to separate out the parameters for the individual alkyl and thiol sections of the molecule. The trend in Figs. 4(a) and (b) can be extrapolated to determine values for the barrier height and the shape parameter α for alkyl and thiol. Extrapolated saturation values for the barrier height of 3.5 $\pm$ 0.2 eV and a value for α of 0.6 $\pm$ 0.1 have been determined. For the thiol, limiting cases of an upper bound of 2.4 eV for the barrier height and a lower bound of 0.65 for the shape parameter α are observed in the graph. A summary of tunneling parameters from our analysis is shown in Table 1. The barrier height for alkyl from this analysis is in good agreement with the theoretical values of about 3.5 to 5.0 eV expected from calculations of the molecular bandgap between HOMO (highest

occupied molecular orbital) and LUMO (lowest unoccupied molecular orbital).[34] These values are higher than those reported previously for the same molecules obtained by other techniques, including PEDOT:PSS protected junctions,[14,26] scanning/conductive probe techniques, [20,21,30,35,36] nanopores,[12] etc. all with reported values below 2.5 eV. In fact, only one result in the literature has a value higher at 5 $\pm$ 2 eV.[37]

While results from different measurement techniques may yield different precisions and uncertainties and may need to be analyzed differently, the most critical factor in determining transport processes through MMM junctions is the nature of the interface between the molecules and the metallic contact. As reported by Wang et al.,[26] the current density through MMM junctions with the top Au electrodes produced by thermal evaporation directly on the molecules was determined to be three orders of magnitude greater than those from junctions made with an intermediate layer of PEDOT:PSS. Introduction of an intermediate conducting polymer layer is a viable approach to prevent electrical shorting from migration of Au through the molecules, as it was first successfully implemented by de Boer et al.[38] However, in samples with a protective layer of PEDOT:PSS, the nature of the molecular barrier can be altered; for instance, the presence of PEDOT:PSS at the interface is known to lower the tunneling barrier in organic monolayers.[39] In contrast, samples with direct thermal deposition of metal on top of the SAM are prone to electrical shorting, with more than 98 % of such junctions shorted.[26,28] Furthermore, a very low value for the decay coefficient β_{th} (0.05 $Å^{-1}$)[13] indicates that the electron wave function is experiencing very little decay within the layers of thiol end groups. This and the above mentioned enhancement in conductivity, previously reported in the literature, strongly

suggest that Au nanostructures may have conglomerated around and covered the thiols and thus partially shorted them. It is reasonable to conclude that the interfaces in MMM junctions with the top electrodes fabricated from direct thermal deposition (including those involving nanopores)[12,40] are at best ill-defined, owing to Au migration and conglomeration through the molecules during deposition. Similarly, contacts made with cAFM tips on molecules are also ill-defined, since the tip geometry is generally uncontrolled and unknown. In short, various interfacial defects between metal contacts and molecules produced by different fabrication processes and measurement techniques can account for the variation in the reported tunneling parameters, and they generally tend to lower the observed tunneling barrier.

	β (Å^{-1})	Φ (eV)	α	d out-of-plane (nm)	θ (°)
Alkyl	1.16 ± 0.10	3.5 ± 0.2	0.6 ± 0.1	0.081 ± 0.003	41 - 50
Thiol	1.00 ± 0.14	2.4 *	0.65 **	0.30 ± 0.02	-

* Upper bound value. ** Lower bound value.

Table III.1. Summary of tunneling parameters obtained from the multi-barrier Simmons analysis. Decay coefficient (β), tunneling barrier height (Φ), shape parameter (α), and out-of-plane spacing ($d_{\perp}$ for alkyl and d_{th} for thiol) are separately listed for alkyl and thiol. The tilt angle for the alkane chain (θ) is with respect to the surface normal (Fig. III-5).

III.5. Dependence of Tunneling Characteristics on the Area of the Printed Au Electrode

Nanotransfer printing of electrodes on a self-assembled monolayer produces permanent and scalable metal-molecule-metal junctions. Electrodes can be made to have well-defined dimensions without the need for any sort of protection layer as has been used in previous devices of this type. The metal is made to contact the molecules directly, producing interfacial contacts on the top that exhibit symmetrical behaviors to those of the bottom. These identical interfaces are produced due to the thiol's affinity to form a strong bond with the metal. As a result of the symmetrical bonding, it is possible to examine the transport parameters of the alkanedithiols forming the middle layer. Consequently, because of the versatility of the printing technique, the lateral dimensions of the top electrode can also be changed, as shown in Fig. III-7, in order to systematically explore the dependence of the tunneling parameters on the area of the top electrode.

Hundreds of MMM junctions made with varying areas of the top electrode were made on SAMs of decanedithiol (C10) or tetradecanedithiol (C14). At least fifty junctions from at least three sample arrays were examined for each contact size by performing I-V measurements on the cAFM. Contact sizes range from 80nm circles to 7 micron squares. As shown in Fig. III-7, the tunneling current increases monotonically versus bias for each contact size. The changes in the current scale with the area as shown with a few exceptions. The 5 micron and 7 micron squares has a larger increase in current at high bias than the other I-Vs for the other pad sizes. When the low bias resistance R_0 is also examined, some additional details emerge about the nature of the printed pads.

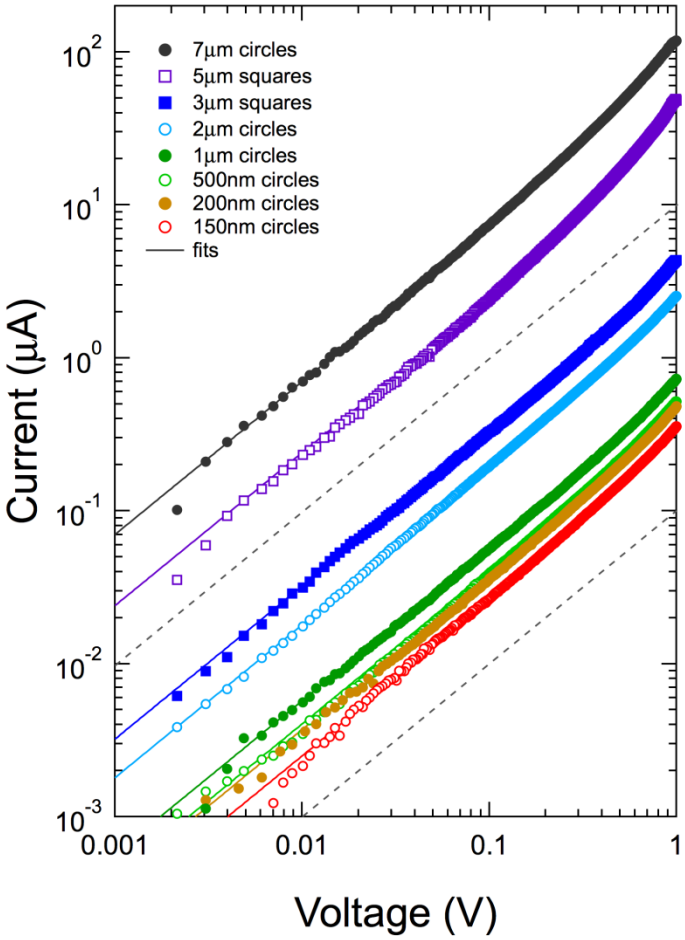

Figure III-9. Dependence of tunneling current on nTP contact size printed on decanedithiol SAMs, showing a monotonic increase of the current versus contact size. Results are shown for Au-decanedithiol-Au junctions. The solid, colored lines corresponds to Simmons fits of the I-V curves, while the two dashed lines are guide for the eyes to indicate the linear slope at low bias.

Values for R_0 are plotted in Fig. III-10 for the various pad sizes whose I-Vs are shown in Fig. III-9. Data for two different stamp types, a low viscosity PFPE and a high viscosity PFPE are shown for C10, and data for C14, made using the high viscosity PFPE, is also

shown, scaled by a factor to make it comparable to C10 for plotting. The resistance values for the pads can be organized into three regions. At low pad sizes, when the pads are less than or equal to those having 200 nm in diameter, there is a linear dependence of the resistance on the pad size in the plot. As area is increased, the resistance values level off and go through a region of no change with respect to area until reaching areas of 1 micron, where, depending on the type of stamp used, the resistance again resumes a linear increase with area in the third region. The linear increase of the third region is indicated by the dashed line in the plot. The data for C14 made using the high viscosity PFPE stamp is observed to scale very similarly to the comparable high viscosity PFPE C10. This behavior is expected based on Eq. (2) and (4).

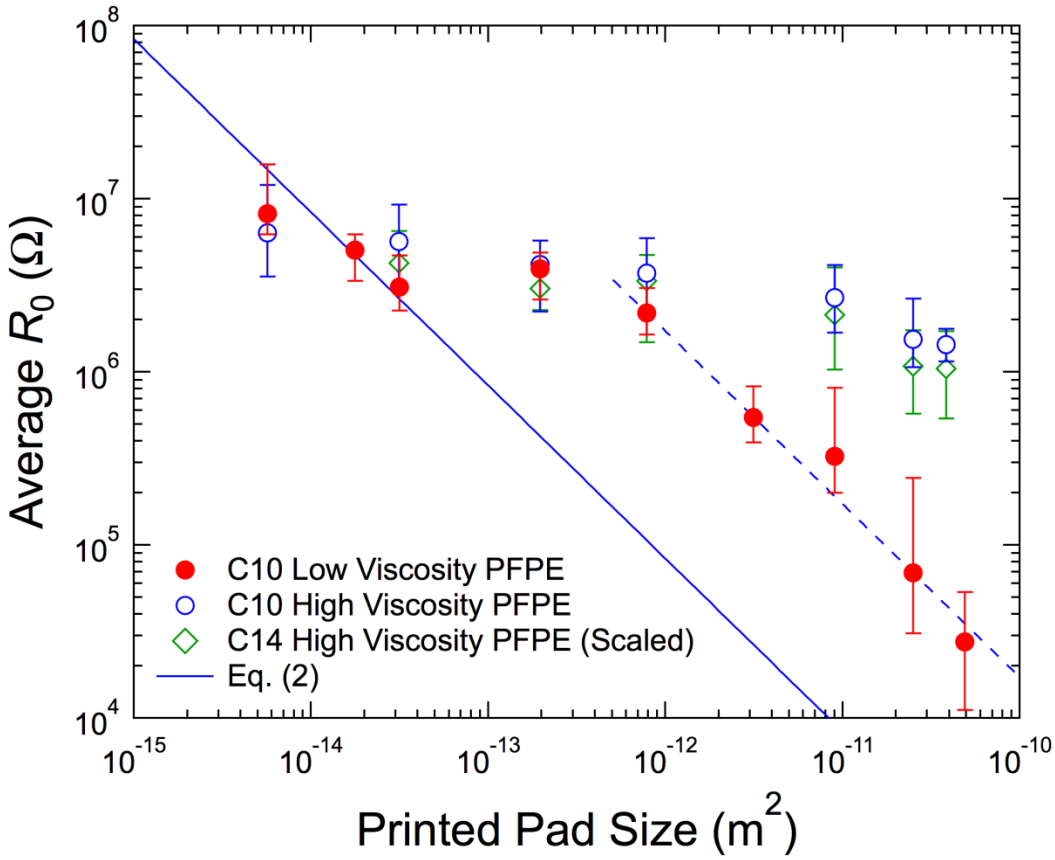

Figure III-10. Dependence of zero-bias resistance R_0 on the area of the nTP pads for decanedithiol (C10) and tetradecanedithiol (C14) and for different PFPE stamps. The solid blue line is the expected dependence based on Eq. 2 using parameters obtained from our analysis. The dashed blue line highlights an additional linear regime for C10 junctions transfer printed using low viscosity PFPE stamps. The points for C14 are scaled down by a factor of 46, which is equal to $\exp\left[\beta_{al}(14-10)d_{\perp}\right]$ (Eqs. (2) and (4)).

The individual resistance values shown in Fig. III-8 were obtained from a distribution of resistance values measured from a large number of samples (minimum of 50 for each pad size) as shown in the histograms of Figures 11 and 12. The distributions usually followed a log-normal distribution. The distributions become noticeably wider as the pad size becomes larger. The low viscosity PFPE also shows wider distributions than the high

viscosity PFPE. Log-normal fits were made to the distributions to determine peak values corresponding to the R_0 values shown in Fig. III-8. Details of these behaviors are described in the following section.

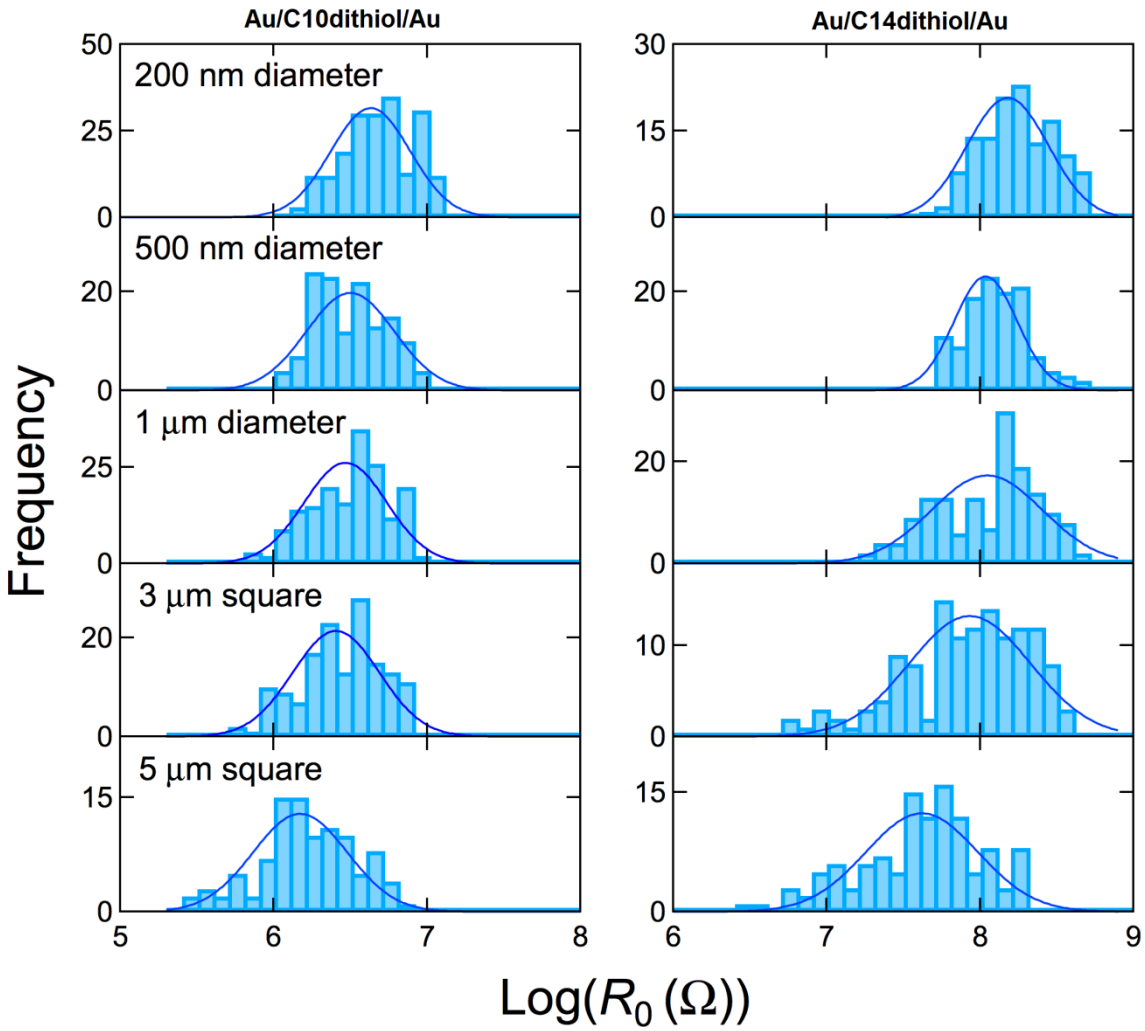

Figure III-11. Lognormal distributions of zero-bias resistance (R_0) for MMM junctions at various pad sizes (rows), transfer printed using high-viscosity PFPE stamps on decanedithiol (C10, left column) and tetradecanedithiol (C14, right column) monolayers. Lines are lognormal fits.

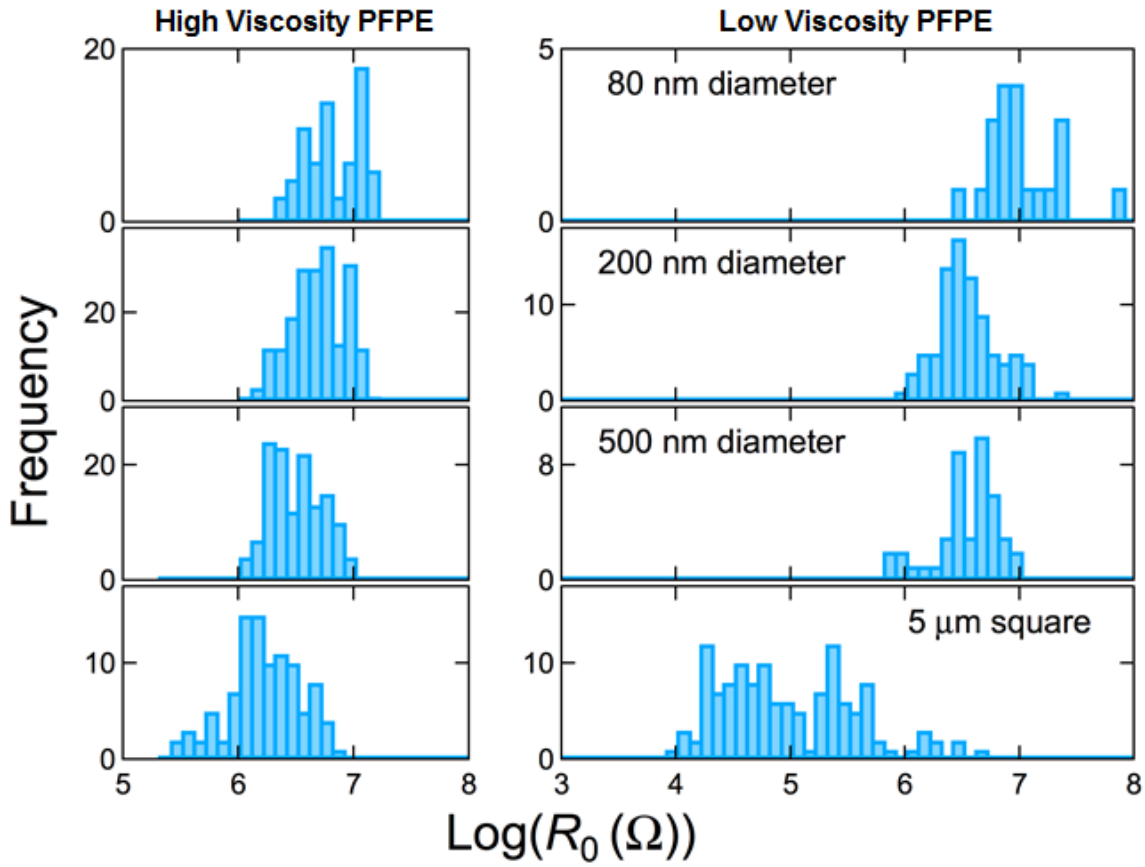

Figure III-12. Distributions of log of zero-bias resistance (R_0) for Au/decanedithiol/Au tunnel junctions versus nTP pad sizes (rows) with the pads made using two different types of stamps (columns): high-viscosity PFPE (left) and low-viscosity PFPE (right). As the pad size increases, the resistance decreases, with that for the low-viscosity PFPE showing a greater decrease. Both stamp types show a relatively constant width of distribution from 80 nm to 500 nm pad size, but at 5 microns the widths noticeably widen.

The behavior of the resistance values in Fig. III-8 with the three separate but distinct regions can be explained considering the nature of the transfer printing process. The resistance is determined not by the area of the pad on the stamp before printing, but by the effective contact area where the metal is actually making contact to the molecules beneath.

This effective contact area can be significantly smaller than the area of the printed pads when the pads get larger. For small pads, the effective contact area is roughly the same as the area of the pads (the first linear region), or in other words, the pads are contacting nearly 100% of the molecules. This result is confirmed by Simmons fitting when the area is allowed to be a free parameter, as mentioned above in the discussion about the Simmons analysis with all four parameters allowed to be free. As the pads get larger, the effective contact area first becomes constant (the plateau region), and then increases again (the second linear region), such that a fixed fraction of molecules under the pads (though << 100%) is contacted by the Au pads. This interpretation is also supported by the Simmons analysis.

The notion of a smaller effective contact area means that for each printed pad, there is a region where the molecules are actually bonding to the metal and another region where this is a gap between the metal pad and the molecules. Tunneling occuring through the latter region, a series of two barriers (molecules plus the gap), can be neglected to a good approximation, given that the measured current is likely dominated instead by tunneling through the other region where it goes directly through molecules.

It is important to understand the factors that determine the effective contact area and its dependence on the size of printed pads, and how these factors can be controlled, starting with the contact force during the nTP process.

The primary control during the transfer process is the tapping force applied (see Chapter 2). If the force is too little, no or partial transfer would occur, while an excessive applied force would lead to shorting between the top and bottom Au electrodes and/or

overprinting in areas between the intended features. Therefore, the optimized nTP process requires a narrow range of applied force, which also turns out to be roughly the same for all pad sizes within the limit of experimental control. As a result, the total mechanical contact force applied at the metal-molecule interface is essentially the same, since it is approximately the weight of the stamp (similar for different size pads) plus the applied tapping force.

Thus, within the plateau region of Fig. III-8, where the resistance is constant, the effective contact area is constant. This is likely the result of a constant contact force. This behavior is similar to what occurs when there is friction between two surfaces. Based on the conventionally known physics of a friction interaction, the frictional force is proportional to the normal force and independent of the macroscopic area in contact. However, as nanotribology studies have revealed, this is actually the case because the frictional force is proportional to the microscopic contact area between the two surfaces in contact.[41] The actual microscopic contact area is directly proportional to the normal force. Thus, the same contact force will produce the same the contact area regardless of the pad size.

The roughness of the two contacting surfaces also plays a significant role, in combination with nanotribological factors, in determining the microscopic contact area. However, the actual interfaces that result from the nTP process are difficult to determine experimentally. AFM and SEM experiments on surfaces before and after printing do provide some indication of the interface quality. As shown in Fig. III-9, the surfaces on small printed Au pads are relatively smooth with typical R_{RMS} values of about 4 nm, whereas the

larger printed pads (≥ 1 µm in lateral dimensions) are considerably rougher with cracks and folded ridges. For the larger pads, as the number of cracks and their lengths increase with the pad size, the R_{RMS} values also increase, from 4.4 nm to 5.0 nm to 5.5 nm for 3, 5, and 7 µm diameter features, respectively. There is no evidence that any cracks traverse an entire pad leading to electrically isolated regions within the pad. In contrast, the Au surfaces prior to transfer printing, i.e., those on the bottom Au electrode and those on the PFPE stamps, are significantly smoother with typical R_{RMS} values of 1.2 to 1.3 nm, as shown in Fig. III-11. The increased roughness, especially the cracking and folding, is likely a result of the force applied during the nanotransfer process. It is also possible that the nTP process promotes conformity at the metal-molecule interface which causes deformations in the top Au contact as the contact is applied to the SAM. There is no discernable difference in surface roughness between the Au surfaces on the two types of PFPE stamps, consistent with the comparable R_0 values (Fig. III-8) and their distributions at least for pad dimensions less than 1 µm (see the histograms in Figs. 9 and 10).

For the second linear region for R_0, where the behaviors for the two types of PFPE stamps deviate from each other, the mechanical properties of the printed Au pads and the PFPE stamps are the cause. When the pads are small, they are rigid like tiny plates, whereas large pads are flexible like sheets free to conform to the surface of the SAM. The change in rigidity also explains the corresponding change in R_{RMS} as the pad size becomes larger than 1 µm. The increased flexibility not only lets the printed pads be more conformal to the surface of SAM, but also allows them to crack, wrinkle and form networks of these, all of which lead to higher roughness, consistent with our microscopy measurements. As far as

the different elastic moduli for the two types of PFPE is concerned, it is suspected that the a different modulus would affect how the tapping force can be applied onto and through the nTP contact. The low-viscosity PFPE is formed from lower molecular weight precursors leading to a higher crosslink density and a higher elastic modulus (~ 7 MPa) when compared to those of the high-viscosity PFPE (~ 4 MPa). The stiffer stamps (low-viscosity PFPE), as opposed to the softer ones (high-viscosity PFPE), would enable the tapping force during nTP process to be more evenly distributed across each Au pad. This reduces the possibility for the conformal folding and wrinkling to occur. The result is a greater effective contact area and thus a lower resistance for the MMM junctions prepared with the low-viscosity PFPE stamp.

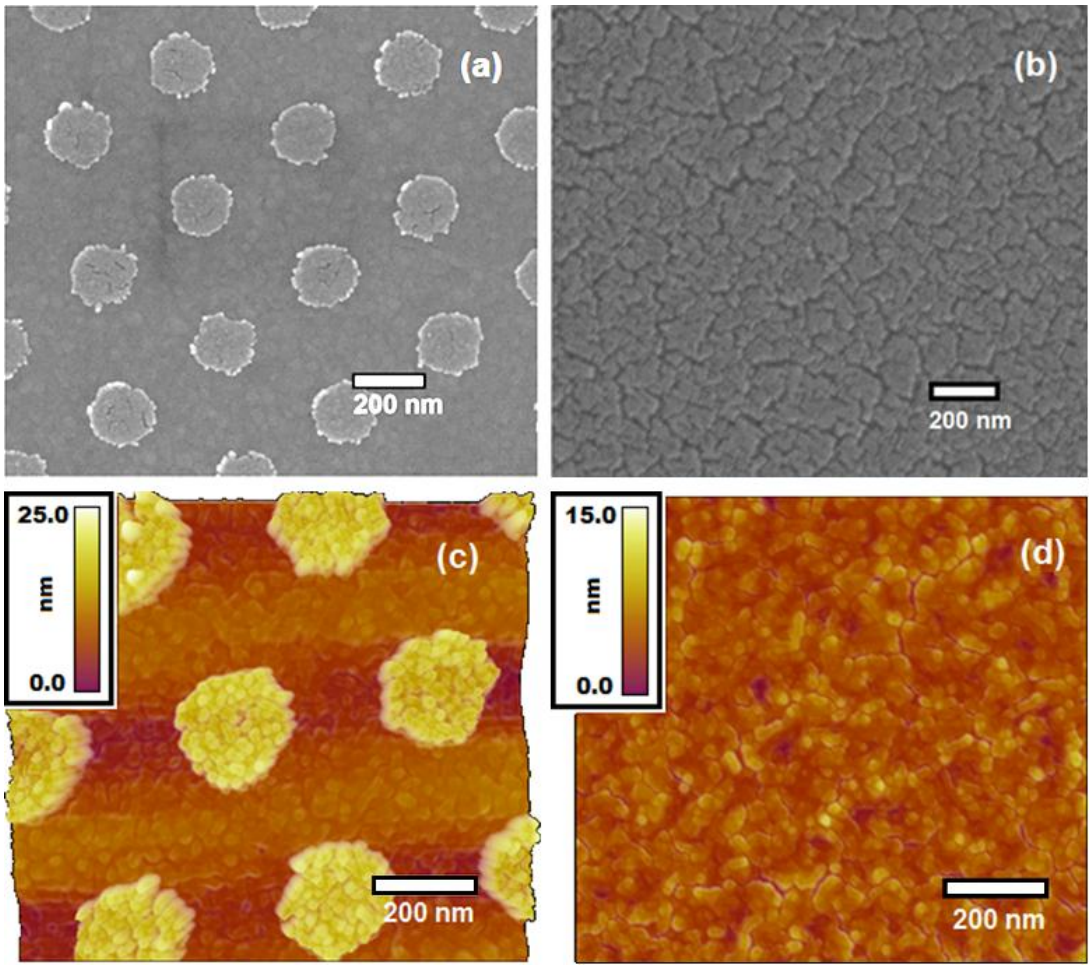

Figure III-13. Characteristic surfaces of various transfer printed features. SEM images of (a) 200 nm diameter contacts and (b) a zoomed-in region on a 7 µm diameter printed contact. AFM topography of (c) 200 nm diameter features and (d) a zoomed-in region on a 5 × 5 µm printed contact.

III.6. MOKE measurements of Metal-Molecule- Metal Junctions made with Ferromagnetic Metals

Nanotransfer-printed MMM junctions were also made using ferromagnetic metals to explore the possibility for their use in a spin valve. As previously demonstrated by this research, SAMs can be grown reliably on ferromagnetic bottom electrodes made from cobalt, iron, or nickel.[3] Ferromagnetic metal nanotransfer-printed top electrodes could be

made using the procedures described above, and the transfer printing was performed in the same way as for gold.

Using the Magneto-Optic Kerr Effect, it was determined that the individual layers of the top and bottom electrodes could be made to switch independently. This allows for the necessary parallel and anti-parallel conditions needed for a spin valve.

Subsequent to demonstrating that independent switching can be made to occur in an MMM junction have two ferromagnetic metal electrodes, devices of this sort were made using the permanent method for attaching leads as described in Chapter 2, so that they could be put into a magnetic field for magnetotransport measurement. Several devices were made; however, to date none have shown any significant magnetoresistance effects. This is likely due to problems associated with the photolithographic methods used.

Nonetheless, this important MOKE result lays the groundwork for future studies of spin-valves made using self-assembled monolayers. It proves that in spite of known problems with nTP pad roughness and cracking at larger pad sizes, the magnetization behavior of the bulk layer can still be preserved.

III.7. Conclusion

Nanotransfer printing was used to make MMM junctions from self-assembled monolayers of alkanedithiols. The nTP method is reproducible, stable and does not damage the molecules. In addition, a high-quality interface can be made that makes it possible to

explore the electrical properties of the alkane molecular chain and metal-molecule bond interface of the thiol. The MMM junctions produce symmetrical I-V behavior, indicating the nTP interface is identical to the metal-molecule interface beneath the monolayer. Analysis of I-Vs collected by cAFM was performed using the Simmons model, combined with a statistical approach to overcome limitations of the fitting algorithm. This analysis revealed quantitative tunneling parameters for the molecules, including the tunneling barrier heights, 3.5 ± 0.2 eV (alkane) and 2.4 eV (an upper bound value for thiol), and the corresponding decay coefficients, 1.16 $\pm$ 0.10 $Å^{-1}$ (alkane) and 1.00 $\pm$ 0.14 $Å^{-1}$ (thiol). These values are consistent with theoretical predictions. However, the alkane barrier height and the thiol decay coefficient are higher than those previously observed by other techniques. It is believed the improved interfacial quality between the SAM and the top printed Au electrode using the nTP process enables these more intrinsic measurements.

NTP electrodes could be made to vary in size with results consistent with scaling of resistances. Areas for the top contacts ranged from 80nm to 7 microns. It was determined that the resistances for the varying pad sizes scaled with an effective contact area instead of the actual contact area when the pad sizes exceeded lateral dimensions of hundreds of nanometers. This microscopic effective contact area is produced as a function of the tapping force of the nTP method, the roughness of the electrodes and mechanical properties of the stamps used.

In summary, the nTP method has enabled the characterization of electrical transport in alkanedithiol molecules made to form a self-assembled monolayer. This technique shows considerable promise for application to other self-assembled monolayers and systems of

molecules in order to expand knowledge and improve development of organic electronics and organic spintronics.

References

1 Niskala, J. & You, W. Metal-Molecule-Metal Junctions via PFPE Assisted Nanotransfer Printing (nTP) onto Self-Assembled Monolayers. *Journal of the American Chemical Society* **131**, 13202-+, doi:10.1021/ja9047152 (2009).

2 Niskala, J. N., Rice, W.C., Bruce, R.C., Merkel, T., Tsui, F., You, W. Tunneling Characteristics of Au-Alkanedithiol-Au Junctions formed via Nanotransfer Printing (nTP). *Journal of American Chemical Society* (2012).

3 Hoertz, P., Niskala, J., Dai, P., Black, H. & You, W. Comprehensive investigation of self-assembled monolayer formation on ferromagnetic thin film surfaces. *Journal of the American Chemical Society* **130**, 9763-9772, doi:10.1021/ja800278a|10.1021/ja800278a (2008).

4 Niskala, J. PhD Thesis, "Molecular Spintronics: Design, Fabrication, and Characterization". *University of North Carolina at Chapel Hill* (2010).

5 Loo, Y., Lang, D., Rogers, J. & Hsu, J. Electrical contacts to molecular layers by nanotransfer printing. *Nano Letters* **3**, 913-917, doi:10.1021/nl034207c|10.1021/nl034207c (2003).

6 Loo, Y. *et al.* High-resolution transfer printing on GaAs surfaces using alkane dithiol monolayers. *Journal of Vacuum Science & Technology B* **20**, 2853-2856, doi:10.1116/1.1523405|10.1116/1.1523405 (2002).

7 Lee, B. *et al.* High-resolution patterning of aluminum thin films with a water-mediated transfer process. *Advanced Materials* **19**, 1714-+, doi:10.1002/adma.200601884|10.1002/adma.200601884 (2007).

8 Akkerman, H., Blom, P., de Leeuw, D. & de Boer, B. Towards molecular electronics with large-area molecular junctions. *Nature* **441**, 69-72, doi:10.1038/nature04699|10.1038/nature04699 (2006).

9 Beebe, J., Engelkes, V., Miller, L. & Frisbie, C. Contact resistance in metal-molecule-metal junctions based on aliphatic SAMs: Effects of surface linker and metal work function. *Journal of the American Chemical Society* **124**, 11268-11269, doi:10.1021/ja0268332|10.1021/ja0268332 (2002).

10 Simmons, J. G. Generalized Formula for the Electric Tunnel Effect between Similar Electrodes Separated by a Thin Insulating Film. *Journal of Applied Physics* **34**, 1793-1803 (1963).

11 Simmons, J. G. Electric Tunnel Effect between Dissimilar Electrodes Separated by a Thin Insulating Film. *Journal of Applied Physics* **34**, 2581-2590 (1963).

12 Wang, W., Lee, T. & Reed, M. A. Mechanism of electron conduction in self-assembled alkanethiol monolayer devices. *Physical Review B* **68**, 035416 (2003).

13 Wang, G., Kim, T.-W., Jang, Y. H. & Lee, T. Effects of Metal-Molecule Contact and Molecular Structure on Molecular Electronic Conduction in Nonresonant Tunneling Regime: Alkyl versus Conjugated Molecules. *The Journal of Physical Chemistry C* **112**, 13010-13016 (2008).

14 Akkerman, H. B. *et al.* Electron Tunneling Through Alkanedithiol Self-Assembled Monolayers in Large-Area Molecular Junctions. *Proceedings of the National Academy of Sciences* **104**, 11161-11166, doi:10.1073/pnas.0701472104 (2007).

15 Poirier, G. E. Characterization of Organosulfur Molecular Monolayers on Au(111) using Scanning Tunneling Microscopy. *Chemical Reviews* **97**, 1117-1128 (1997).

16 Love, J. C., Estroff, L. A., Kriebel, J. K., Nuzzo, R. G. & Whitesides, G. M. Self-Assembled Monolayers of Thiolates on Metals as a Form of Nanotechnology. *Chemical Reviews* **105**, 1103-1170 (2005).

17 Schreiber, F. Structure and Growth of Self-Assembling Monolayers. *Progress in Surface Science* **65**, 151-257 (2000).

18 Ulman, A. Formation and Structure of Self-Assembled Monolayers. *Chemical Reviews* **96**, 1533-1554 (1996).

19 Luca, M. G., Riccarda, C. & Luigi Delle, S. Alkanethiol headgroup on metal (111)-surfaces: general features of the adsorption onto group 10 and 11 transition metals. *Journal of Physics: Condensed Matter* **19**, 176004 (2007).

20 Li, C. *et al.* Charge Transport in Single Au | Alkanedithiol | Au Junctions: Coordination Geometries and Conformational Degrees of Freedom. *Journal of the American Chemical Society* **130**, 318-326 (2008).

21 Wang, G., Kim, T.-W., Jo, G. & Lee, T. Enhancement of Field Emission Transport by Molecular Tilt Configuration in Metal-Molecule-Metal Junctions. *Journal of the American Chemical Society* **131**, 5980-5985, doi:doi:10.1021/ja900773h (2009).

22 Barrena, E., Ocal, C. & Salmeron, M. Molecular packing changes of alkanethiols monolayers on Au(111) under applied pressure. *The Journal of Chemical Physics* **113**, 2413-2418 (2000).

23 Barrena, E., Ocal, C. & Salmeron, M. Structure and stability of tilted-chain phases of alkanethiols on Au(111). *The Journal of Chemical Physics* **114**, 4210-4214 (2001).

24 Slowinski, K., Chamberlain, R. V., Miller, C. J. & Majda, M. Through-Bond and Chain-to-Chain Coupling. Two Pathways in Electron Tunneling through Liquid Alkanethiol

Monolayers on Mercury Electrodes. *Journal of the American Chemical Society* **119**, 11910-11919, doi:10.1021/ja971921l (1997).

25 Wang, G., Kim, T.-W., Lee, H. & Lee, T. Influence of Metal-Molecule Contacts on Decay Coefficients and Specific Contact Resistances in Molecular Junctions. *Physical Review B* **76**, 205320 (2007).

26 Wang, G. *et al.* Electrical Conduction Through Self-Assembled Monolayers in Molecular Junctions: Au/Molecules/Au versus Au/Molecules/PEDOT:PSS/Au. *Thin Solid Films* **518**, 824-828 (2009).

27 Xu, B. & Tao, N. J. Measurement of Single-Molecule Resistance by Repeated Formation of Molecular Junctions. *Science* **301**, 1221-1223, doi:10.1126/science.1087481 (2003).

28 Kim, T.-W. & et al. Statistical analysis of electronic properties of alkanethiols in metal–molecule–metal junctions. *Nanotechnology* **18**, 315204 (2007).

29 Akkerman, H. B. & Boer, B. d. Electrical Conduction Through Single Molecules and Self-Assembled Monolayers. *Journal of Physics: Condensed Matter*, 013001 (2008).

30 Engelkes, V. B., Beebe, J. M. & Frisbie, C. D. Length-Dependent Transport in Molecular Junctions Based on SAMs of Alkanethiols and Alkanedithiols: Effect of Metal Work Function and Applied Bias on Tunneling Efficiency and Contact Resistance. *Journal of the American Chemical Society* **126**, 14287-14296 (2004).

31 Salomon, A. *et al.* Comparison of Electronic Transport Measurements on Organic Molecules. *Advanced Materials* **15**, 1881-1890 (2003).

32 Wold, D. J. & Frisbie, C. D. Fabrication and Characterization of Metal−Molecule−Metal Junctions by Conducting Probe Atomic Force Microscopy. *Journal of the American Chemical Society* **123**, 5549-5556, doi:10.1021/ja0101532 (2001).

33 Cui, X. D. *et al.* Making electrical contacts to molecular monolayers. *Nanotechnology*, 5 (2002).

34 Tomfohr, J. K. & Sankey, O. F. Complex Band Structure, Decay Lengths, and Fermi Level Alignment in Simple Molecular Electronic Systems. *Physical Review B* **65**, 245105 (2002).

35 Wold, D. J., Haag, R., Rampi, M. A. & Frisbie, C. D. Distance Dependence of Electron Tunneling through Self-Assembled Monolayers Measured by Conducting Probe Atomic Force Microscopy: Unsaturated versus Saturated Molecular Junctions. *The Journal of Physical Chemistry B* **106**, 2813-2816, doi:doi:10.1021/jp013476t (2002).

36 Li, X. *et al.* Conductance of Single Alkanedithiols: Conduction Mechanism and Effect of Molecule−Electrode Contacts. *Journal of the American Chemical Society* **128**, 2135-2141, doi:10.1021/ja057316x (2006).

37 Xu, B. & Tao, N. Measurement of single-molecule resistance by repeated formation of molecular junctions. *Science* **301**, 1221-1223, doi:10.1126/science.1087481 (2003).

38 Akkerman, H. B., Blom, P. W. M., de Leeuw, D. M. & de Boer, B. Towards Molecular Electronics with Large-Area Molecular Junctions. *Nature* **441**, 69-72 (2006).

39 Koch, N. *et al.* Conjugated organic molecules on metal versus polymer electrodes: Demonstration of a key energy level alignment mechanism. *Applied Physics Letters* **82**, 70-72 (2003).

40 Song, H., Lee, T., Choi, N.-J. & Lee, H. A Statistical Method for Determining Intrinsic Electronic Transport Properties of Self-Assembled Alkanethiol Monolayer Devices. *Applied Physics Letters* **91**, 253116-253116-253113 (2007).

41 Krim, J. Friction at the Atomic Scale. *Scientific American* **275**, 74-80 (1996).

Chapter IV: Valence Tautomeric Switching Behavior in a Spin Valve

Valence tautomer molecules made from complexes of cobalt dioxolenes have been studied over the past couple of decades for their unique ability to transition between two stable magnetic forms as a result of a change in temperature, light, or pressure. They belong to a class of molecules called spin crossover compounds which are capable of undergoing a change between two different total spin states. Based on the different spin states, the molecules can exhibit two different magnetic behaviors. SQUID measurements done by collaborators have shown that valence tautomeric molecules are paramagnetic in their higher spin form, but diamagnetic in their low spin form.[1] There is considerable interest in exploiting this magnetic transition behavior for use in molecular spintronics. Although a significant amount of research has been completed in characterizing the transitional behavior of the tautomer, until now not much research has been done to explore its transport behavior with the goal of integrating the molecules into an electronic device. The work presented in this chapter examines the magnetotransport of the molecule and yields new findings that show promise for a unique molecular spintronic application.

Molecular spin valve structures have been studied for the past decade[2] for the potential advantage provided by a molecular spacer layer: controllable magnetism. All-organic spin valves making use of organic electrodes have recently been reported,[3] in addition to spin filters made from molecular layers.[4] The mechanisms of a spin valve, in addition to some of the

important general considerations for molecular systems, are described in greater detail in Chapter 1. A spin filter is a device which makes use of the spin polarization of the molecular layer to influence the transport. It is envisioned that a single layer of a bi-stable molecule like a valence tautomer (VT), exhibiting a change in spin state, can be connected to a single ferromagnetic contact to make a device having its magnetotransport behavior controllable by temperature, light or pressure. Additionally, very recent investigations suggest that an electric field can be used control the magnetic switching.[5]

In the following chapter, the discussion will explain how a spin-valve structures were made from valence tautomer films, followed by results obtained from the spin valves. The focus will then turn to a spin valve that demonstrated distinctive switching behaviors as a result of the molecule's intrinsic valence tautomeric transition, and the exact nature of those switching behaviors will be analyzed.

IV.1. Review of Valence Tautomer Properties and Characteristics

Although many different varieties of the valence tautomer molecule can be made, each having their own separate transition temperatures which can range from as low as 80K to above room temperature, this study focuses on one type, a valence tautomer made from a complex of cobalt dioxolenes with cyanopyridine ancillary groups. The known tautomeric transition is caused by an intramolecular ligand-metal charge transfer that is coupled with a metal-based spin crossover. The conversion is accompanied by an increase in the total spin of the molecule from S=1/2 in a low-spin Co(III) form to S=5/2 in a high-spin Co(II), and a molecular expansion due to bond length elongation. Extensive studies completed prior to this

work on this and other valence tautomer molecules, including synthesis and magnetic susceptibility measurements, were done by collaborators in the Shultz group in Chemistry at North Carolina State University. Reference is made to their prior work on the subject.[1]

Valence tautomerism is an equilibrium process, characterized by a metal-ligand electron transfer, coupled with a metal-based spin-crossover. As a consequence of the electron transfer, the metal undergoes a spin-crossover, meaning the metal not only changes oxidation, but also spin state, from low to high spin or high to low spin. This interaction is shown in Figure IV-1, which illustrates the potential energy wells of the states associated with the two bistable forms. Valence tautomeric molecules typically consist of two redox active, organic ligands bridged by a paramagnetic metal center, with ancillary ligands completing the coordination sphere.[6]

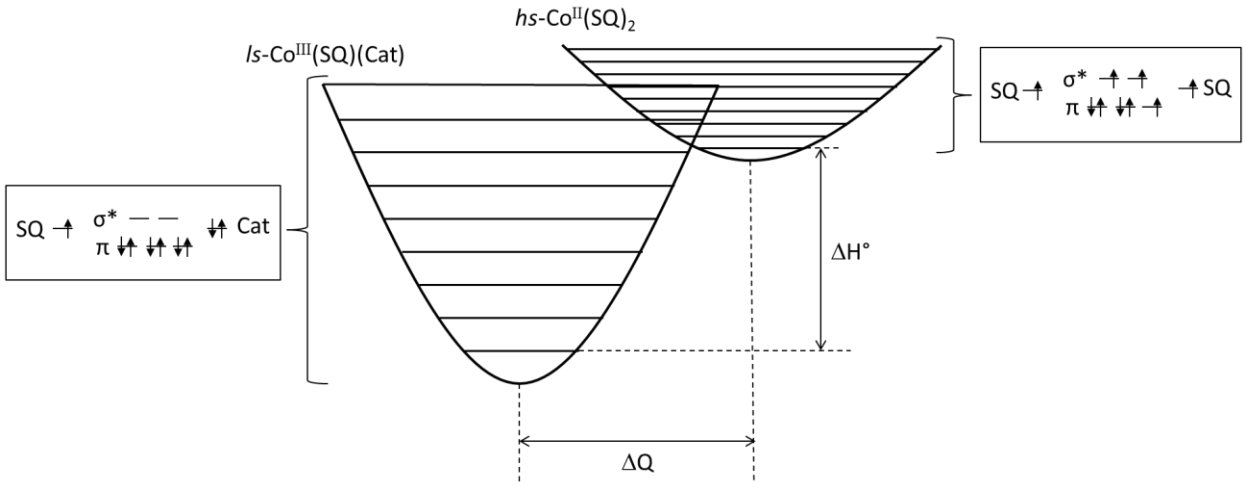

Fig. IV-1 Diagram showing the energy potential wells corresponding to the two bistable forms of a valence tautomer molecule. The low spin Co(III) form has a deeper well with wider spacing between the energy levels, while the high spin Co(II) form has a shallower well with more densely packed energies. This is a result of the additional vibrational modes arising from the formation of the second semiquinone out of catechol at higher temperature. Molecular orbital occupations for the two forms are shown in the small boxes.

In the VT complexes, the quinone ligand orbitals are close enough in energy to the metal orbitals, and can either donate or accept electrons, depending on the oxidation states. This is a temperature dependent phenomenon, and as such the metal centers change d-orbital occupation with temperature, satisfying the spin-crossover. In Co-based molecules, this means that the low temperature form, *ls*-Co^{III} has the configuration $(t_{2g})^6(e_g)^0$, and the high temperature form, *hs*-Co^{II} has the configuration $(t_{2g})^5(e_g)^2$. The population of the σ^* orbitals in the *hs*-Co^{II} form will result in longer metal-ligand bond lengths. Also, as shown in Fig. IV-1 above, the vibrational levels of the *hs*-Co^{II} state are very densely packed, which translates into a large increase in entropy with conversion to the *hs*-Co^{II} form.

When two spin states have approximately equal enthalpies, H, but different entropies, S, ΔG° can change sign within a readily attainable temperature range. The entropic driving force is vibrational. The entropy-driven transition is controlled by the relative Gibbs free energy between the high-spin and low-spin states:

$$\Delta G = G_{HS} - G_{LS} = \Delta H - T\Delta S \qquad (1)$$

where $\Delta H = H_{HS} - H_{LS}$ and $\Delta S = S_{HS} - S_{LS}$ are the respective enthalpy and entropy difference. $\Delta G > 0$ means that the thermodynamically stable configuration is low-spin. In spin-crossover molecules, as in valence tautomers, $\Delta H > 0$ but $S_{HS} > S_{LS}$ so that as the temperature increases, the entropic term $T\Delta S$ dominates over the enthalpic one. This lowers the Gibbs energy, causing the molecules to transition from low-spin to high-spin. The microscopic mechanism for the spin crossover consists in moving an electron from a

nonbonding to an antibonding state. The transfer produces the breathing of the metal ion coordination sphere with consequent phonon modes softening. Thus, both the spin and the vibrational entropy of the high-spin state dominate over those of the low-spin ones.[5]

IV.2. Structure of Spin-valves made with Valence Tautomers

Ferromagnetic metal – molecule – ferromagnetic metal junctions were prepared as described in detail in Chapter II using permalloy and cobalt as the two electrode metals. The design makes use of crossbar contacts which form a vertical stacked structure, a cross-section of which is shown in Fig. IV-2. By connecting leads to the crossbars, four-terminal I-V and differential conductance measurements were performed in a low-temperature flow cryostat under a variable magnetic field. The magnetic field direction is perpendicular to the current direction, in the plane of the layers. By making the entire stack on a glass slide with a thin bottom contact (25nm Au/20nm permalloy), light can be transmitted through the glass slide and the bottom contact, so that it reaches the approx. 25nm-thick VT layer. Thus, the light-induced transition in the VT can be generated. The cobalt top layer is 100nm, followed by a Au capping layer of 100nm. When examining samples, individual crossbar devices were first checked on the probe station in atmosphere to find a working device. Subsequently, leads were attached and the sample mounted in the flow cryostat. The junctions were measured by magnetic field scans in the cryostat to explore for magnetoresistive effects at varying temperatures.

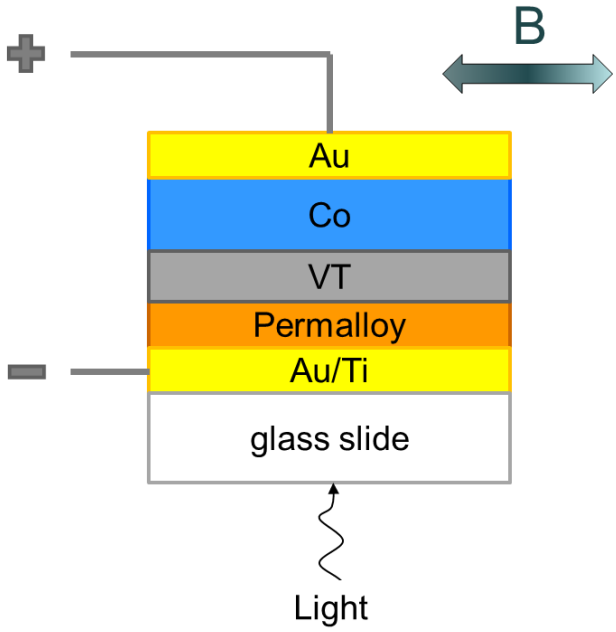

Fig. IV-2 Magnetic tunnel junction of Co-VT-permalloy made as a vertical stacked structure. Crossbars to perform a four-terminal measurement were made with an additional gold layer provided for increased conductance. The entire structure was made on a glass slide so that light could be transmitted through the transparent bottom permalloy layer in order to reach the VT. The magnetic field direction is in the plane of the electrodes, perpendicular to the current direction.

The specific mechanism of the VT-transition can be described by the change in molecular structure shown in Fig. IV-3. Once there is a sufficient thermal energy or energy from a photon, the bonding arrangement of the catechol changes so that the double bond between the two carbons bonded to the oxygens becomes a single bond, and now a double bond can form between one of these carbons and an oxygen of the cobalt ligand. This creates the double bond and a second semiquinone. The additional energy of the electrons in this bonding structure allows them to reach higher, previously unoccupied molecular orbital sites, which they fill as unpaired single electrons. These unpaired electrons cause the greater magnetic susceptibility and contribute to the paramagnetic behavior.

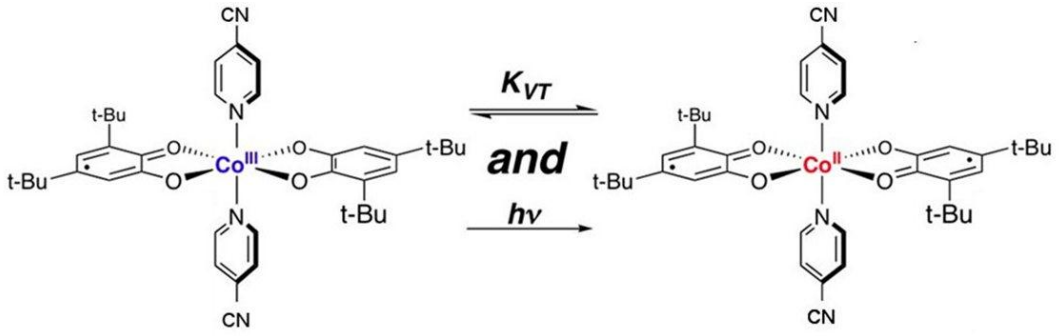

Fig. IV-3 Molecular structure of the two forms of the cyanopyridyl valence tautomer. The low-spin Co(III) form (left) transitions to the high-spin Co(II) form when the temperature increases above the transition temperature, or when light is applied.

Optimization of Spincoating Procedure for making Valence Tautomer Thin Films

At first, samples having high resistances were desired. An initial study using samples made from gold electrodes had shown that samples with R_0 values in the kiloohm range could routinely be achieved. These samples demonstrated interesting effects based on temperature. It was expected that these same resistance values could also be obtained in the ferromagnetic-insulator-ferromagnetic (FM-I-FM) devices by spincoating the VT layer. However, initial batches revealed that the VT resistances were lower.

In an attempt to obtain devices that were not only higher in resistance, but also had a range of resistance values so that a comparative study could be performed based on thickness as a variable, variations were made to the spincoating parameters used to prepare the thin films.

One of these variations was using different solvents. To increase thickness, dichloromethane was used as a solvent since it is one of the solvents into which the tautomer dissolves with the greatest concentration. However, as shown in Fig. IV-4, the resulting

resistance values tended to stay in two separate ranges, low (<100 Ω) or high (> 1 TΩ, open circuit).

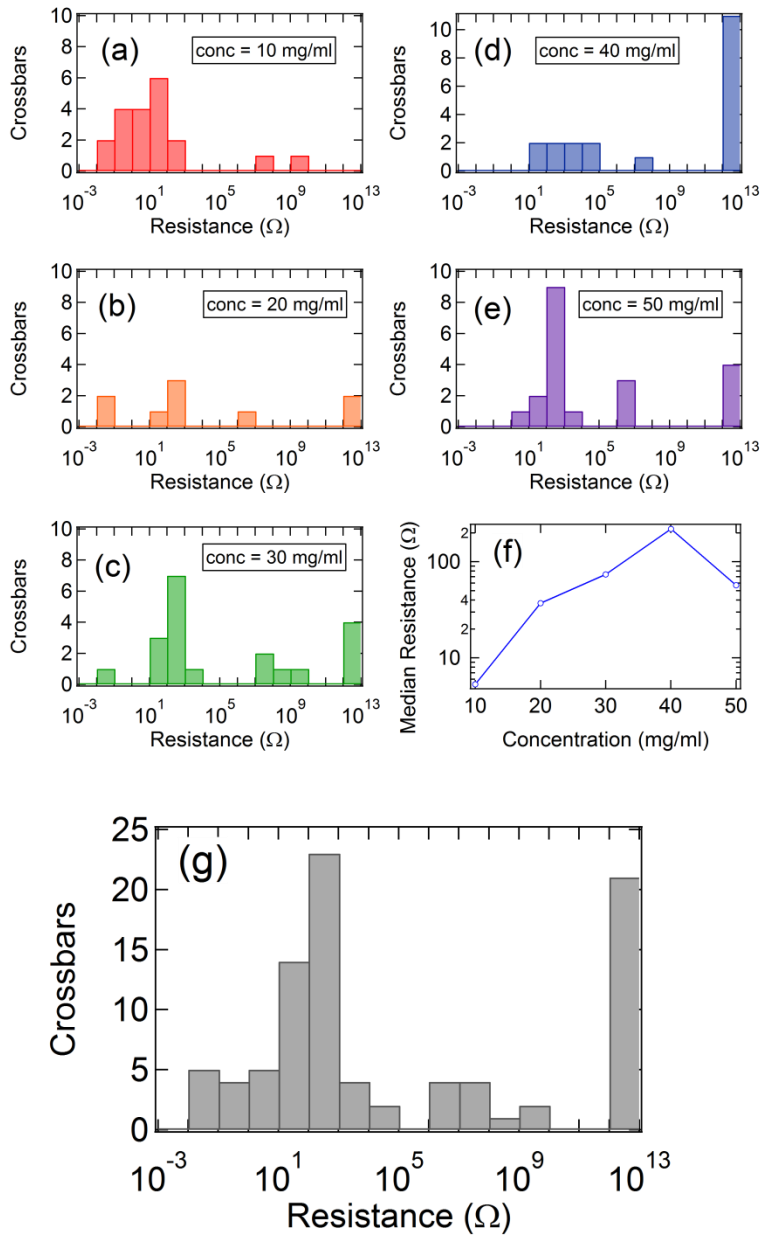

Fig. IV-4 Histograms showing variations in resistance values as a function of concentration of VT in dichloromethane. Although varying the concentration did allow for a slightly improved dispersion of the resistance values, the resistances still tended to bunch up in two regimes: open (> 1 TΩ) or low (< 100 Ω). (a-e) Individual histograms for 5 different concentrations. (f)

Semi-log plot of median resistance versus concentration (with open circuit values removed) (g) All resistance values.

Magnetoresistive Effects Observed in Co-VT-Py Junctions

Magnetoresistance Effects Observed

Over 200 samples, each comprising 5 individual crossbar devices, have been made. Of those approx. 1,000 devices, any that showed resistance values in a wide range between 50 ohms to 10 megaohms were selected to be wired for further measurement in the cryostat. Generally, the samples with the greatest number of promising devices on them were chosen. Once in the cryostat, another I-V measurement was done prior to running the magnetic field scan to probe for an MR effect as described above. Of samples selected for a magnetic field scan, approx. 1 out of 5 have shown some sort of magnetoresistance effect. Due to the amount of time required for the measurements, not all samples that showed promise could be measured. In many cases, when the distribution of the resistance values was not uniform, another batch of samples (usually 10-15 samples) was prepared in an effort to further optimize the spincoating parameters as described above.

Various types of magnetoresistance effects have been observed. They range from positive MR to negative, or "inverse" MR. Inverse MR has not only been observed in non-molecular spin valves having an inorganic oxide intermediate layer,[7] but also in molecular spin valves with Alq3 as the intermediate layer.[8] The wide range of possible MR types is a result of variations in the interfacial properties occurring between the molecule and the ferromagnetic metals. Because of sensitivity of the MR to the interface, it is possible to have both positive and

negative MR to occur in a system that was prepared the same way.[9] These scenarios were described briefly in Chapter 1.

The largest positive magnetoresistance thus far observed for the Co-VT-Py magnetic tunnel junctions is approx. 1% at 77K in a sample that had a resistance of 81 ohms. This sample (CC38) was made as a vertical stack structure on glass and was comprised of 5nmTi/40nmPy/VT/100nmCo/150nmAu. The MR for this sample is plotted versus field for temperatures of 290K and 77K as shown in Fig. IV-5.

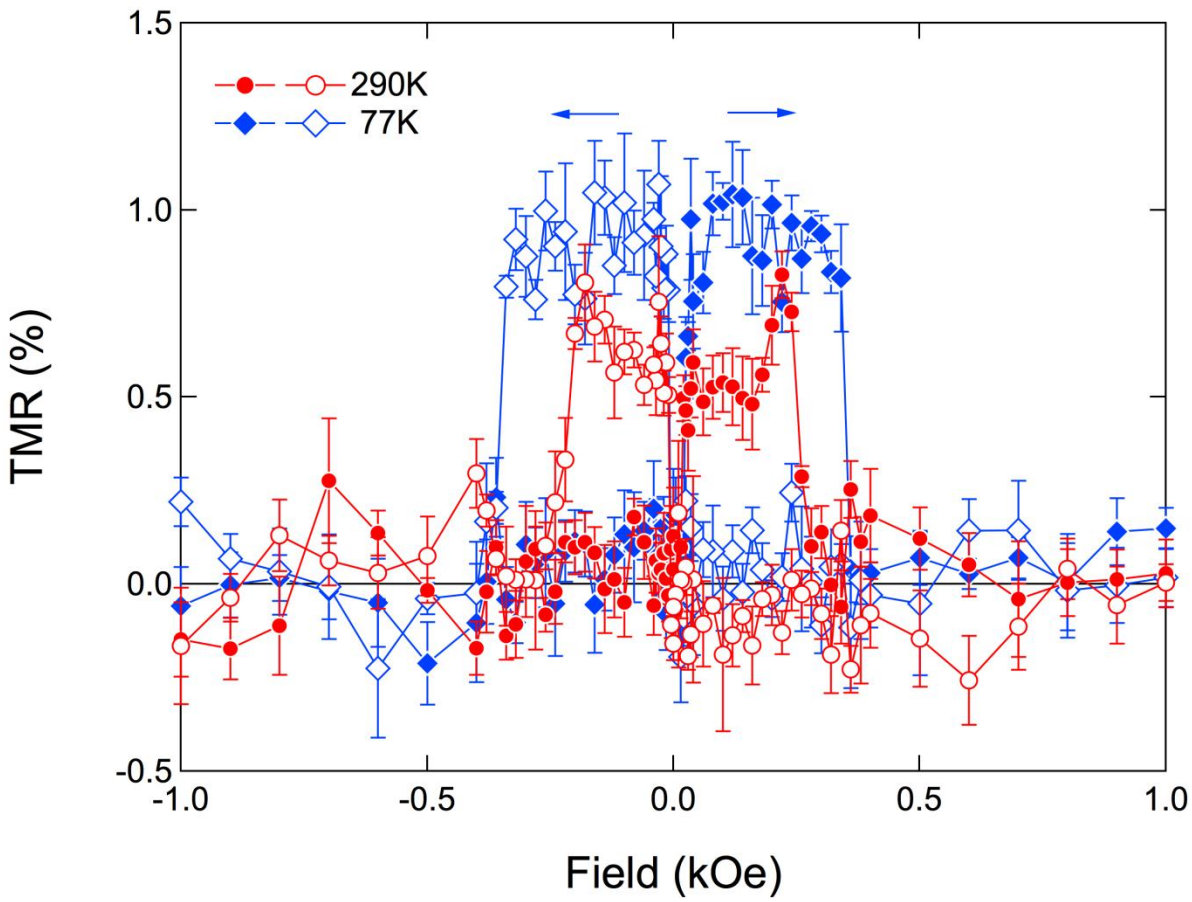

Fig. IV-5 Plot of TMR vs. magnetic field for sample CC38 at -10mV DC applied bias, which showed maximum MR of approx. 1% at 77K (blue). MR decreases at higher temperature 290K (red) to 0.8%.

The MOKE data for sample CC38 confirms that the switching fields are dominated by the bulk behavior of the ferromagnetic electrodes, as shown in Fig. IV-6. The low resistance of the junction is consistent with the observed distribution of resistances values from the devices shown in the histograms above (Fig. IV-4). Further discussion of the resistance and I-V behavior follows the investigation of the magnetoresistive effects below.

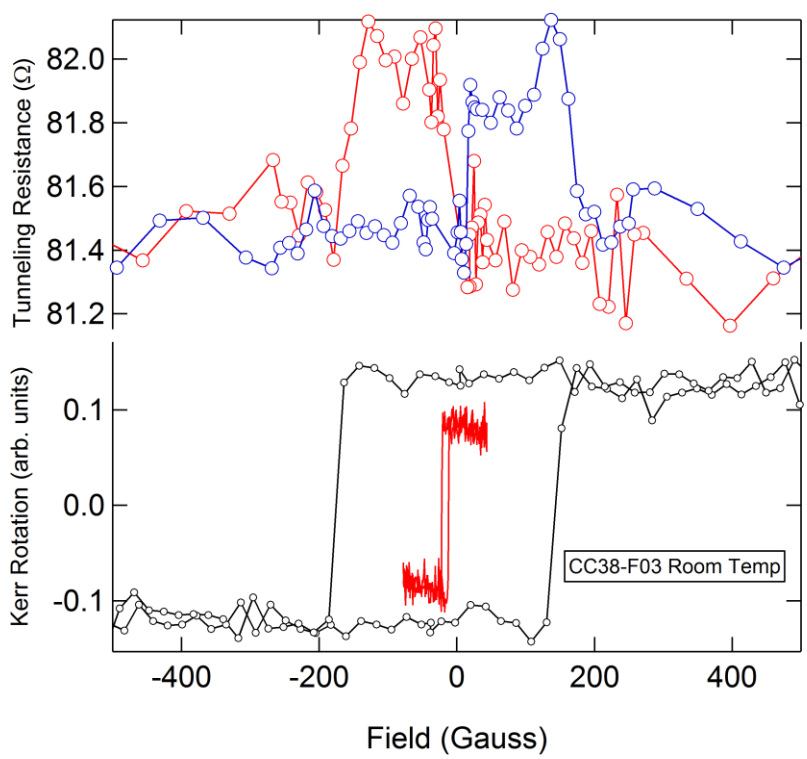

Fig. IV-6 Plot of resistance vs. field along with MOKE data for the individual ferromagnetic electrode layers (sample CC38). The field scan was done with the bias at -10mV. Resistance behavior matches the magnetization behavior of the electrodes. Permalloy switching (red, bottom graph) first at low magnetic field causes the anti-parallel window, followed by the cobalt switching (black) which returns the alignment to parallel.

Measurements performed on sample CC38 were limited to a low bias regime of ± 10mV as a result of the relatively high resistance of the back contact (approx.. 700 Ω). Consequently,

the bias dependence of the MR was not explored. Subsequent improvements were made to the sample design and circuit measurement components in order to allow for measurements at higher bias. Specifically, in later samples, a bottom Ti/Au layer at least 25nm thick was deposited underneath the permalloy to allow for greater conductance of the bottom contact. Also, a 1-to-1 current to voltage converter was installed in the measurement circuit to allow for measurements at higher currents than had been previously attainable using a $x10^4$ current amplifier (see Chapter 2 for description of the measurement circuit).

An example of inverse MR is shown in Fig. IV-7. The sample in this case again has a low resistance, and the overall MR increases as the field sweeps through zero. However, for the up sweep (increasingly positive magnetic field), the resistance drops considerably when the field becomes positive. There are also switching fields that cause a decrease in resistance before the magnetic field has reached zero (a so-called pre-effect), and an additional field change at approx. 1000 Oe. It is important to note that although the effect is most dramatic in the up sweep, the down sweep has a similar type of effect, but its magnitude is reduced. This is a type of asymmetric behavior of the MR seen in almost all of the samples. It will be discussed in greater detail below.

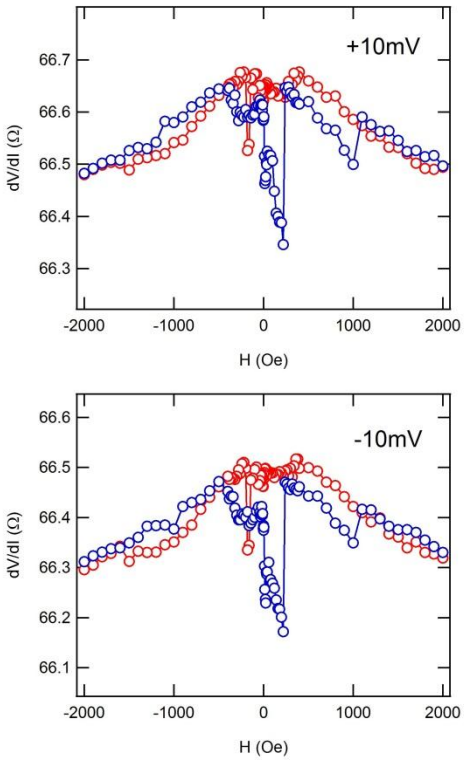

Fig. IV-7 Plots of differential resistance (dI/dV) showing an example of negative magnetoresistance observed in a MTJ (sample CC43) at 77K. This behavior resulted from a magnetic field scan while taking measurements following a sequence of 0V, +10mV, 0V, -10mV and 0V applied bias at each magnetic field point.

The sample behaviors described above, in spite of the wide variety of observed effects, are indeed very much of interest due to the fact that the structure with the VT interlayer can be used to make a spin valve. This is significant because it suggests the spins can survive in transit through the VT. The variety of the MR behavior indicates that there are certain configurations of the device structure which contribute to the MR in different ways (e.g. the interface). It is likely that, due to the spincoating process, the film is comprised of polycrystalline (nanocrystalline) layer, and effects may be resulting from individual crystals varying in size and orientation with respect to the current and/or field directions. The specific nature of these possible configurations remains to be explored.

IV.3. Valence Tautomeric Switching Behavior in a Spin Valve

A sample was found having a series of MR effects that, unlike for the previous samples discussed above, showed direct evidence of the tautomeric transition. The MR is positive and the resistance is also relatively low (approx. 13 ohms) as observed before for the samples showing MR effects. A detailed study was performed on this sample in order to determine the exact nature of the effects with the ultimate goal of elucidating the magnetotransport behavior of the tautomer molecule. The results of this study are presented in the next few sections.

Specific Magnetotransport Measurement Method

A measurement scheme was devised to explore for magnetoresistance effects in Co-VT-Py junctions. Measurements were performed using a Labview controller program and measurement circuit as described in Chapter 2. Specifically for these measurements, a magnetic field sweep was done by stepping the magnetic field from a maximum in one direction to a maximum in the opposite direction while taking individual electrical measurements at each step during the sweep. Subsequently, the field was swept back in the opposite direction to complete a full loop and thus probe for all possible magnetized conditions of the magnetic junctions.

A full magnetic field scan can take a significant amount of time to complete. Usually each set of measurements at a specific “point”, which corresponded to a single magnetic field point and a single bias point, took several seconds. Although the measurements themselves were taken within 300 to 500ms of each other, there was a built-in delay of approx.. 3 seconds after any change of bias output. This was done on purpose in order to allow time for the lock-in amplifier to properly read the differential signal. It would take a few seconds for the AC signal on the lock-in to stabilize after the instantaneous spike in frequency that was introduced by a step in the DC voltage output. By pausing, there would not be a false reading on the lock-in.

However, because of this time limitation, it was impractical to perform a full I-V measurement at each individual field step. As a result, a small number of I-V points were measured at each field step. A single I-V point, or if desired, a small number of multiple points, could be measured to comprise a “mini-IV” type measurement. As described in Chapter 2, a bias was applied to the crossbar circuit and the four-terminal current and voltage measured across the individual device, as well as differential current and voltage, were recorded.

In spite of the lower amount of time required by recording data at a smaller number of I-V points in the mini-IV, the time required was still significant enough that electrical drift in the circuit due to charging effects or other spurious effects on the meters could contribute to imprecise measurements. The drift can appear as an increase or decrease in the value read by the meter over time. In order to eliminate the effects of any drift, a measurement was performed (and current and voltage across the device recorded) with a zero voltage bias output applied to the sample circuit before and after the measurement at a given bias or small set of biases for the mini-I-V. In this way, the zero bias reading could be used as a baseline and the

difference between the baseline value and the measured value taken as the value for subsequent data analysis. For example, one measurement sequence of applied biases was: 0V, +10mV, 0V, -10mV, 0V. When determining the value of the current at +10mV bias for example, the value of the current from the two adjacent zero bias values (immediately before and immediately after) was averaged and then subtracted from the actual measured value at +10mV. A measurement for the voltage was done in the same way, and a resistance value at +10mV could then be calculated as follows, for example:

$$R_{+10mV} = \frac{\Delta V}{\Delta I} = \frac{V_{+10mV} - \left(\frac{V_{0\ (before)} + V_{0\ (after)}}{2}\right)}{I_{+10mV} - \left(\frac{I_{0\ (before)} + I_{0\ (after)}}{2}\right)}$$

Eqn. (1)

The terms in the last equality are the respective actual measurements taken from the instruments. The above value is sometimes referred to as a DC value.

Likewise, measurements from the lock-in amplifiers were taken using the circuit diagram shown in Chapter 2, Fig. II-4. A differential resistance value was calculated each time from the individual respective measurements without any averaging:

$$R_{d\ +10mV} = \frac{dV}{dI} = \frac{dV_{+10mV}}{dI_{+10mV}}$$

Eqn. (2)

The above value is sometimes referred to as an AC measurement value.

Magnetotransport Measurements on Valence Tautomeric Spin Valve (CC149)

Magnetotransport measurements were performed on CC149 in the manner described above. To examine the temperature-dependent behavior in order to explore for the tautomer transition, measurements were taken in a total of eight cooling runs. Full magnetic field scans were done at selected temperatures with I-V data collected for a set of biases at each field step. Usually the bias steps included both positive and negative bias to comprise a mini-I-V type measurement. Fig. IV-8 shows results from a field scan at 200K, representing a high temperature measurement, corresponding to the high-spin VT form, and Figs. IV-9, IV-10, and IV11 show the results from three separate field scans at 80K, representing a low temperature measurement, corresponding to the low-spin VT form. In these measurements, the bias was toggled at two separate bias values, for both positive and negative. For example, with bias values of 30mV and 40mV, the sequence for the mini-I-V was: 0V, +30mV, +40mV, 0V, -30mV, -40mV, 0V. Current and voltage were recorded and these values were used to calculate the DC resistance (in ohms), using the two nearest zero bias measurements in the sequence, as indicated in eqn. (1). Differential current (dI) and differential voltage (dV) were recorded and used to calculate the differential resistance R_d (= dV/dI as indicated in eqn (2)), which is plotted in the right column of the figures. Unlike the DC, the differential measurement makes it possible to calculate an AC resistance value when the DC bias output value was 0V. Those additional measurements appear as the scans in the differential resistance (AC) column with no corresponding values in the DC column.

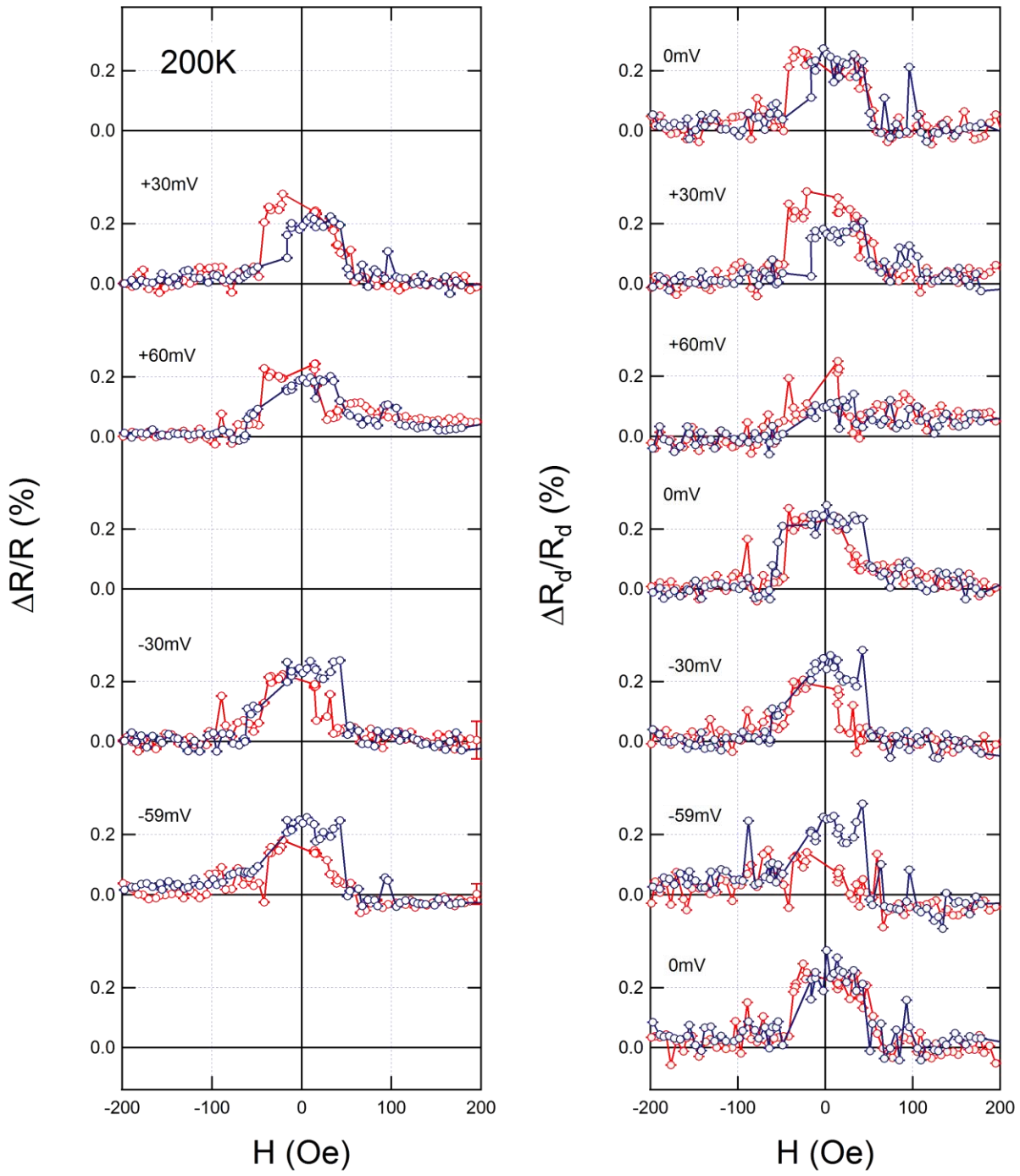

Fig. IV-8 Magnetotransport scan at 200K. The tautomer is in its high-spin form (S=5/2) at this temperature. Plots show the measurements corresponding to the sequence in which the data was actually collected. At each field step, the sequence for the mini-I-V was 0V, +30mV, +60mV, 0V, -30mV, -60mV, 0V.

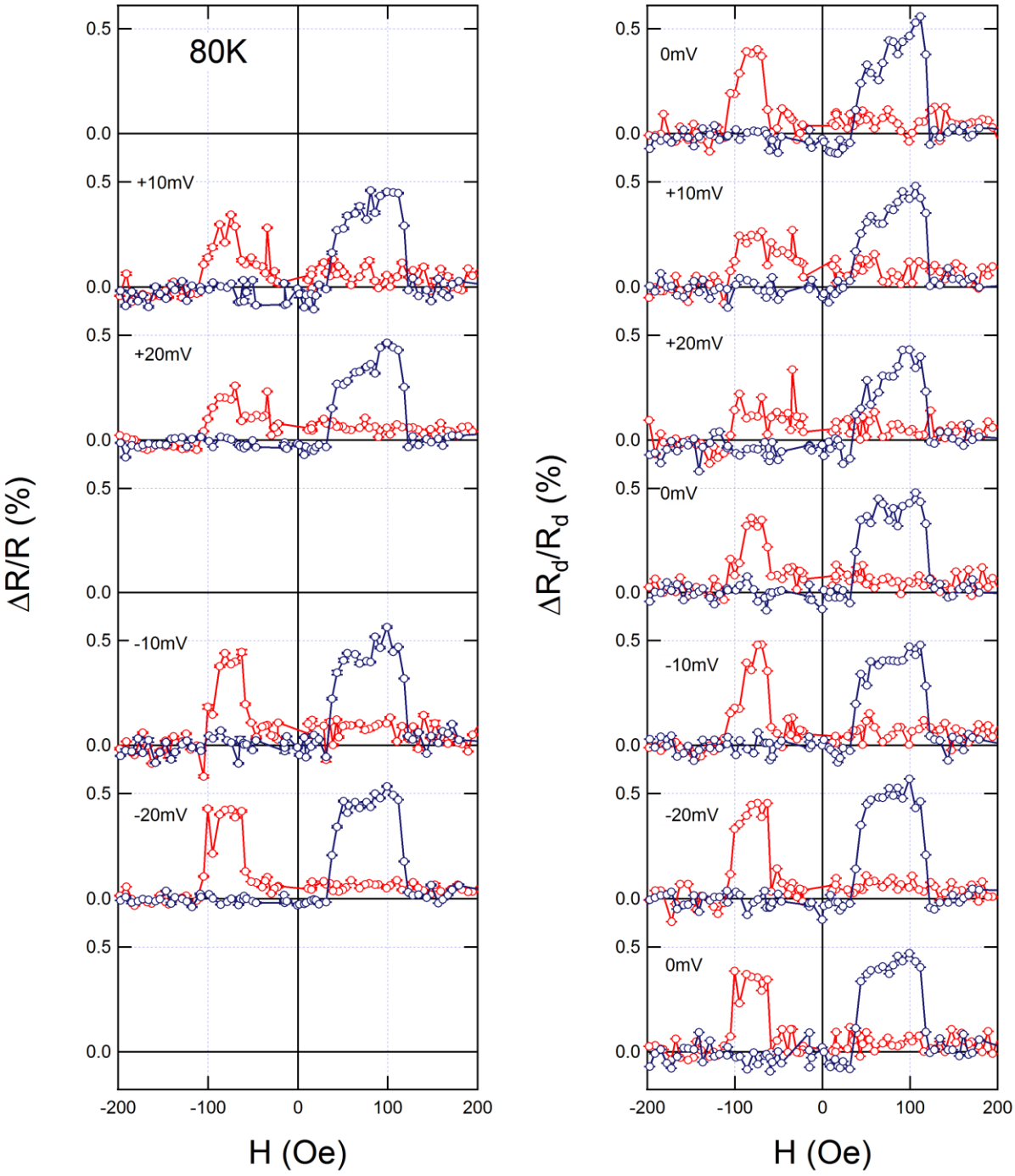

Fig. IV-9 Magnetotransport scan at 80K. The tautomer is in its low-spin form (S=1/2) at this temperature. Plots show the measurements corresponding to the sequence in which the data was actually collected. At each field step, the sequence for the mini-I-V was 0V, +10mV, +20mV, 0V, -10mV, -20mV, 0V.

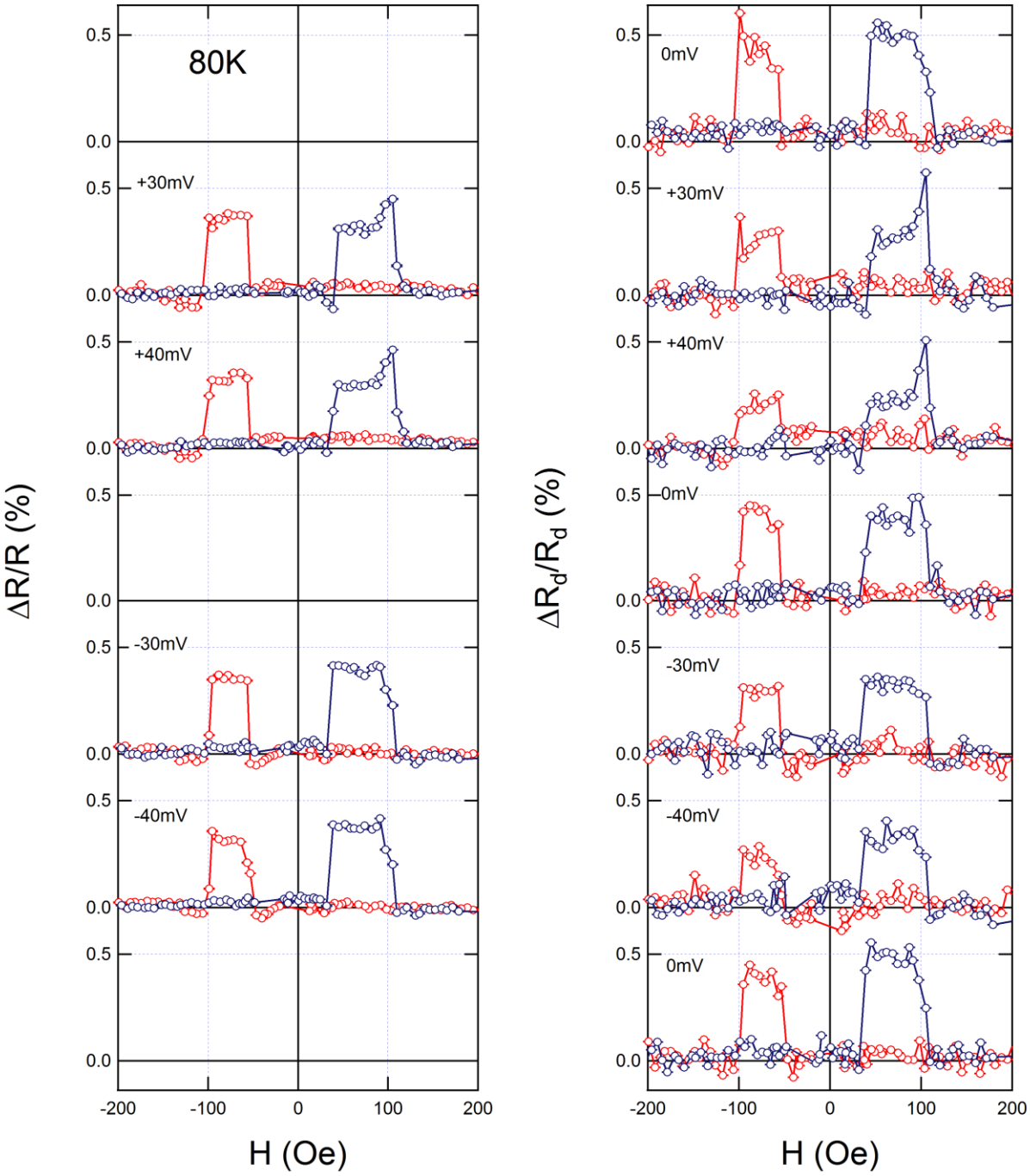

Fig. IV-10 Magnetotransport scan at 80K. The tautomer is in its low-spin form (S=1/2) at this temperature. Plots show the measurements corresponding to the sequence in which the data was actually collected. At each field step, the sequence for the mini-I-V was 0V, +30mV, +40mV, 0V, -30mV, -40mV, 0V.

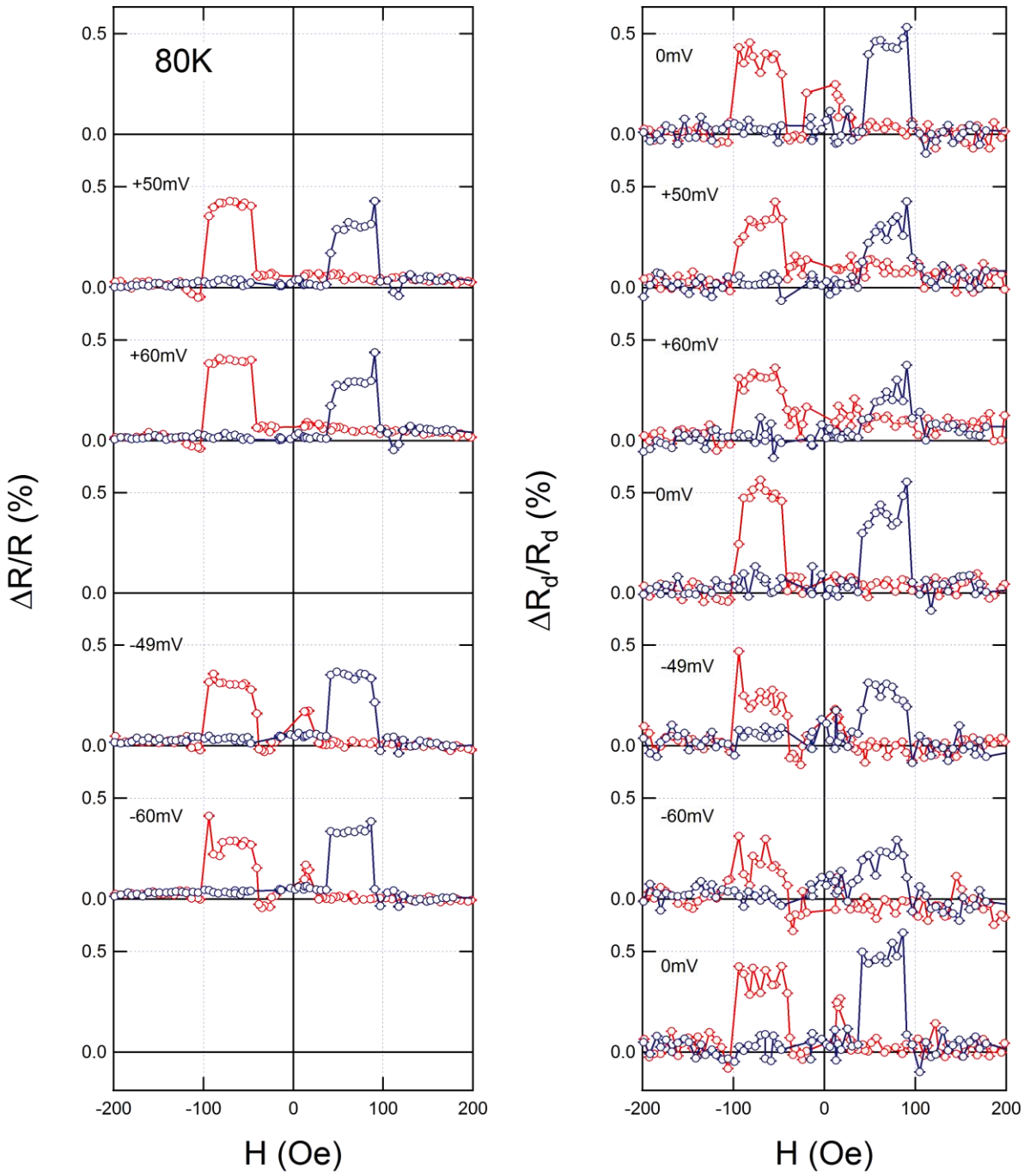

Fig. IV-11 Magnetotransport scan at 80K. The tautomer is in its low-spin form (S=1/2) at this temperature. Plots show the measurements corresponding to the sequence in which the data was actually collected. At each field step, the sequence for the mini-I-V was 0V, +50mV, +60mV, 0V, -50mV, -60mV, 0V.

I-V Behavior

As mentioned above, the device exhibited low resistance (approx. 13 Ω at room temperature). It is important to mention, however, that for the initial observation of the MR effect at room temperature, the device had a resistance of approx. 270 Ω with the same MR behavior. During repeated measurements, which included cycling of biases as well as cycling of the temperature during low-temperature measurements, the resistance fell to lower and lower values, eventually reaching a range from 13 Ω to 10 Ω by the end of a total of 9 cool-downs. The cause of these transitions is still not clear. It is possible that metallic filaments of the top cobalt layer are migrating with the application of applied bias. As the VT itself is known to transition with an increase in bond length, this may be a contributing factor to the reorganization of the polycrystalline VT layer allowing metal to migrate when higher biases are applied. The creation of metallic filaments would lead to the formation of pinholes and hot-spots through and on the amorphous VT layer. Hot spots by themselves are expected due to known non-uniformity of the polycrystalline film, as observed by profilometry. The thickness of the film was observed to vary from as little as 10nm to as much as 70nm in different places across the film. In fact, in some of the samples, the film would even have localized areas of no coverage, leading directly to shorted crossbars. So the decrease in resistance may be due to an increasing number of hot spots. This will be discussed in greater detail below.

The I-V curves for all measurements (before and after any resistance transitions) were non-linear and had a decreasing slope, leveling off at higher magnitudes of the bias. The differential conductance shows this behavior very clearly by its concave-down shape (see Fig. IV-12).

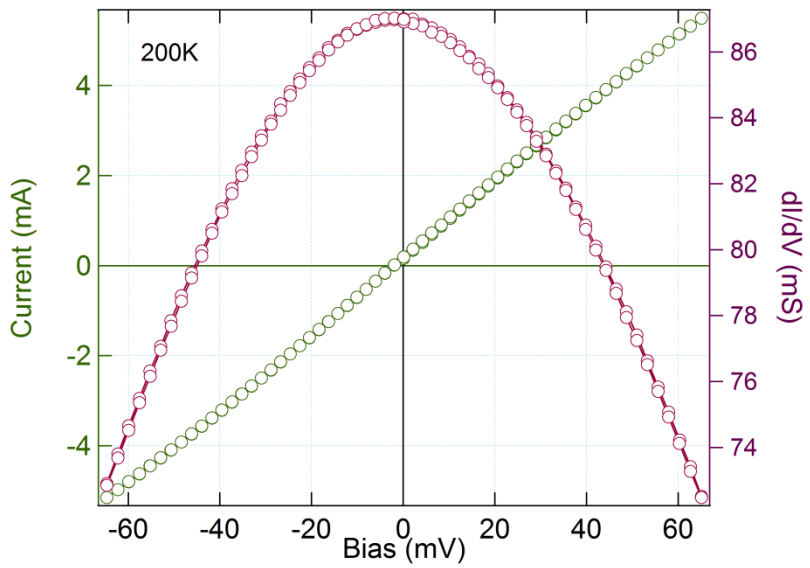

Fig. IV-12 I-V curve (green) and differential conductance (purple) for sample CC149 at 200K. The I-V shows non-linearity of decreasing slope at increasing bias. R_0 for this device is approx. 13 Ω.

A detailed plot of the evolution of the resistance throughout the thermal cycling of the nine individual cool downs is shown in Fig. IV-13. Metallic temperature dependence was observed, most notably in the plot for cooling run #4, where the sample was cooled to 4K with liquid helium.

This metallic temperature dependence indicates a pinhole may be present in the film. The I-V and differential conductance supports this conclusion. This behavior has been reported in prior studies.[10] Based on the conclusions of these prior studies, when the current increases as higher and higher bias is applied, heating occurs in the narrow constriction of the pinhole. This in turn would cause increased resistance at higher bias due to thermal scattering of electrons, leading to the decrease in the differential conductance plot at high bias. The concave-down shape of the differential conductance is not a sole determinant of a pinhole,

however. Detailed analysis and theoretical models of pinhole behavior have even shown that pinholes may still be present in tunnel junctions regardless of whether the profile of the differential conductance is concave-down or concave-up.[11] The only criterion for concluding a pinhole is not present is to have increasing (non-metallic) resistance versus decreasing temperature.[10]

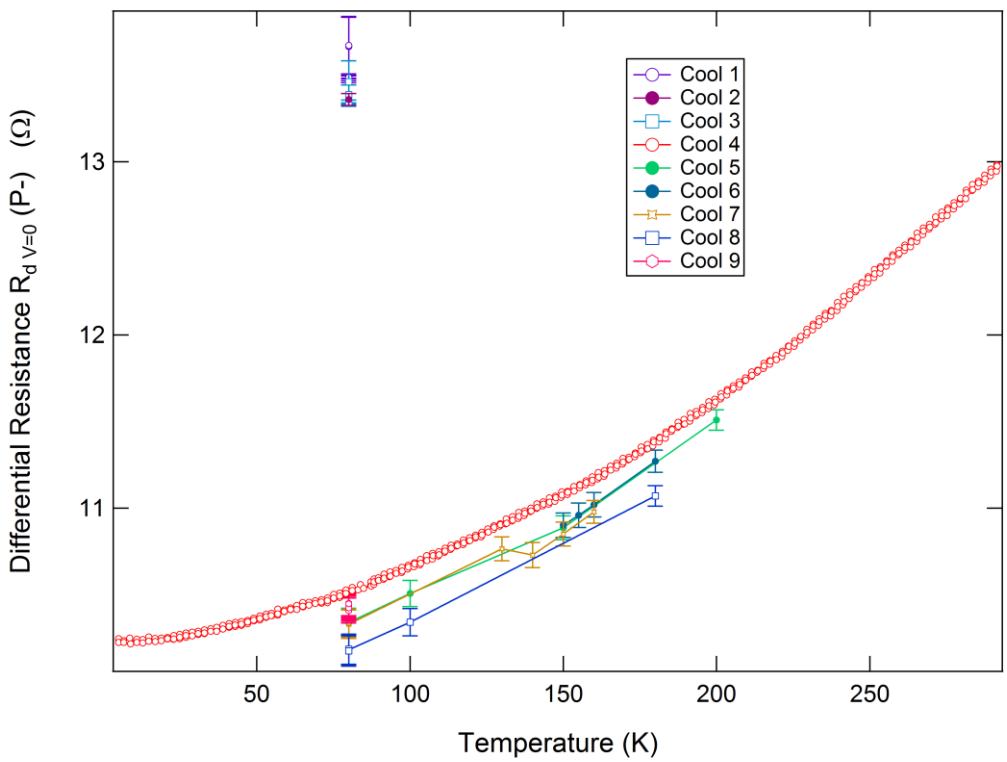

Fig. IV-13 Temperature dependence of differential resistance for sample CC149. Resistance decreases with decreasing temperature, indicating metallic behavior, as shown in cool 4 (red circles). In this cooling run, the sample was cooled down to liquid helium temperature (4K) and data was collected to obtain a continuous curve upon returning to room temperature. Overall resistance was also observed to decrease from one cool-down to the next. During any individual run, the shape of the cooling curve appears to be the same. Earlier cooling runs (Cools 1 to 3) were done simply by cooling down to 80K (one temperature point) and then returning to room temperature. Cools 5 through 9 were done to explore for the tautomeric transition and also for the light experiment.

On the other hand, having metallic temperature dependence does not necessarily guarantee a pinhole is present either. There are also other possible modes of transport that could account for this behavior, such as a induced dipoles at the metal-molecule interface[12] or rectification by charging in the molecular orbitals.[13] Additionally, as has been demonstrated in the literature,[11] it is possible to have tunneling behavior through other regions even when pinholes dominate the transport in parallel.

A comparison was made between the I-V behaviors during the different cooling runs using differential resistance measurements. The resistance values at all biases was divided by the baseline differential resistance value at zero bias for some individual temperatures during the run. These curves are plotted together in Fig. IV-14. As can be observed in the plot, there is a clear temperature dependence to the change in curvature, which is what would be expected if the pinhole in parallel with the tunneling transport through the film is becoming more conducting. However, measurements at low temperature (e.g. at 80K) show approximately equal curvature shape for almost all of the cooling runs. This indicates that although there may be additional conduction channels in the later cooling runs, these conduction channels are actually all of the same type (e.g. hot spots) and go through the film. In other words, it is the resistance through the film that is dropping between runs and the pinhole is staying the same. If the pinhole were to increase in size, enough to account for the drop in resistance, it would significantly change the curvature of the differential resistance.[11] This did not happen. A simple parallel resistor analysis used to to model the effects of any possible parallel paths, bears this out. According to the following equation for parallel resistor paths:

$$\frac{1}{R_T} = \frac{1}{R_C} + \frac{1}{R_P} \qquad (1)$$

with R_T = total resistance, R_C = the resistance of an earlier cooling run having high resistance, and R_P = the resistance of the parallel conduction path that lowered the total resistance in a later cooling run, it is not possible for the parallel conduction path to be have a linear I-V behavior (i.e. be a simple ohmic resistor) without shifting the curvature on the differential resistance plot as shown in Fig. IV-14. Since the curves overlap for a given temperature in all cooling runs, it is concluded that although the resistance is lower for the later runs, the conduction channels are all of the same type with the same I-V behavior. With this in mind, a comparison between the MR effects of the different cooling runs, including a comparison between the behaviors at different temperatures, is justified.

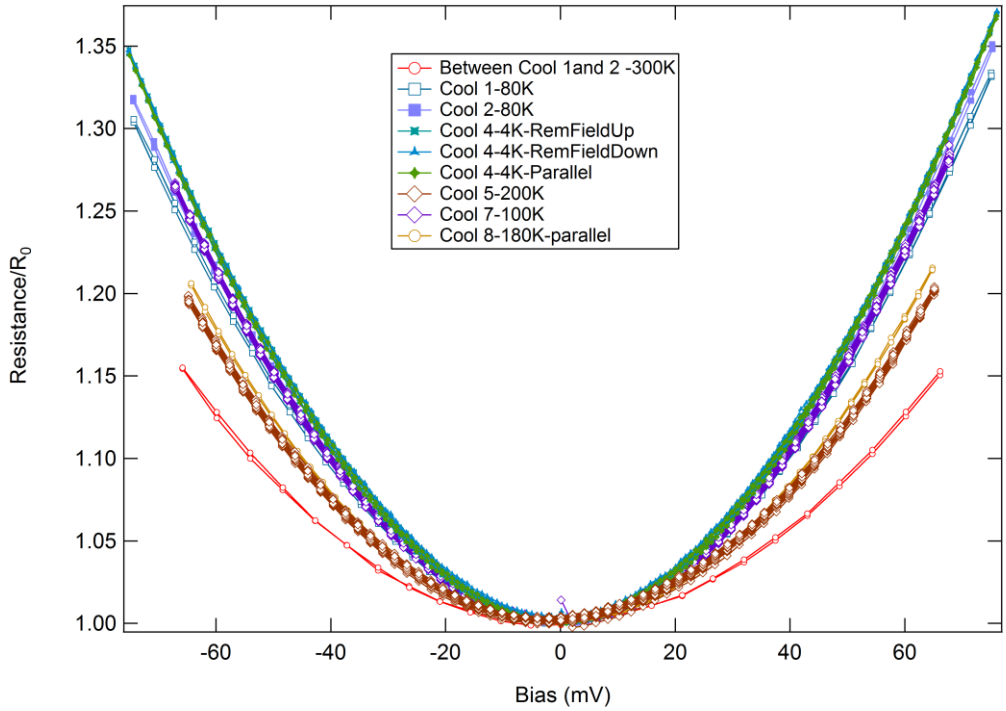

Fig. IV-14 Comparison of the scaled differential resistance vs bias for separate cooling runs. The actual differential resistance is divided by the baseline differential resistance at zero bias voltage to examine if there is any scaling.

Further studies will be necessary to elucidate the exact nature of the interfaces and contacts that are giving rise to the I-V behavior. In this study on this particular sample (CC149), however, the focus is on the spin-dependent transport. It is possible to reach many conclusions about some interesting spin-dependent behaviors that are caused by the known magnetic behavior of the valence tautomer molecule.

Discussion of I-V Behavior in Prior Sample showing 1% MR

At this point, it is important to compare the I-V behavior of CC149 to that of CC38, which was the sample reported at the beginning of the chapter exhibiting 1% MR. The low resistance in sample CC38 is likewise an indicator of the possibility that a metallic short, or pinhole, is occurring. However, it is unlikely that transport is occurring through a pinhole in this sample for a couple of reasons. First, the I-V data shows a positive concave-up differential conductance with the current increasing, which is the shape expected due to quantum tunneling. A pinhole is expected to have differential conductance with a concave-down shape (i.e. conductance decreases with increased bias due to thermal heating),[11] although it is important to note that prior studies have determined that a concave-up shape in the differential conductance could also occur with a pinhole present.[11] Secondly, the resistance vs. temperature data shows an increase in resistance for decreasing temperature. This suggests non-metallic, semiconducting behavior. The latter resistance vs. temperature behavior is a sufficient criterion to rule out a pinhole.[10] Hence, the transport mechanism is either hopping or tunneling through the VT layer for this sample showing large MR effects. This suggests that the

MR in sample CC149, which shows VT transition effects, is also a result of conduction through the VT. It is likely that the low resistance and metallic behavior in CC149 is a result of parallel conduction through the VT and through a pinhole at another location on the sample.

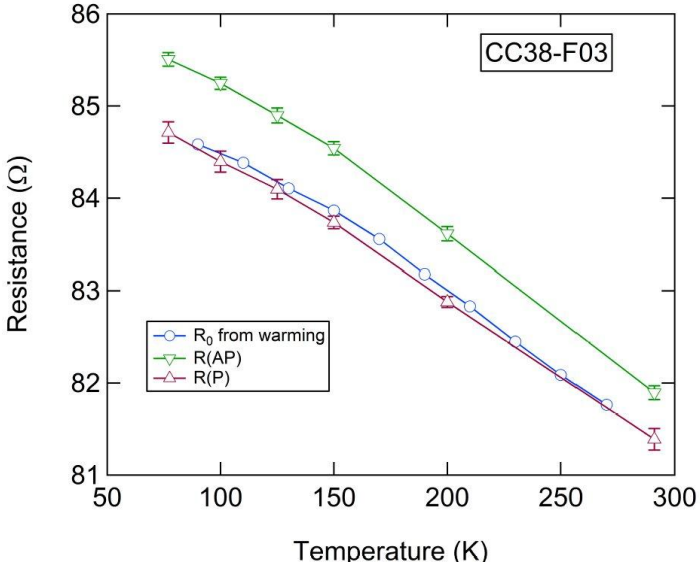

Fig. IV-15 Plot of resistance vs. temperature, including resistance for the parallel and anti-parallel magnetizations for sample CC38. Resistance increases for decreasing temperature. This indicates that transport is not dominated by a pinhole.

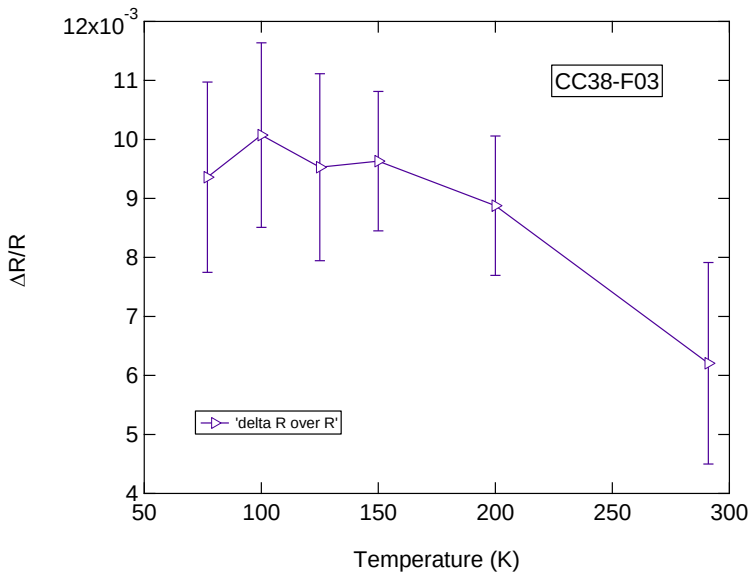

Fig. IV-16 Plot of MR vs. temperature for sample CC38. MR increases as temperature decreases.

IV.4. Results and Discussion of Valence Tautomeric Switching

The magnetic behavior of the high-spin and low-spin forms of valence tautomers under investigation has been measured on the SQUID by collaborators in the Shultz group at NC State Chemistry.[1] As shown in Fig. IV-17, the susceptibility undergoes a change from the high-spin, high temperature form to the low-spin, low temperature form. When the samples are polycrystalline, the conversion between populations of low-spin and high-spin occurs gradually. The samples examined in this study are of the polycrystalline variety.

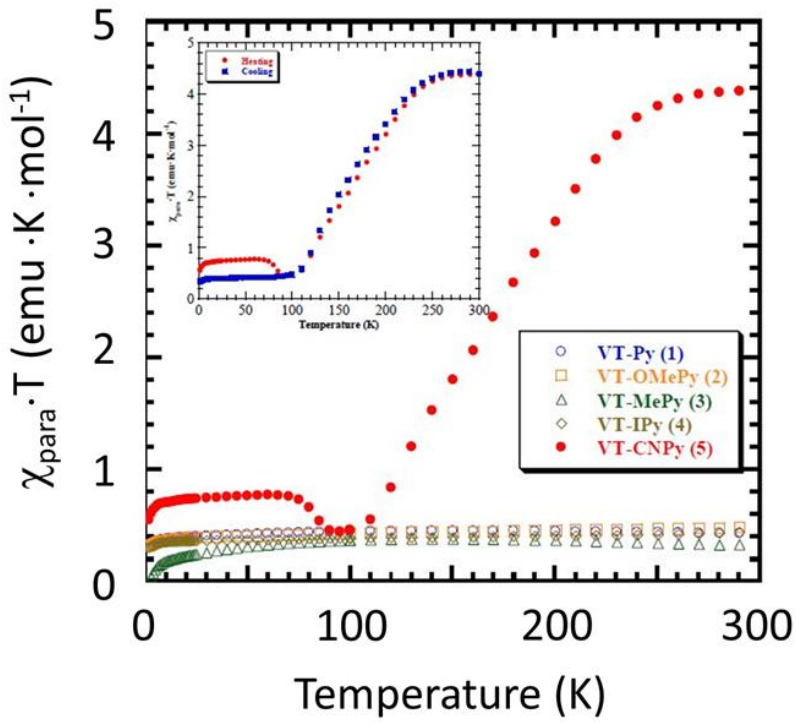

Fig. IV-17 Change in magnetic susceptibility times temperature plotted versus temperature for a variety of valence tautomeric crystals. Each molecule type has a pair of curves showing hysteresis due to heating and cooling. A polycrystalline sample undergoes a gently sloping transition. This occurs as a result of the inhomogeneity of the population conversion for the polycrystalline sample. Plot taken from ref. 1.

There are many significant behaviors that can be observed from the data in the four magnetotransport scans shown in Figs. IV-8 to IV-11, as well as the approximately 50 total scans that were measured at different temperatures and bias conditions for the sample during the nine different cooling runs. As it is impractical to display all of the results here, these main behaviors are classified and summarized in relevant graphs and in the discussions which follow.

First, it is observed that there is a clear difference between a high temperature behavior as shown in Fig. IV-8 and low temperature behavior as shown in Figs. IV-9 to 11. The most obvious change is that, at high temperature, the switching fields are coinciding with each other

so that the higher resistance regions are overlapping each other both when the field is sweeping down and when the field sweeping is up, whereas at low temperature, the high resistance regions are separated from each other with a gap in between them. At high temperature, the high-resistance region begins during the magnetic field sweep prior to the magnetic field changing polarity, i.e. prior to reaching zero. The resistance becomes low again for the opposite polarity at approximately the same field strength, i.e. the switching is symmetric about zero. At low temperature, there are two separate high-resistance regions spaced apart from each other and away from zero, as expected for the two anti-alignment configurations resulting from hysteresis loops of two different ferromagnetic electrodes as described in Chapter 1. This shifting of the coercive fields for the two different temperatures is a result of the two different tautomeric forms. This is analyzed in greater detail in the analysis section below. The tautomeric transition occurs at approximately 150K-180K for the polycrystalline sample, so converting from the high spin form to the low spin form happens when cooling down from room temperature to 80K.

A second significant behavior observed in Figs. IV-8 to IV-11 is that there is a bias dependence shown in the size and shape of the MR peaks on the down sweep versus the up sweep of the magnetic field. The plots in Fig. IV-18 have been compiled to make this behavior easier to see along with the temperature dependence. In the magnetic field scan at a positive bias (+60mV in the figure), the plateau of the MR value on the down sweep is greater than the plateau for the MR on the up sweep. In the magnetic field scan at a negative bias (-60mV), the MR for the down sweep is less than the MR for the up sweep. This effect, sometimes more difficult to observe due to the presence of isolated spikes which themselves may be significant

other features discussed in greater below, is prevalent at both temperatures and throughout the magnetotransport scans. It is considered to be a so-called “spin rectification” effect. It is discussed in greater detail below.

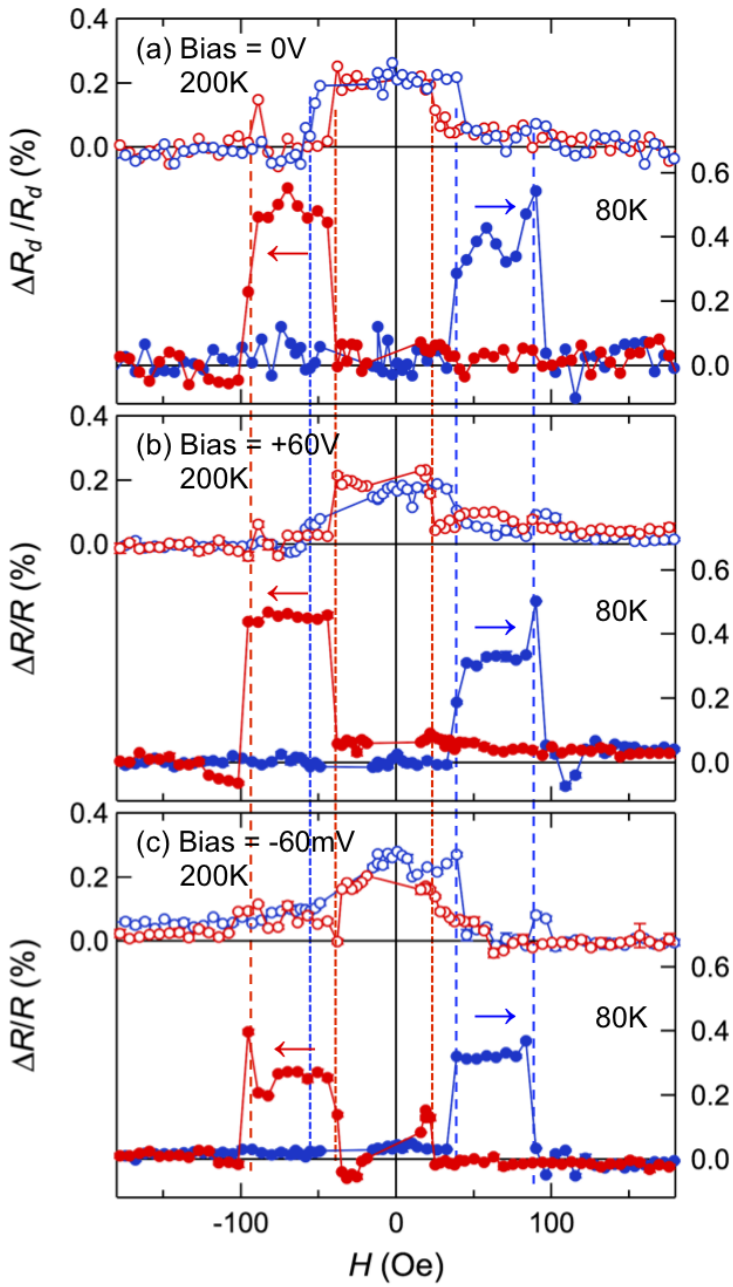

Fig. IV-18. Comparison of the magnetic switching fields observed at temperatures of 200K and 80K - on either side of the valence tautomeric transition (150K). For (a), the differential resistance R_d is plotted at bias = 0V, while for (b) and (c), the DC resistance is plotted at +60mV and -60mV, respectively. At 200K, switching occurs as the field is decreased from maximum but before the magnetic field has reached zero. The return switch occurs at approximately the same field magnitude of the opposite polarity during the sweep. At 80K, the switch occurs once the magnetic field has changed polarity and the magnitude has increased. The MR corresponds to a more conventional switching "window" in which the two bulk ferromagnetic electrodes are expected to be anti-parallel.

A third significant behavior observed in Figs. IV-8 to IV-11 is that the MR increases for the lower temperature. This is the generally expected behavior for a spin-valve and is a result of increased stabilization of the system resulting from reduced thermal vibrations. It has been observed in all of the tautomeric samples, including sample CC38 as shown in Fig. IV-5 above.

A fourth behavior can be observed when plots are reconstructed as shown in Fig. IV-19. Here again the two different temperatures are plotted for a collection of four points. However, included in this collection are measurements for the differential bias output of 0V which immediately follow a positive or negative higher bias measurement (see Figs. IV-8 to IV-11) in the “mini I-V” toggling sequence. It is clear based on the features present that a time-based “memory” behavior is present. In other words, the immediately preceding higher bias has an effect of setting a state that persists during the subsequent zero bias measurement.

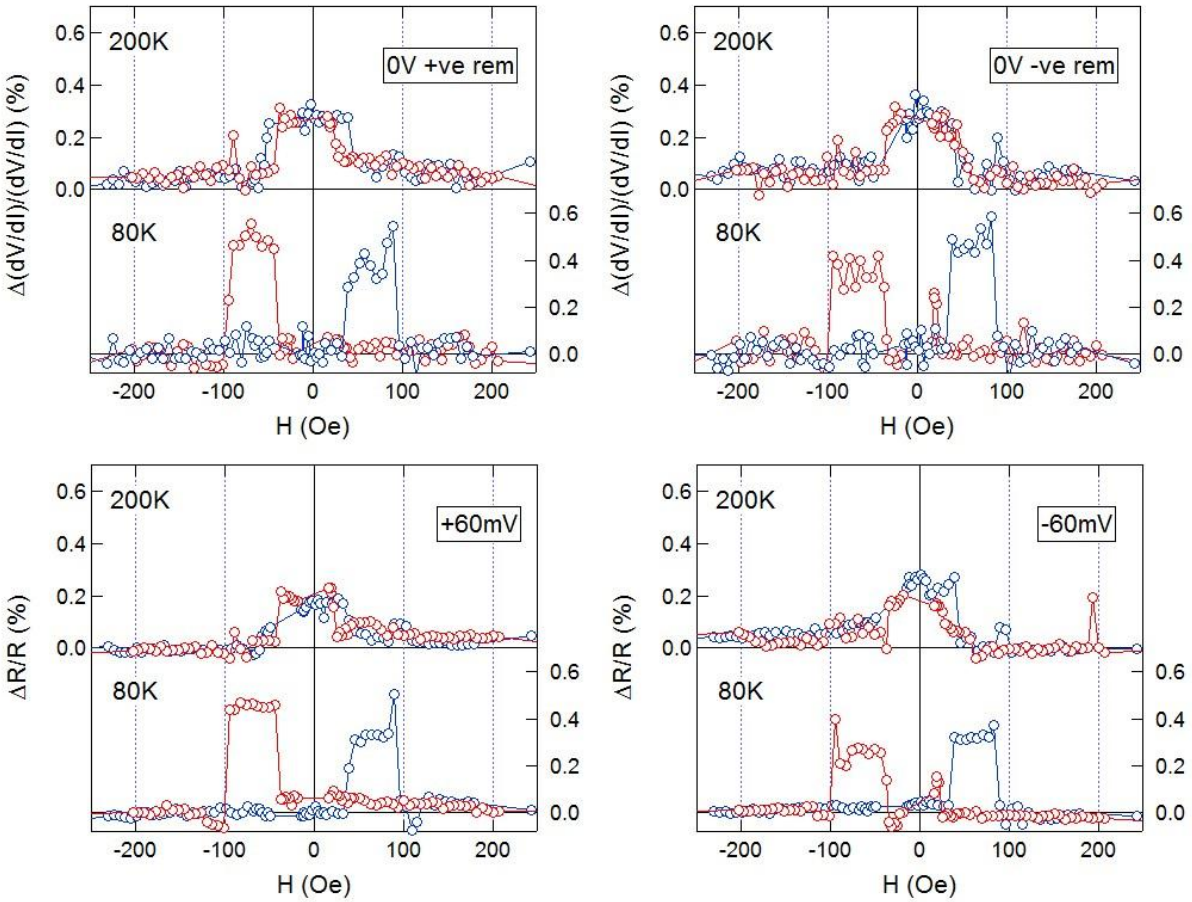

Fig. IV-19. Another comparison (like Fig. IV-18) of the magnetic switching fields observed at temperatures of 200K and 80K - on either side of the valence tautomeric transition (150K). Here, however, positive and negative remanent values are plotted for the AC differential resistance at 0V. These plots show the effects at the different higher biases carry over to the 0V measurements. The effects can be seen as features such as spikes or rectification behavior, indicating a time-based "memory" is present.

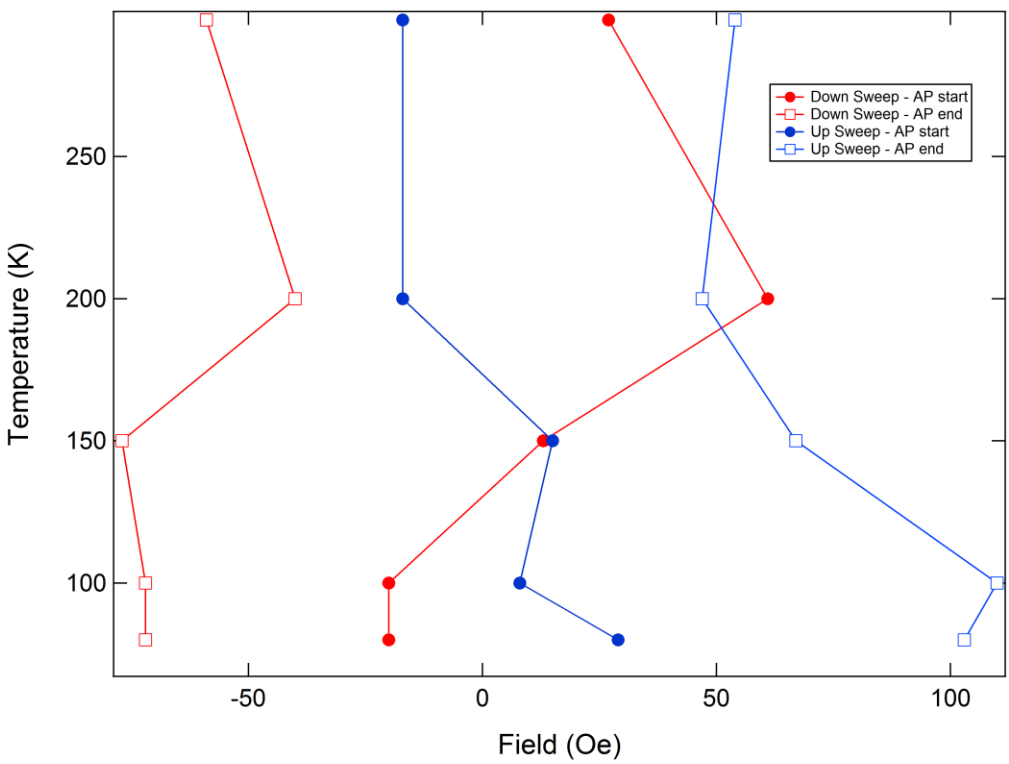

Fig. IV-20. Temperature-dependent shifts of the switching fields. Red points indicate the switching fields of the down sweep, and blue points represent the switching fields of the up sweep.

With regards to the shifting of the switching fields, it is also noted that the fields appear to shift in a continuous manner during cooling so that there is a gradual movement during the transition. This can be seen schematically in Fig. IV-20 for a cooling run which went through the transition. Here the four switching points for the main anti-parallel alignment windows of the MR runs are plotted. As the temperature decreases, the windows for the down sweep and the up sweep move apart from each other and away from zero.

Spin Rectification

As mentioned above, there is an effect of spin rectification in the MR value which occurs as a result of the bias direction of the measurement. It can be seen in Fig. IV-18, where for the positive bias (+60 mV in this case), the downward field sweep has a higher MR than the upward field sweep. When the bias direction is reversed (to -60mV in Fig. IV-18), the MR is higher for the upward field sweep and lower for the downward field sweep. This behavior is observed throughout the measurements (at both temperatures). It is summarized in the following logic table:

Rectifying Logic Table

		Field Sweep	
		↓	↑
Bias	+	H	L
	−	L	H

Table IV.1. Rectifying Logic Table. This table describes the behavior of the MR depending on the bias direction and the field sweep direction. H indicates high MR, and L indicates low MR. The behavior can be seen in Fig. IV-18.

IV.5. Parallel Resistors Model

To investigate the behavior of a spin valve with a magnetic middle layer, a model has been constructed based on parallel resistors. This model can be used to explain the

consequences a spin-polarized middle layer has on the magnetoresistance in particular with respect to the spin rectification effect.

As discussed in Chapter 1 in the density of states model for a ferromagnetic metal, the states of the metal's electrons can be classified into the two separate spin types of spin-up and spin-down. A spin-valve exploits the different spin density of states of the two separate metal electrodes depending on whether the magnetizations of the metals are parallel or anti-parallel. When they are parallel, electrons of either spin-up or spin-down can pass through the interlayer into an equally matched number of available states on the opposite electrode. However, when the magnetizations of the two electrodes are anti-parallel, there are not enough available states for all of the majority spin-up electrons to go into the opposite electrode, nor are there as many minority spin-down electrons coming into the opposite electrode as there are states available (see Fig. I-1, Chapter 1).

Another way to conceptualize the behavior of the electrodes was developed by Mott as a model for giant magnetoresistance. Essentially the flow of spin-up and spin-down electrons can be thought of independently as two parallel channels of current. Instead of using the density of states to model the behavior, resistors can be used to represent the relative availability of states for spin-up or spin-down. A single ferromagnetic electrode can then be modeled as two resistors, $r_{\uparrow}$ and $r_{\downarrow}$ corresponding to its density of states:

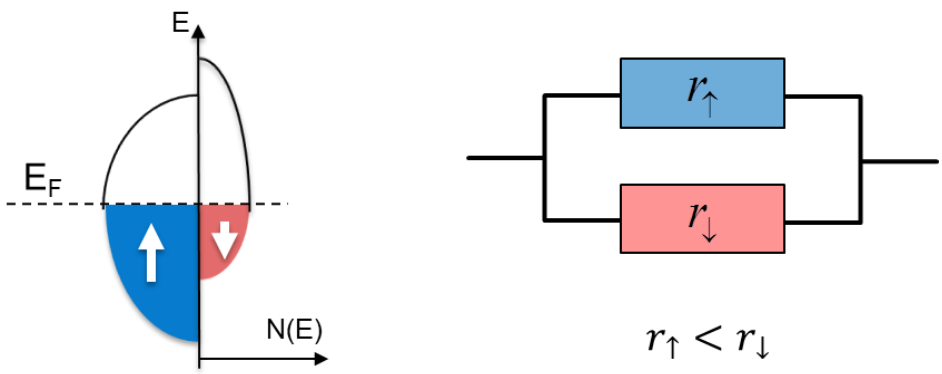

Fig. IV-21. Density of states (left) and corresponding Mott parallel resistor (right) for a ferromagnetic electrode.

In the example shown in Fig. IV-21, the blue spin-up states correspond to the spin-up channel going through $r_\uparrow$ which, because it has more available electrons and thus a higher current, can be represented by a lower resistance, and the red spin-down states can be represented by resistor $r_\downarrow$ which has a higher resistance because of the fewer electrons. It is important to note at this point and going forward in the discussion that, although electrons are mentioned as the charge carrier, the conduction could occur through holes instead of electrons, or a combination of the two. For simplicity of this discussion, the charge carrier has been chosen to be electrons.

The model can be extended further to the case of conduction through two ferromagnetic metals. This is the case for a giant magnetoresistance (GMR) device. In that device the current actually flows in the plane of the two layers with a spacer in between, unlike a more conventional spin-valve where the flow usually occurs by electron tunneling. The two ferromagnetic metals are modeled in series and the spin channels can be represented as two

separate parallel channels of series resistors as follows, for both possible spin configurations of parallel and anti-parallel.

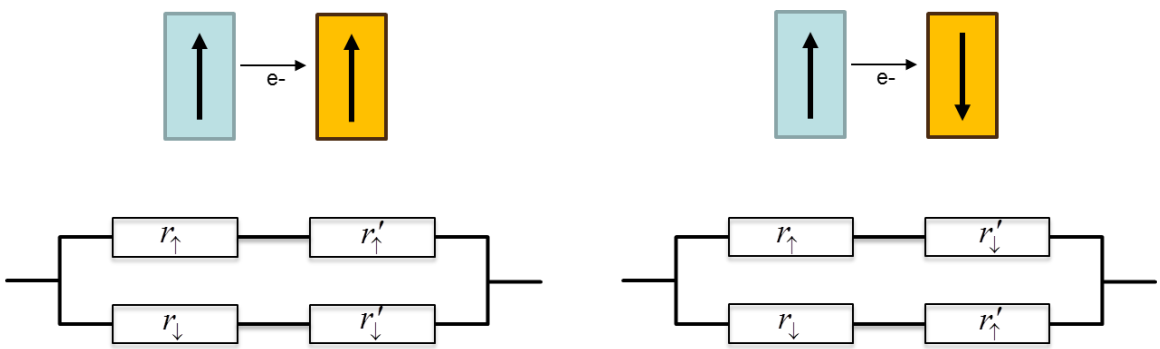

Fig. IV-22. Parallel resistor model for parallel (left) and antiparallel (right) configurations of two ferromagnetic metals. When one of the electrodes switches magnetization direction, the corresponding resistors for spin-up and spin-down switch places in the conduction channels. Maximum magnetoresistance occurs when the magnetizations are anti-parallel.

Since the spin-up channel has greater conductivity and hence a lower resistance, $r_\uparrow < r_\downarrow$ and $r'_\uparrow < r'_\downarrow$. Remembering that the MR is defined as:

$$MR = \frac{\Delta R}{R_P} = \frac{R_{AP} - R_P}{R_P} \qquad (2)$$

the two-resistor model can be worked out to find MR when the two electrodes are equal, i.e. $r_\uparrow = r'_\uparrow$ and $r_\downarrow = r'_\downarrow$:

$$MR = \frac{(r_\downarrow - r_\uparrow)^2}{4 r_\uparrow r_\downarrow} \qquad (3)$$

The above two-resistor model applies when the middle layer has no spin polarization and thus has no effect on the conduction channels. But when the middle layer has a significantly high resistance or spin polarization, the model can be expanded yet again to

account for it. A simple diagram for this model containing parallel channels of three resistors in series is as follows:

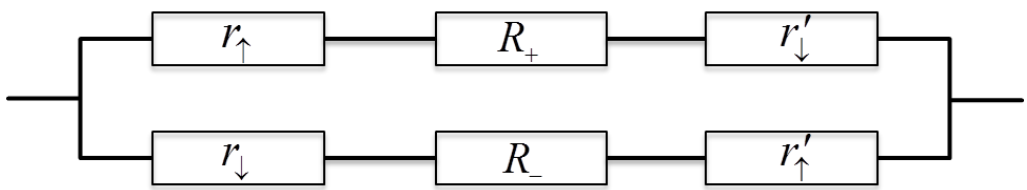

Resistors are inserted into each conduction channel to represent the spin polarization and resistance of the middle layer. In this case, $R_+ < R_-$ represents the middle layer.

If all resistances have different values, there are $2^3 = 8$ possible combinations of resistors. Of these combinations, 4 of them have a degeneracy with one other combination so there are only 4 possible combinations leading to different values for the overall resistance. The possible combinations and their degeneracies are shown below, where the subscripts denote the magnetization direction of each individual layer in one of the parallel channels (e.g. top channel in the diagram).

$$R_1 \equiv R_{\uparrow+\uparrow'} \equiv R_{\downarrow-\downarrow'}$$

$$R_2 \equiv R_{\uparrow-\uparrow'} \equiv R_{\downarrow+\downarrow'}$$

$$R_3 \equiv R_{\uparrow+\downarrow'} \equiv R_{\downarrow-\uparrow'}$$

$$R_4 \equiv R_{\uparrow-\downarrow'} \equiv R_{\downarrow+\uparrow'}$$

(4)

These four possible resistance values can then be compared in cases of different spin polarizations and resistances for the individual layers. If the spin polarization of the middle layer is allowed to go to zero, i.e. the middle layer is nonmagnetic, the model reverts to the model for two resistors described above.

A comparison of the separate resistance values in the individual combinations can be made in order to determine the MR values that can be obtained as the magnetic field is swept from a maximum positive field to a maximum negative field, and vice-versa. A typical progression follows the switching behavior as described in chapter 1, where there is still an anti-parallel window for the two outer ferromagnetic electrodes. Once the magnetic field has changed direction, the softer switching electrode will flip its magnetization first, thus giving rise to anti-parallel alignment with the other electrode. As the field is increased, the other electrode will eventually flip, and the two electrodes will again be parallel.

The three-series resistor model allows considerable diversity in the behavior of the middle layer. Here, several scenarios can be examined. For example, the middle layer could be allowed to flip along with one of the electrodes, going from R+ to R-. In this case, if the middle layer flips with the softer ferromagnetic electrode (primed arrows), the switching sequence would be:

$$R_{\uparrow+\uparrow'} \rightarrow R_{\uparrow-\downarrow'} \rightarrow R_{\downarrow-\downarrow'} \qquad (5)$$

which, based on the above definitions, would produce resistance values in sequence corresponding to:

$$R_1 \rightarrow R_4 \rightarrow R_1 \qquad (6)$$

Subsequently, for the same behaviors as the field is swept back,

$$R_{\downarrow-\downarrow'} \rightarrow R_{\downarrow+\uparrow'} \rightarrow R_{\uparrow+\uparrow'} \tag{7}$$

And again based on the above definitions, the sequence of resistance values is

$$R_1 \rightarrow R_4 \rightarrow R_1 \tag{8}$$

So this would produce an MR result that is very similar to having two ferromagnetic electrodes, with two possible MR values corresponding to the two anti-parallel windows during the magnetic field sweeps. The overall size of the MR would be different because now it is a function of the middle layer's spin polarization, but the switching would occur at the same field values. In like manner, if the middle layer were to flip with the harder ferromagnetic layer (at higher coercive field – unprimed arrows), instead of with the softer layer (at lower field) as was described above, there would again be two resistance values for the MR, but this time the sequence would be:

$$R_1 \rightarrow R_3 \rightarrow R_1 \tag{9}$$

So the resistance value for the anti-parallel state would be different from (6) and (8). However, since there are only two possible and equivalent resistance values for the down sweep and the up sweep, the MR plots would appear qualitatively the same (switching at the same field values) and unless additional details were known, it would be impossible to tell whether the middle layer was switching with the softer or the harder ferromagnetic layer.

However, now consider the scenario where the middle layer is not allowed to flip at all. The down switching sequence would be:

$$R_{\uparrow+\uparrow'} \rightarrow R_{\uparrow+\downarrow'} \rightarrow R_{\downarrow+\downarrow'} \tag{10}$$

which would produce resistance values in sequence corresponding to:

$$R_1 \rightarrow R_3 \rightarrow R_2 \tag{11}$$

Subsequently, for the same behaviors as the field is swept back,

$$R_{\downarrow+\downarrow'} \rightarrow R_{\downarrow+\uparrow'} \rightarrow R_{\uparrow+\uparrow'} \tag{12}$$

And again based on the above definitions, the sequence of resistance values is

$$R_2 \rightarrow R_4 \rightarrow R_1 \tag{13}$$

Now there is a clear difference between the resistance values for the antiparallel states of the down sweep and the up sweep, R_3 and R_4, respectively, and in addition, the parallel states are also different: R_1 and R_2.

Next it is important to consider the possible values that the various resistances of R_1 through R_4 can have. It is possible to define the two resistors for each layer separately in terms of a single resistance for the spin-up channel (although alternatively the spin-down channel could be used) and a value for the spin polarization of the layer. Thus, for the first electrode, which has $r_\uparrow$ and $r_\downarrow$, the spin polarization can be defined as:

$$P = \frac{r_\downarrow - r_\uparrow}{r_\downarrow + r_\uparrow} \tag{14}$$

Next, calculating the values for the individual resistances R1 through R4 gives:

$$R_1 = \frac{(r_\uparrow + R_+ + r_\uparrow')(r_\downarrow + R_- + r_\downarrow')}{(r_\uparrow + R_+ + r_\uparrow' + r_\downarrow + R_- + r_\downarrow')} \tag{15}$$

$$R_2 = \frac{(r_\uparrow + R_- + r_\uparrow')(r_\downarrow + R_+ + r_\downarrow')}{(r_\uparrow + R_+ + r_\uparrow' + r_\downarrow + R_- + r_\downarrow')} \tag{16}$$

$$R_3 = \frac{(r_\uparrow + R_+ + r'_\downarrow)(r_\downarrow + R_- + r'_\uparrow)}{(r_\uparrow + R_+ + r'_\uparrow + r_\downarrow + R_- + r'_\downarrow)} \tag{17}$$

$$R_4 = \frac{(r_\uparrow + R_- + r'_\downarrow)(r_\downarrow + R_+ + r'_\uparrow)}{(r_\uparrow + R_+ + r'_\uparrow + r_\downarrow + R_- + r'_\downarrow)} \tag{18}$$

And these values in turn can be used to calculate expected magnetoresistance changes for the individual states relative to the parallel configuration of R1:

$$MR_{21} = \frac{R_2 - R_1}{R_1} = \frac{(R_- - R_+)[(r_\downarrow - r_\uparrow) + (r'_\downarrow - r'_\uparrow)]}{(r_\uparrow + R_+ + r'_\uparrow)(r_\downarrow + R_- + r'_\downarrow)} \tag{19}$$

$$MR_{31} = \frac{R_3 - R_1}{R_1} = \frac{(r'_\downarrow - r'_\uparrow)[(R_- - R_+) + (r_\downarrow - r_\uparrow)]}{(r_\uparrow + R_+ + r'_\uparrow)(r_\downarrow + R_- + r'_\downarrow)} \tag{20}$$

$$MR_{41} = \frac{R_4 - R_1}{R_1} = \frac{(r_\downarrow - r_\uparrow)[(R_- - R_+) + (r'_\downarrow - r'_\uparrow)]}{(r_\uparrow + R_+ + r'_\uparrow)(r_\downarrow + R_- + r'_\downarrow)} \tag{21}$$

Further examination of these values reveals that it is possible, depending on the combinations of to have $MR_{31} > MR_{41}$ which would give rise to the asymmetrical MR on the down-sweep versus the up-sweep. Indeed, this is the behavior observed in the magnetotransport measurements as the spin rectification effect shown in Fig. IV-18 for the positive bias (+60mV). This occurs when the scenario is that as given by eqns. 10-13, where the middle layer polarization does not change.

Furthermore, if the middle layer is allowed to change to its opposite spin polarization and kept there during the sweeps, this would have the effect of switching MR_{31} and MR_{41}. Thus, the MR would be higher on the opposite sweep direction for the opposite bias direction. This again is what is observed in Fig. IV-18 for the opposite bias (-60mV). The effect of opposite

bias switches the relative height of MR on the down sweep versus that of the upsweep to generate the spin rectification effect. This corresponds very well to the truth table shown in Table 1. Fig. IV-23 shows a representation of the observed rectification behavior as it corresponds to the different MR states.

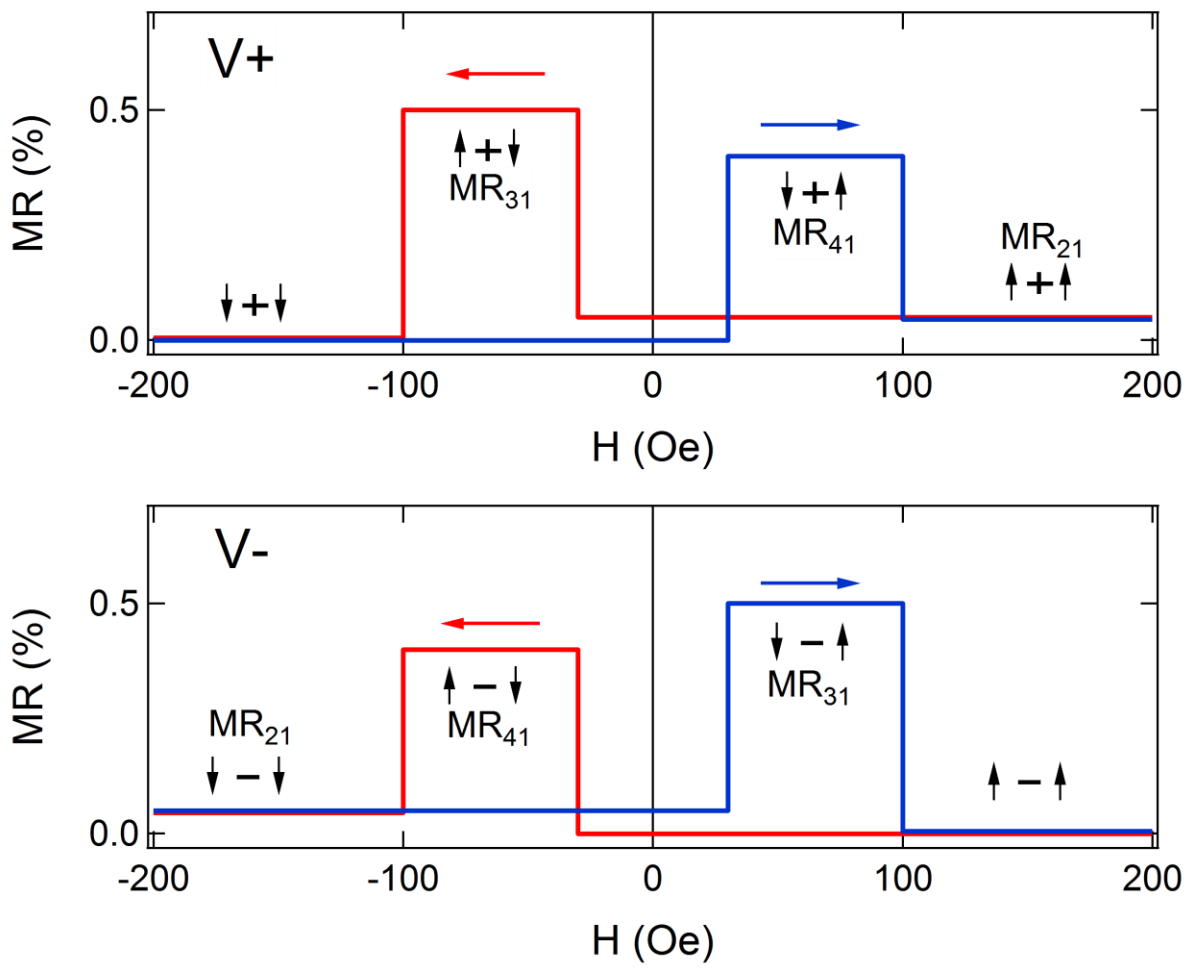

Fig. IV-23 Schematic representation of observed spin rectification effect including magnetic configurations corresponding to the parallel resistors model. The degeneracy of the model, as indicated in equations (4), accounts for the rectification behavior for the different bias directions (V+) and (V-).

In spite of this analysis, however, if the above effect is to take place, the MR_{21} must also be observable. This means the two configurations when the ferromagnetic electrodes are

parallel would produce two different resistance values. This also is indeed the case in Fig. IV-18 and in all of the magnetotransport measurements, especially at the higher biases where it is more apparent. It is shown in greater detail in Fig. IV-24, where the difference in the two parallel states has been plotted as a function of bias for different temperatures. The difference becomes significant at high bias, but still remains relatively low overall at 0.05% change.

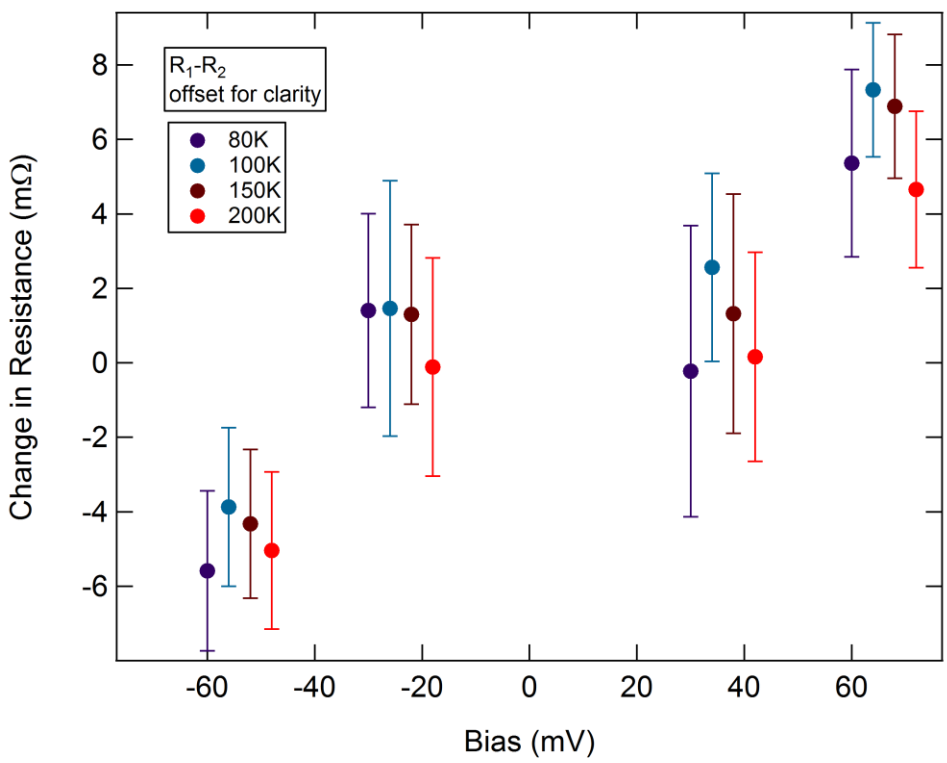

Fig. IV-24 Difference in resistance values of parallel configurations of ferromagnetic electrodes during magnetotransport scans. This corresponds to MR_{21} in the analysis presented above. Horizontal axis was shifted slightly for clarity of the 4 temperatures at each bias. The 4 bias values are: -60mV, -30mV, +30mV, and +60mV. There is a clear bias dependence to the difference, with maximum difference of approx. 6mΩ at +60mV. This value is well below the difference in resistance obtained from results for the anti-parallel configurations, approx. 20mΩ. This does not agree with the parallel resistors model which would require the two differences to be equal or the parallel case to have a higher difference. There is also no effect at low bias, which agrees with the MR observed for MR_{31} and MR_{41} – i.e. no low bias rectification effect there either.

In spite of this observation, calculation of the expected values from the model reveals that MR_{21} must be greater than or equal to the relative difference between MR_{31} and MR_{41}. This expected result is shown in Fig. IV-25 (dashed lines). A change on such a scale cannot be seen in Fig. IV-18, Fig. IV-23 or any of the measurement results.

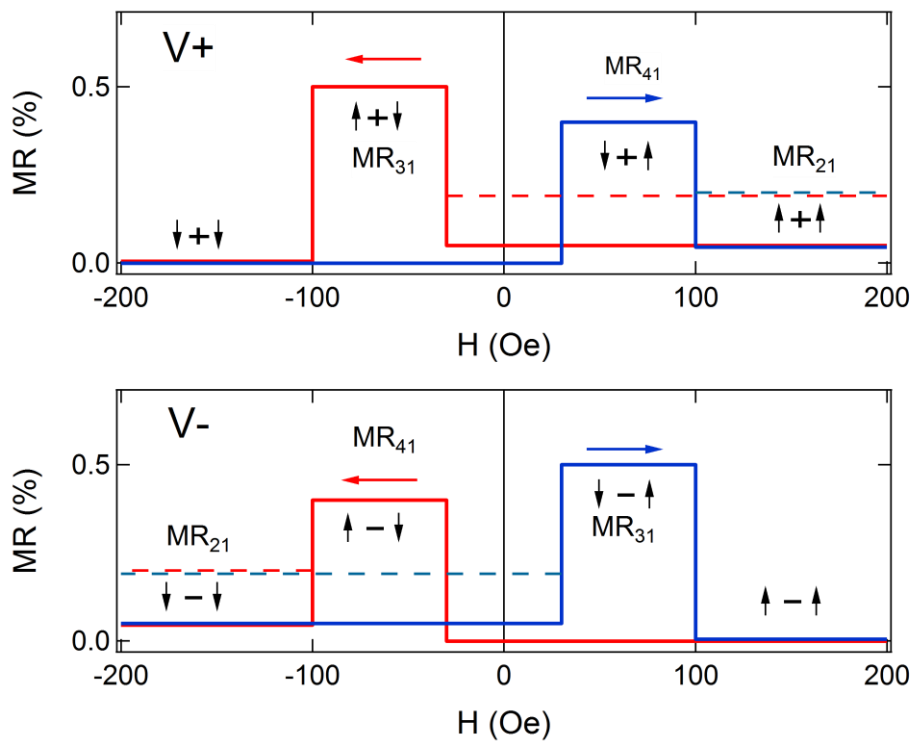

Fig. IV-25 Diagram of results from the parallel resistors model with actual expected resistance values for the state MR_{21} (dashed lines) compared to the observed behavior (solid lines). There should be a greater change in resistance for the MR_{21} configuration.

Conclusions from the Parallel Resistors Model

The parallel resistors model effectively describes the magnetotransport behavior of the VT spin valve as it relates to the spin rectification effect of the antiparallel configurations. In these cases, the parallel resistor model accounts for the fact that there is a middle layer which

is spin-dependent. The model demonstrates that there is no way to obtain a spin rectification effect without a spin-dependent middle layer. If the middle layer were merely spin-dependent, and could not be controlled by the bias, both MR plots for V+ and V- would be the same. However, since that is clearly not the case, it is concluded that the spin-dependent VT layer can be controlled by the bias.

A shortcoming of the parallel resistors model is that the parallel configurations are not adequately represented. There is a detectable lifting of the degeneracy of the two parallel states as shown in Fig. IV-24, and it does fit the model in terms of its directional dependence on the bias. In other words, the qualitative behavior is there. However, the quantitative behavior is not: the magnitude of the degeneracy-lifting expected from the parallel case does not match the model.

This leads to the conclusion that there is likely some other factor that is reducing the relative difference in resistance between the two parallel states. Perhaps some interaction with the local magnetic field at the interface when the electrodes have parallel magnetization is occurring to enhance conductivity.[12,14]

Another explanation for the discrepancy of the parallel configurations in the model is obtained when the model is expanded. If another spin dependent pathway is allowed to open that did not exist before, the correction can account for the observed behavior. This new parallel channel is shown in Fig. IV-26. The channel does not depend on the VT spin polarization, but does depend on the switching of the bulk ferromagnetic electrodes and has a high MR effect. Essentially it is a parallel channel with just an insulator between. It should be noted that it could also be a channel with the VT in between (or possibly even just another

channel in the VT itself), but in this channel the VT has no spin-polarization – similar to what was observed for sample CC38.

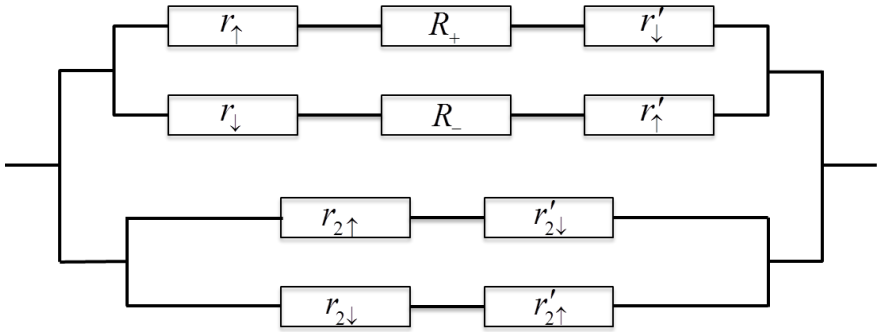

Fig. IV-26 Schematic diagram of the extended parallel circuit. The circuit contains two main parallel branches, one has the spin-polarized middle layer, and one does not have a spin-polarized middle layer. The two branches are each comprised of their own two parallel channels of spin-polarized elements, leading to a total of four channels.

The increased conductance of this additional parallel channel effectively lowers the resistance in both of the parallel magnetization configurations, so that MR_{21} becomes much lower. The conduction in the parallel case is dominated by the two-resistor channels without the middle layer. In contrast, in the antiparallel configurations, the greater resistance of the two-resistor channel makes it so that the spin-rectification effects of the spin-polarized middle layer in the three-resistor channels can become significant and much more observable.

IV.6. I-V Measurements at Specific Magnetic Configurations

In addition to the MR measurements described above where only a few bias points were taken as the magnetic field was scanned, full I-V measurements were taken at selected fixed magnetic field values. The purpose of these I-Vs was to examine the behavior of specific magnetic configurations that led to MR effects. For example, a full I-V measurement was done when the field value was known to give parallel alignment of the ferromagnetic electrodes, e.g. at a large field, and then the field was changed to to give anti-parallel alignment of the ferromagnetic electrodes for the next I-V. In this way, parallel and anti-parallel configurations were examined over the entire hysteresis loop. The fields were selected based on magnetotransport scans done previously in the manner described above and as shown in Figs. IV-17 and IV-18. The I-V measurements were done at varying temperatures from room temperature to as low as 4K. The maximum range of the I-Vs was approximately $\pm$ 80mV.

IV.7. Discussion of Results from I-V Measurements

For all of the measurements, the same concave-down differential conductance as shown in Fig. IV-12 was observed. However, by subtracting out the differential conductance curves taken for the parallel configuration, it was possible to detect the changes in the magnetoresistance (or magnetoconductance as desired) relative to the parallel configuration.

Fig. IV-27 shows the results for I-V measurements taken at 80K. The bottom plots in the Figure show the magnetoresistance for the anti-parallel configuration during a magnetic field sweep down (left panels) or up (right panels). The bias sweep in each plot has been sorted into positive increasing (up) shown in blue, and negative decreasing (down) shown in red. The standard convention followed when conducting the I-V measurement was to start at zero bias, sweep up to the maximum positive bias, then sweep back down to the maximum negative bias, then sweep back to zero.

The MR plots show a hysteresis on either side of zero depending on the AP configuration. For the magnetic field down sweep (left side of graph), the hysteresis occurs when sweeping the bias down. A higher MR is observed on the negative bias side during the down bias sweep. When returning (increasing bias) to zero after reaching a maximum negative bias, the MR does not return to as high a value as before and an opening in the curve occurs.

A similar behavior occurs for the magnetic up sweep plotted on the right side of Fig. IV-27. In this plot, the MR increases during the up bias sweep to its highest value which is offset from zero to the positive bias side this time. In like manner, after reaching the positive bias maximum, the MR returns at a lower value for the same bias where there was previously a maximum in the MR, so an opening occurs this time on the positive bias side. The two openings for the magnetic field up sweep and down sweep appear to mirror each other.

The relative asymmetry in MR for a particular bias direction and magnetic field sweep direction is reminiscent of the rectification effect. Consulting the logic table IV.1, it is expected that the MR would be higher for a positive bias on the down magnetic field sweep than for the positive bias on the up magnetic field sweep. Comparing the right-hand sides of the two

graphs, this does appear to be true in general, with the exception of the spiked part of the hysteresis. Now comparing the negative bias side, it is expected from the logic table that the MR would be higher on the up magnetic sweep than on the down magnetic sweep. In this case, the two left sides appear to be approximately equal except for the hysteretic portion where again the opposite from expected behavior is occurring, i.e. the down magnetic sweep has higher MR instead of the up magnetic sweep. This behavior will be explored further in the discussion which follows.

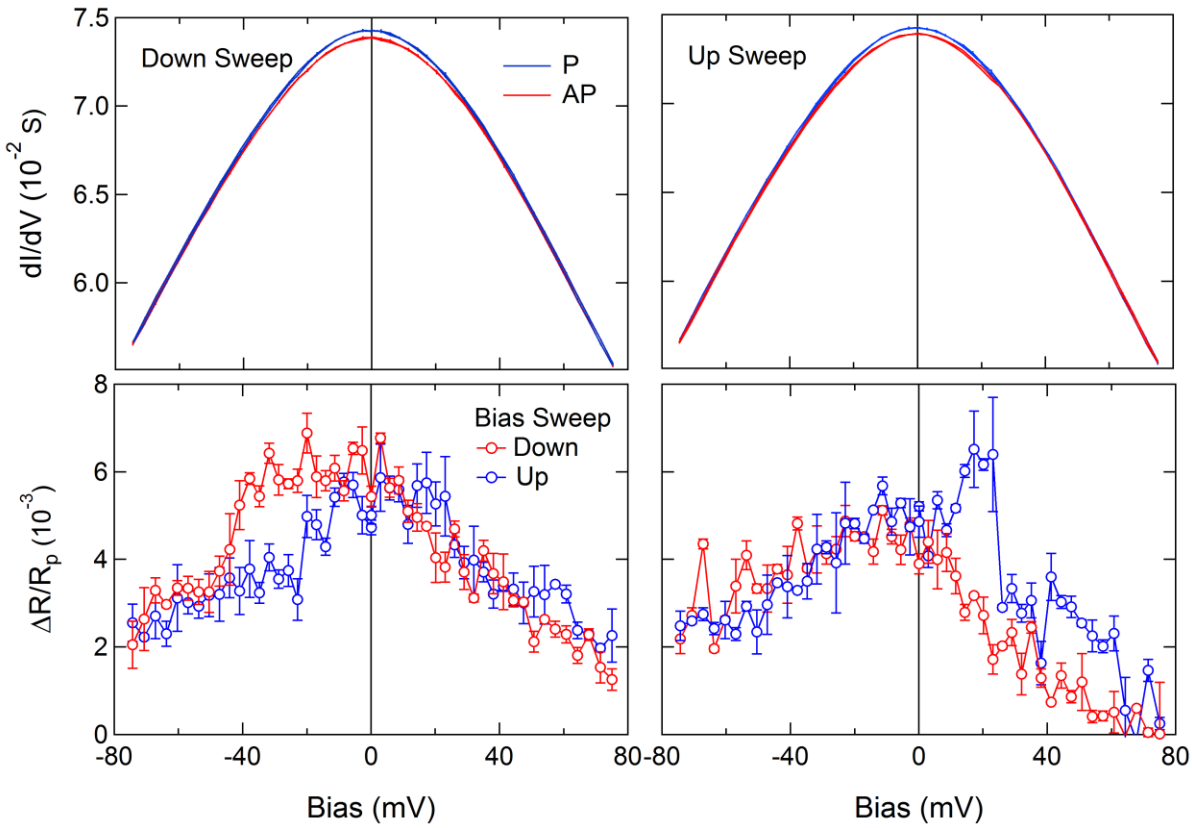

Fig. IV-27 Results from 80K I-V measurements taken at different magnetic configurations corresponding to anti-parallel and parallel states for the down sweep of the magnetic field at 80K. Top panels: Differential conductance plots for the parallel (P) and anti-parallel (AP) configurations taken during the magnetic field down sweep (left) and magnetic field up sweep (right). Bottom panels: Plot of the MR for the AP configuration as a function of bias corresponding to the respective magnetic field sweeps in the top panels. Plots separated into up and down sweeps of the I-V for greater clarity. There is a hysteresis present.

Another set of I-V curve data, this time from measurements at 200K, is shown in Fig. IV-28. Here, more measurements were taken around the fields that were expected to produce the anti-parallel configuration. The MR plots for this temperature are shown above in Fig. IV-8, where at the high temperature, the VT is in its high-spin form and the switching fields exhibit high resistance regions that are overlapping and symmetric about zero field.

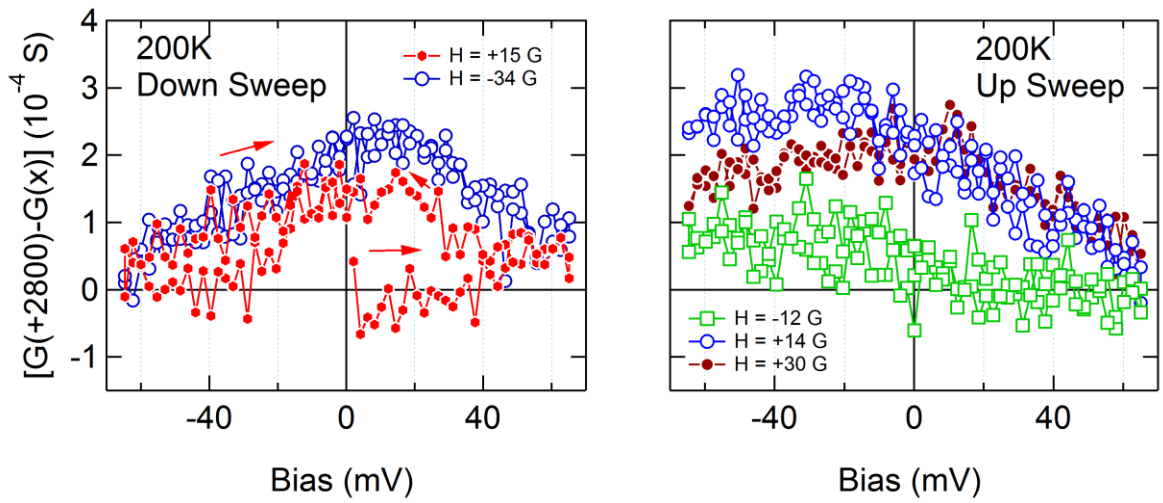

Fig. IV-28 Results from 200K I-V measurements taken at different magnetic configurations for the down sweep of the magnetic field. In these figures, the differential conductance at fields for different expected anti-parallel configurations was subtracted from the one for the parallel configuration. A positive value for the plotted points means higher resistance, so the values plotted qualitatively correspond to the MR.

In Fig. IV-28, for the down magnetic field sweep, two I-Vs were measured at +15 Oe, prior to crossing zero and at -34 Oe after crossing zero. For the +15 Oe, the MR is zero until the bias becomes high. After that, the MR appears to increase as the bias decreases through zero, and for the remainder of the measurement is non-hysteretic with an apparent symmetrical peak at zero. For the -34 Oe plot, the MR curve is non-hysteretic, but has a slight offset to the

positive bias side. This is consistent with the rectification table in that an offset of the peak to the positive bias side would be expected for the down sweep, and an offset to the negative bias side would be expected for the up sweep, as shown in Fig. IV-29.

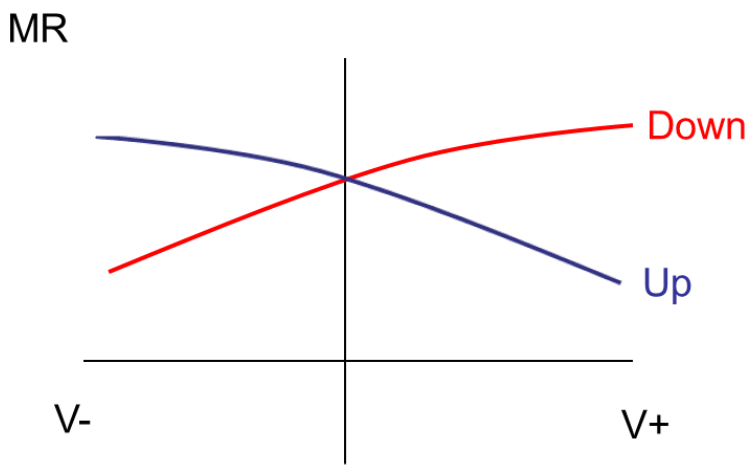

Fig. IV-29 Model of MR versus bias for AP configurations of different magnetic field sweep directions, as expected from the rectification effect shown in Table IV.1. These behaviors correspond to the observed behaviors for the magnetic field sweeps shown in Fig. IV-18.

In contrast with the expected behavior shown in Fig. IV-29, which is based solely on the observed behaviors from the MR sweeps, the plots in Fig. IV-28 appear to decrease back towards zero MR at higher bias. This behavior is expected based on observed MR effects in spin valves, where the highest MR occurs around zero bias.[15] The higher energies at higher bias usually acts to increase conduction while at the same time reducing any spin dependency due to scattering.

However, examining the behavior of the plots for the up magnetic sweep on the right side of Fig. IV-28, the expected offset behavior of the peak on the negative bias side is apparent, particularly for the measured curve at +14 Oe. This curve increases to a high ΔG (qualitatively the MR) value and stays there on the negative bias side. The behavior of the

other two curves is of interest. These curves were measured at values of -12 and +30 Oe. Both of these values are expected to be within or very close to the AP window as shown in Fig. IV-8 for the MR scans. However, there are apparent differences in the curves. It is possible to explain these differences with a model that assumes, in addition to the rectification, there is shifting of the switching fields as a function of bias.

This shifting behavior of the switching fields as a function of bias has been observed in the MR scans at a specific temperature and is shown in Fig. IV-30. It is reminiscent of the overall effect of the shifting of the switching fields as discussed above in connection with the change associated with the tautomeric transition by temperature as shown in Fig. IV-18. It is clear from Fig. IV-30 that the bias does cause the shift in the switching fields that is similar to the shift occuring due to the tautomeric transition. The data in these two figures were taken from the magnetotransport scans. It is thus not surprising that a similar effect is observed in the I-V scans at higher biases.

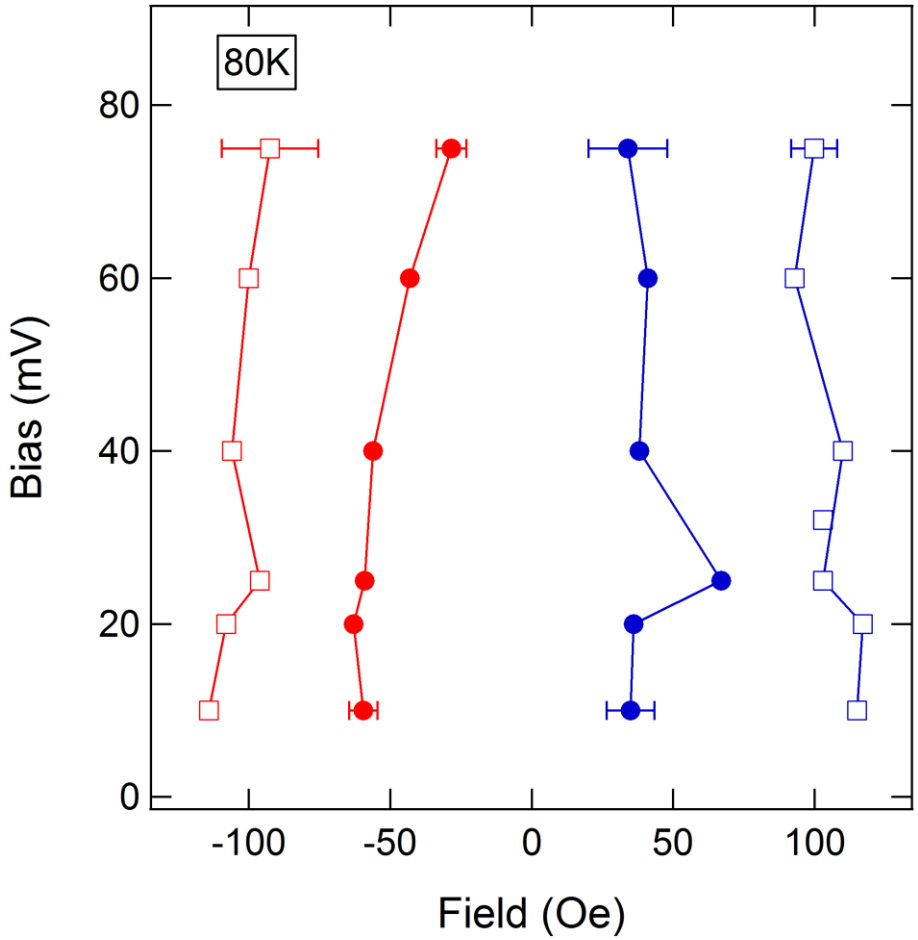

Fig. IV-30 Bias dependent shifting of the switching fields. Switching fields move inward towards zero with increasing bias magnitude. Data was collected from magnetotransport scans so the bias is an absolute value that represents both positive and negative values.

The I-V data (differential conductance) provides additional details that cannot be observed from Fig. IV-30. Because of the toggling method that was used to collect the data for the magnetotransport scans and Fig. IV-30, where the bias was alternated between positive and negative as described for the magnetotransport measurements above, and as a result of the apparent hysteretic behavior that occurs as a result of high bias as discussed in the section

above (see, e.g. discussion of the remanent states shown in Fig. IV-18), there is no way to distinguish the effects of positive and negative bias from the data collected in the magnetotransport scans. Hence, Fig. IV-30 is limited to a single absolute value of bias which is plotted. However, for the I-V measurements, the bias direction is held for a long enough time so that its directional dependence can be examined.

Now returning to Fig. IV-28, and knowing that the bias can in fact shift the switching fields of the MR window, the behavior of the curves for the magnetic up sweep can be explained. The shift of the window is shown in Fig. IV-31 for the three separate field values, and the corresponding MR at those values matches the position of the MR peak in the window. In Fig. IV-31, it is assumed that in fact the positive bias shifts the switching window outward from zero, and the negative bias switches the window inwards towards zero.

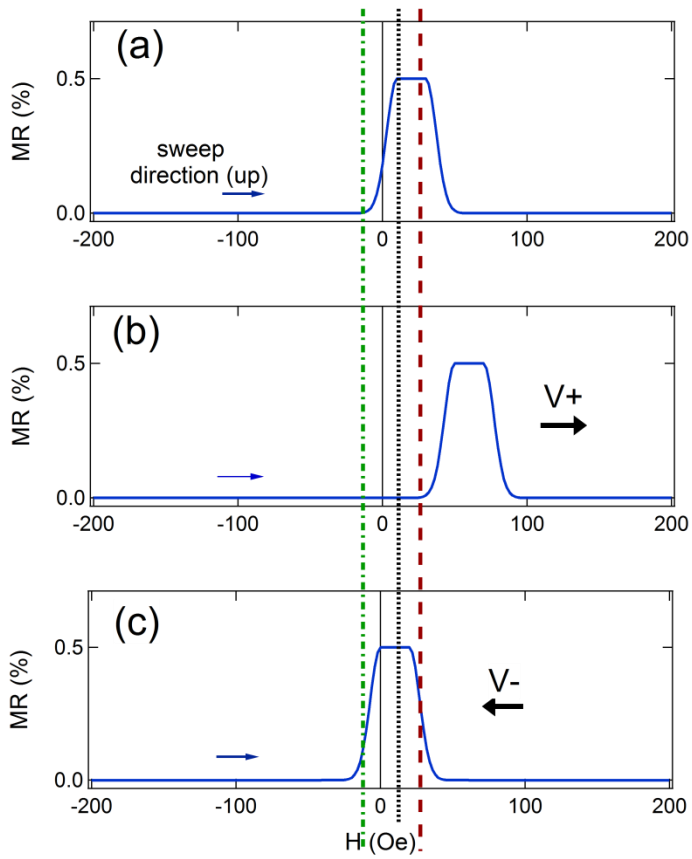

Fig. IV-31 Upsweep at 200K. Example of shifting of the switching field during the magnetic field upsweep. The shift in (b) shown is expected due to increasing the positive bias. The shift back resulting from negative bias is shown in (c). The green dot-dash line, black dotted line, and the brown dashed line correspond to the behavior for H=-12G, H=+14G, and H=+30G, respectively (see Fig. IV-25)

The effect can be observed in the MR scans of Fig. IV-8, where the outer switching field does systematically move outward for positive bias, and inward for negative bias.

Additional I-V measurements at 100K show that for the down sweep, the asymmetry is reversed so that the negative bias causes shifting towards zero of the switching field. In Fig. IV-32, for a field of -20 Oe, the behavior is as shown in the hypothetical model of Fig. IV-33. Initially the field is in the antiparallel window as seen in the MR scan of Fig. IV-34. Then the bias is increased in the positive direction and increases as is consistent with the sloped behavior of

the MR in Fig. IV-34. At a certain point, because of the positive bias, the window moves outside of the measurement field (Fig. IV-33(b)), causing the sharp drop to a low MR. This condition remains until the negative bias can shift the field back (Fig. IV-33(c)).

A separate I-V taken at a field that was directly on the antiparallel window (-42 Oe) is more symmetric when it is likely that the bias in either direction is not capable of shifting the switching fields enough to move outside the window. This is shown in the blue trace of Fig. IV-32.

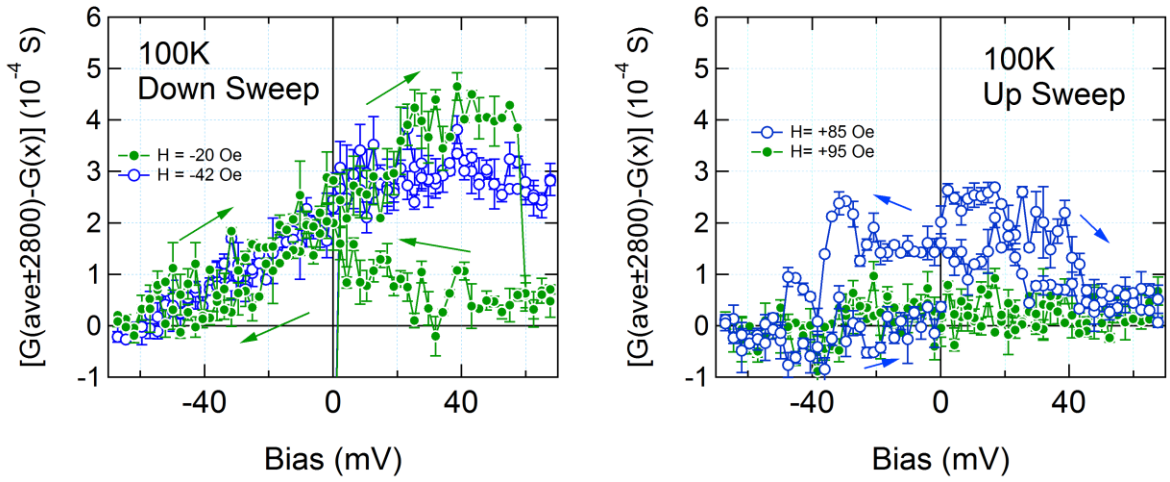

Fig. IV-32 Plots of differences in differential conductance at 100K for AP configurations. The down sweep shows clear hysteresis for the -20 Oe curve. For the up sweep, the curve appears to go into and out of an MR region at low bias.

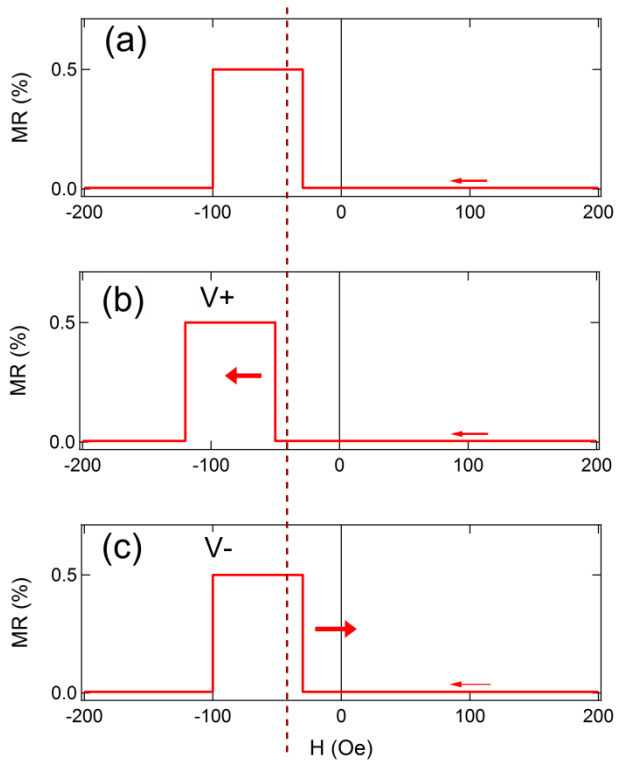

Fig. IV-33 Example of shifting of the switching field during the magnetic field downsweep. The shift in (b) shown is what is expected due to increasing the positive bias. The shift back towards zero results from negative bias is shown in (c).

For the upsweep in Fig. IV-32, the curve corresponding to H=+85 Oe on the upsweep matches the narrow MR spike shown in Fig. IV-34 for measurement at 100K. Here it is apparent that the higher positive bias moves the switching window away from the measurement field (+85 Oe), then as the bias is lowered, the window returns, and then the negative bias moves the window away again. It is not possible to determine which direction the shift is occurring for this measurement because of the symmetry.

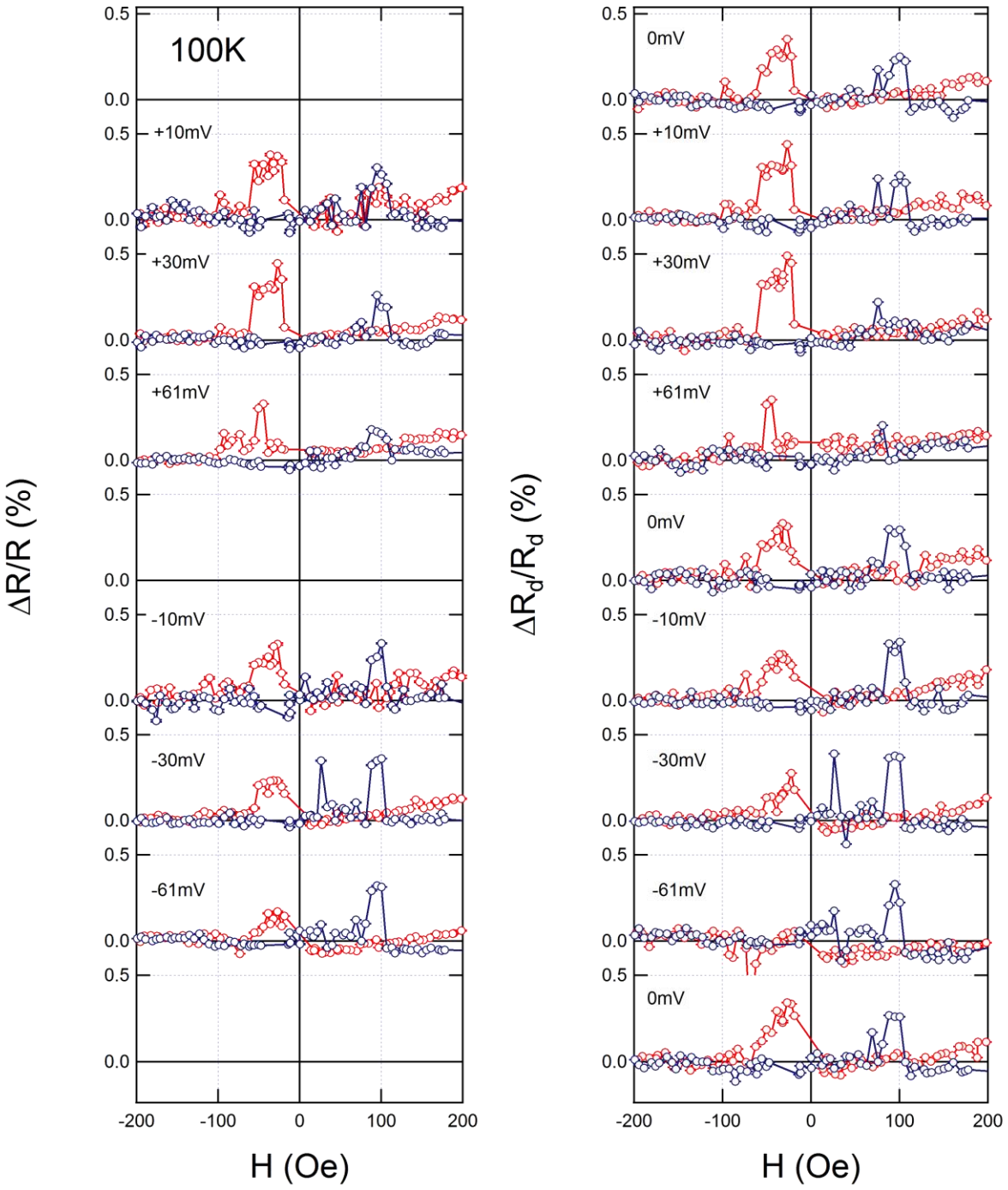

Fig. IV-34 MR data taken at 100K. This data shows the switching windows that create the MR matching the behaviors of the I-Vs shown in Fig. IV-32. Some sample degradation has occurred in this later measurement.

The set of I-Vs measured at 180K did not yield any illuminating information with regard to the bias-directional shifting of the AP window, however, the rectification offset of the down sweep versus the up sweep is apparent in Fig. IV-35. In this plot, all traces taken during the loop are included, showing there were no partial traces that had movement into or out of the AP window. In general the MR was on or off, and when it was on, it followed the rectification scheme shown in Fig. IV-29 with the peak offset to one side of zero depending on the sweep direction.

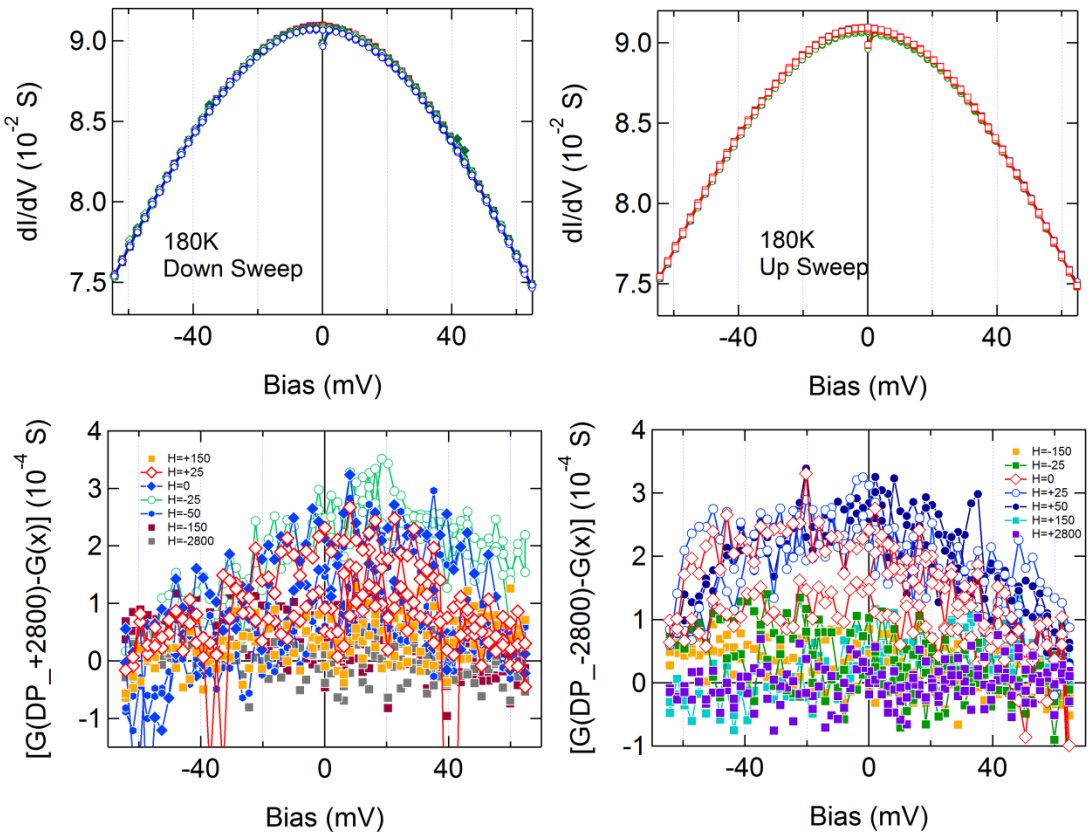

Fig. IV-35 I-V sweeps taken at 180K. The full set of sweeps for 180K are included in the bottom plots for purposes of comparison.

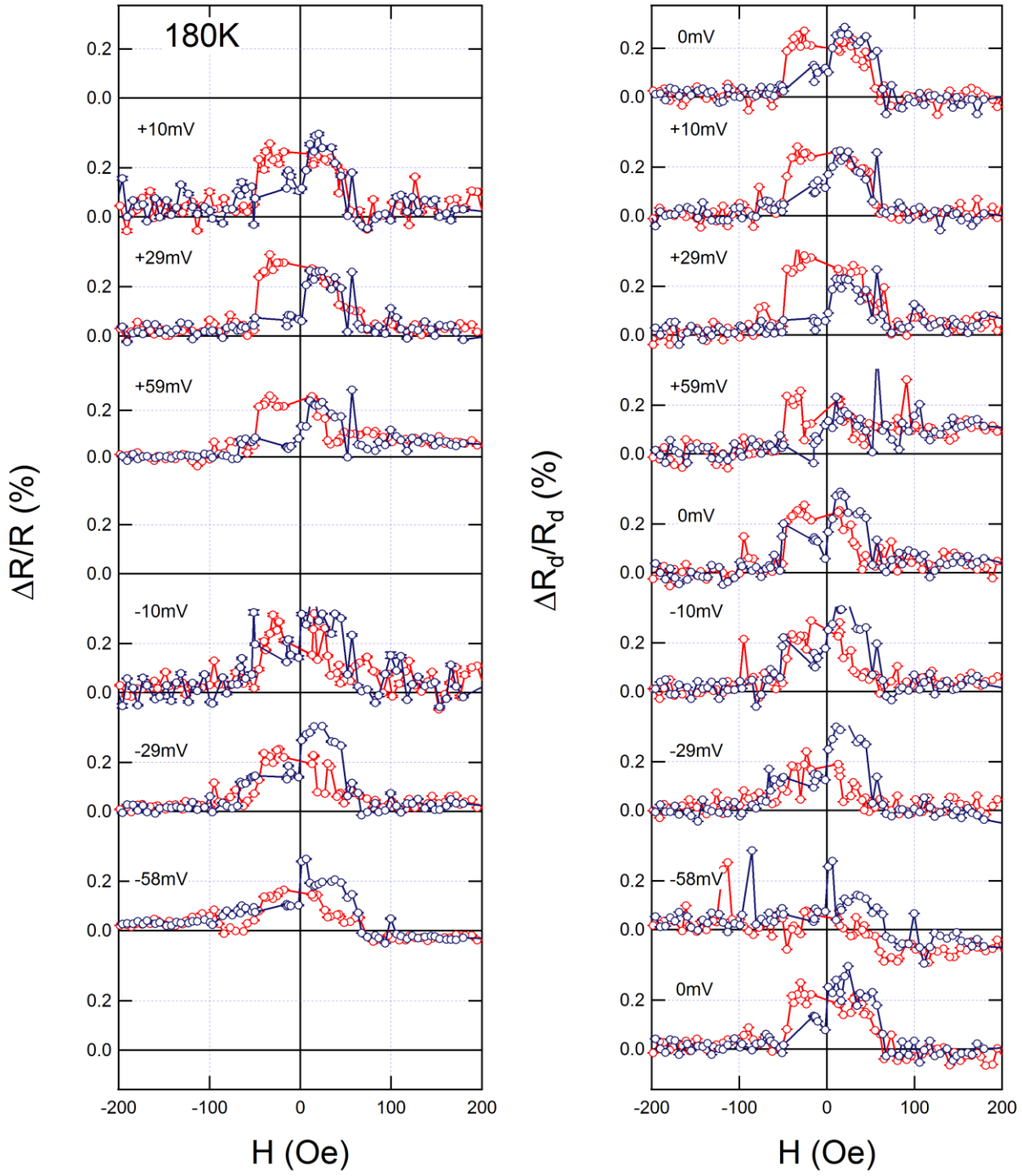

Fig. IV-36 MR data taken at 180K. This data shows the switching windows that create the MR match the behaviors of the I-Vs shown in Fig. IV-35.

I-V Behavior: Conclusion

There are several key effects which emerge from examination of the I-V data:

The two types of effects which emerged from the MR scans are present: (1) the rectification effect and (2) the shifting of the switching fields. The rectification effect (1) can be seen as the offset in the peak value of the differential conductance subtraction plots versus bias for a given AP configuration. This behavior follows the scheme shown in Fig. IV-29. The shifting effect (2) is observed to occur when the AP configuration field is not sufficiently chosen, so that the bias is able to move the AP window away from the selected field, causing the MR to decrease. Matching the observed MR scans up to the I-V data reveals that the positive bias is likely causing the switching fields to shift outwards, and the negative bias is likely causing the switching fields to shift inwards.

Another significant effect is the hysteretic behavior that is clearly observed in the plots at 80K (Fig. IV-27). Openings on either side of zero bias depending on the magnetic field sweep direction indicate that there are accessible states which can become filled and prevent further conduction, increasing MR. It is likely these are spin dependent trapped states. Subsequently, a higher bias, or the passage of sufficient time, is necessary to remove the trapped condition and on the return downward bias leg of the I-V, the states are accessible again so conduction stays high (and MR low).

It is believed that there is considerable hysteresis, like the one specifically observed above at 80K, in all of the measurements, especially in the MR scans. For this reason, the bias-direction dependent shifting of the switching fields could not be easily observed in the MR scans, and instead an absolute value effect is observed in Fig. IV-30. This indicates the negative

bias effect of shifting the fields inward is dominate over the positive bias effect at 80K, which is not too surprising if it is considered that conversion to the higher-spin form is likely happening and the conversion back to the low-spin form is not very fast.

IV.8. Light Effect

Two separate experiments were performed at 80K to determine how shining light on the tautomer would affect the magnetotransport behavior. The cryostat's window is aligned with a hole in the copper plate and mounting plate for the sample. To illuminate the sample, aluminum foil that was covering the cryostat was removed, so that light could be transmitted from an external laser source through the window and through the hole to the bottom of the glass slide on which the crossbar device was made. The light would then go through the bottom electrode to reach the tautomer film in the middle of the vertical stack, as shown in Fig. IV-2.

The light had the effect of moving the switching fields towards zero as shown in Fig. IV-37. It took a certain amount of time for the light to take effect. Initially there was a gradual shift of the switching fields from the separated windows at 80K to the overlapping variety of the higher temperature measurements. The shift happened during the measurement. Also, the overlap of the windows was not fully complete. The down side had a more complete overlap of zero field. The up sweep side shows a shift, but does not fully cross zero. Once the laser was turned off, as shown in Fig. IV-37(b), a dramatic shift of the windows away from each other and zero occurred. With the laser on again in Fig. IV-37(c), the overlapping behavior

returned. The resistance during this measurement stayed within a range of 0.02 Ω during the measurement so any effects due to heating can be ruled out.

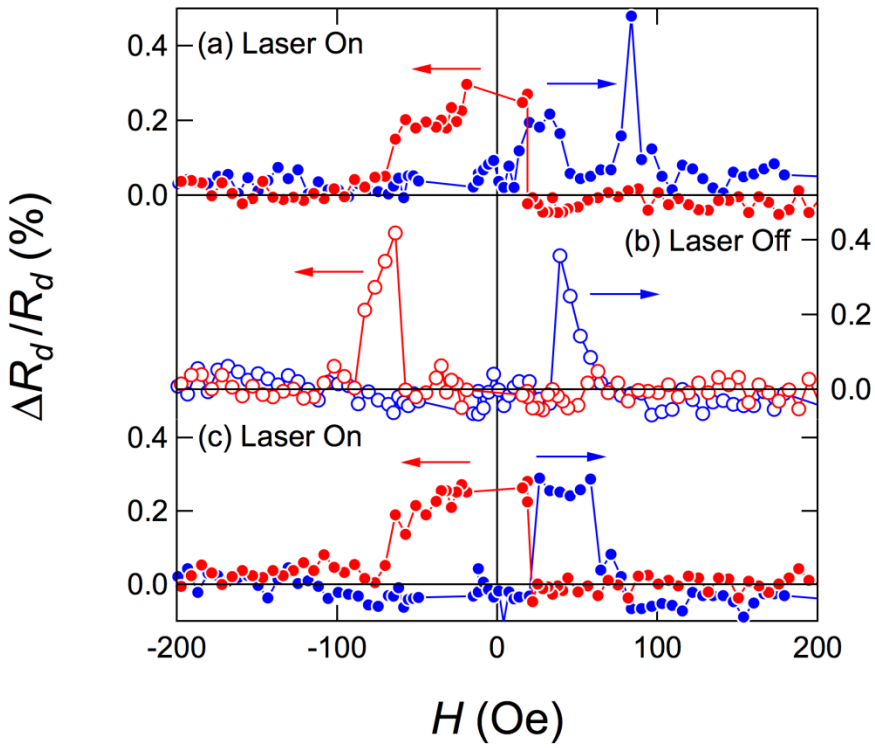

Fig. IV-37 Light experiment. Shift of the switching fields as a result of the laser being on or off.

Conclusion

At 80K, the laser light drove the conversion of the valence tautomer from the low spin Co(III) to its high spin Co(II) counterpart. This in turn caused the observed behavioral change that was seen when transitioning by temperature from low temperature to high temperature: the movement of the switching fields towards zero and for the downsweep, actually crossing zero. Thus, the light experiment shows the presence of the VT layer and confirms the observed magnetic behavioral transition is caused by VT transition.

IV.9. 4K Behavior

The sample was cooled down to liquid helium temperature, 4K, to observe its behavior. At this temperature, the sample showed behavior in its MR scans that was similar to its behavior at room temperature in the high-spin state. In particular, for measurements toggling at biases of ±15mV and ±45mV, the down sweep showed a clear transition to switching before the magnetic field had crossed zero, i.e. before it had switched polarity. This was never observed in any low-temperature measurements below 130K, except when the light illuminated the sample at 80K as discussed in the previous section.

According to prior research done on the tautomer[1], the molecule has a separate anti-ferromagnetic low-spin state below 10K. It is likely that the measurement at 4K indeed observes an anti-ferromagnetic coupling behavior similar to that of the high-spin state. This result serves as further confirmation not only that the tautomer is influencing the magnetotransport, but also that the tautomeric behavior in the high spin state is anti-ferromagnetic in nature.

It is additionally noted in Fig. IV-38 that the higher bias toggling measurement actually drove the switching field for the down sweep back across zero. This effect is the opposite of the type of effect observed in Fig. IV-30, where higher bias caused the switching fields to move towards zero. This is consistent with the known behavior of the tautomer in that the high bias is driving a conversion to the tautomeric state which is next highest in temperature, i.e. converting from the 4K antiferromagnetic state to the low-spin state.

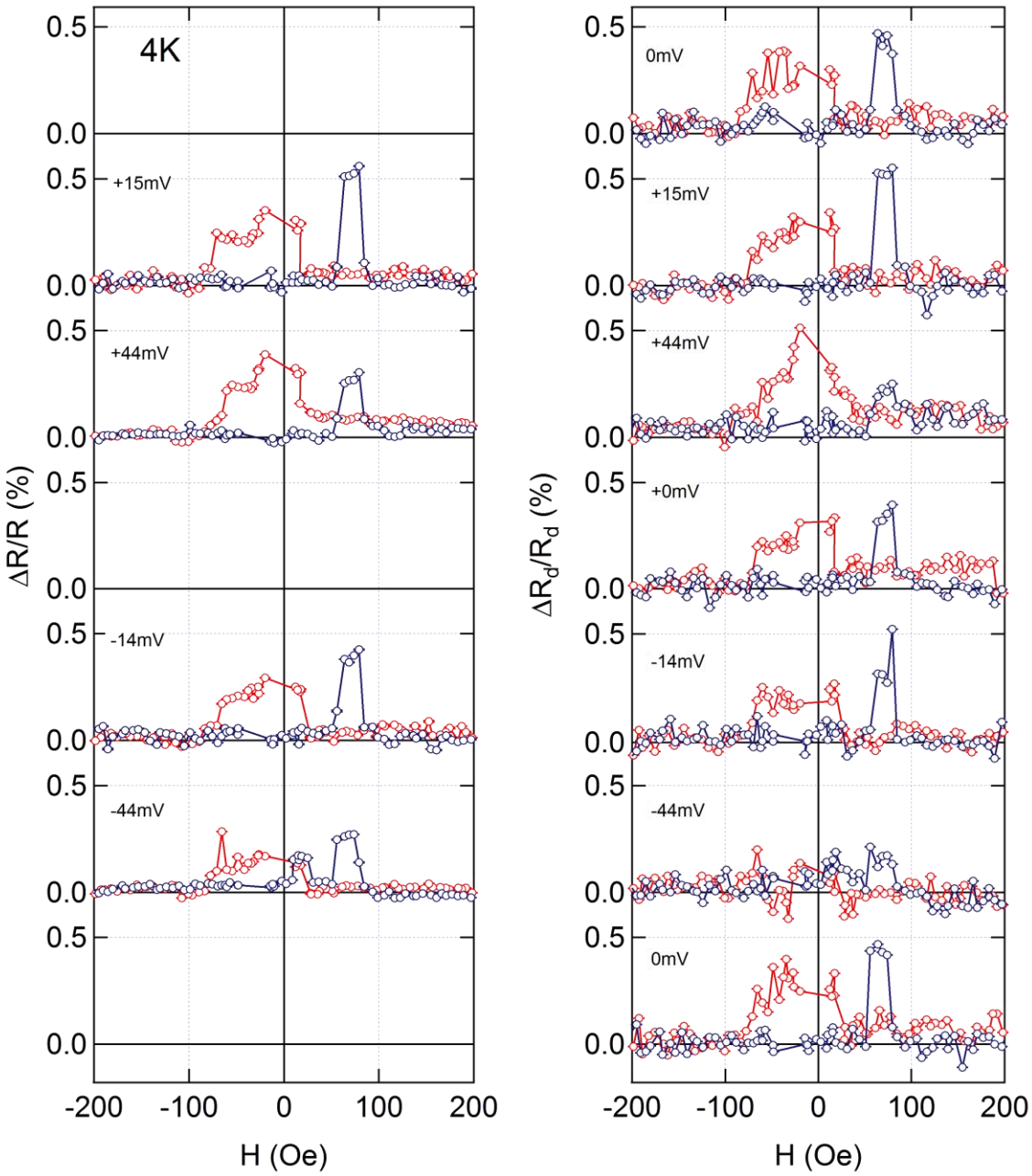

Fig. IV-38 MR data taken at 4K. The experiment was done by toggling of bias values of ±15mV and ±45mV.

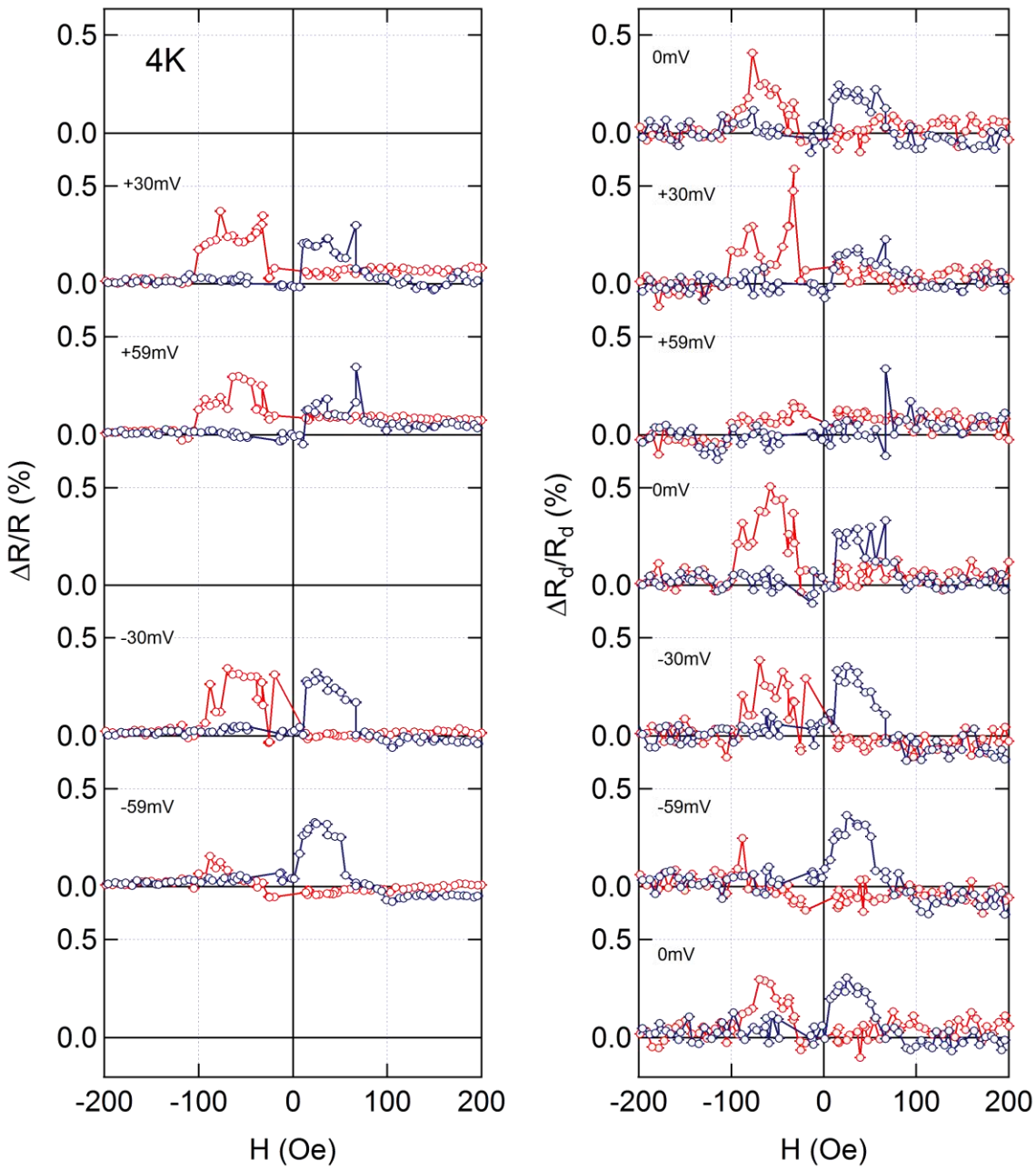

Fig. IV-39 MR data taken at 4K. The experiment was done by toggling of bias values of ±30mV and ±60mV.

I-V data at 4K shows an apparent symmetry in Fig. IV-40. Here, the sweep direction is plotted in different colors. Again, the behaviors for the down magnetic sweep and the up

magnetic sweep appear to be mirrored. This is expected from the rectification effect as well as shifting of the switching fields as described above.

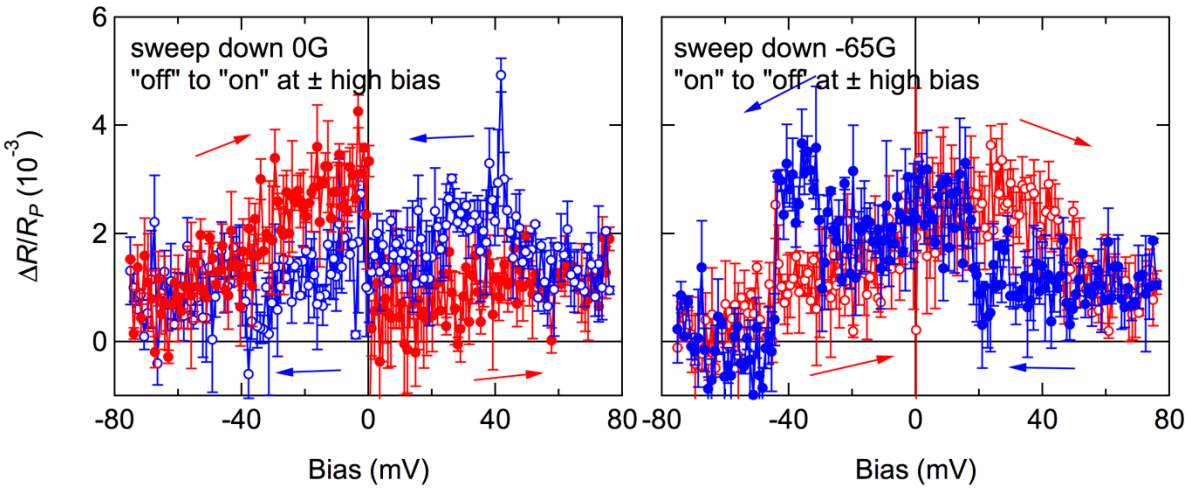

Fig. IV-40 I-V data from 4K. The behaviors for the down magnetic sweep and the up magnetic sweep are mirrored.

AF Coupling

Although the rectification effect demonstrates, through the parallel resistor model, the presence of an spin-dependent intermediate layer, the shifting of the AP window for the high-spin state compared to the low-spin state remains to be explained. One interpretation of the switching field behavior is that the high-spin state, with its five unpaired electrons, is anti-ferromagnetically coupling to one of the ferromagnetic electrodes at the shared interface. The switching field could in fact change depending on the energy associated with this coupling, Moreover, if the coupling itself involved a greater or lesser population of the high-spin state versus the low-spin state, the energy could be a function of that. Moreover, the switching field could change in a continuous manner, shifting position depending on the population. Thus it is

likely that the amount of conversion to the high-spin tautomeric form actually determines the switching field.

In Fig. IV-41, the possible scenarios involving anti-ferromagnetic coupling are depicted. The down magnetic sweep only is shown (usually the red leg of the MR plots). For scenario i), the VT is coupled to the cobalt top layer. A switching field can occur before the magnetic field has reached zero. Once the magnetic field energy has fallen below the threshold energy required to keep the antiferromagnetic interfacial layer from aligning in antiparallel to the cobalt, it will flip. This causes an increase in the MR as shown. Subsequently, the MR stays high until the permalloy, the softer switching ferromagnetic metal, flips to align with the interfacial layer. Essentially the entire MR is derived from the alignment of one of the metals with the interfacial layer. So once the permalloy has flipped, the two layers governing the MR are now aligned, so MR drops to zero again. Next, the cobalt flips at a larger field. This causes a momentary anti-alignment of the interface which prefers to anti-align with the cobalt. However, since the field is now very large at the cobalt's coercive field, the interface flips back to align in parallel with all layers. This quick flipping and return causes a spike in the MR.

Examining Fig. IV-17 reveals that all of these features are present in the high-temperature measurement. Dashed lines show the correspondence between switching fields of the metal, in particular, the cobalt for high and low temperature.

The scenario shown in ii) is what would happen if the VT were coupled to the permalloy, which is clearly not the case since the behavior depicted is not observed.

It is important to note that the rectification effect could still be operative since it remains a function of the intermediate layer, itself controlled by the bias. In the parallel

resistors model presented above, one of the electrodes is now simply replaced with an interface to satisfy the AF-based shifting that is happening. Thus, both effects are present and can be observed independently. This is why the rectification effect occurs throughout all of the measurements regardless of whether the tautomer is in the high-spin or the low-spin state.

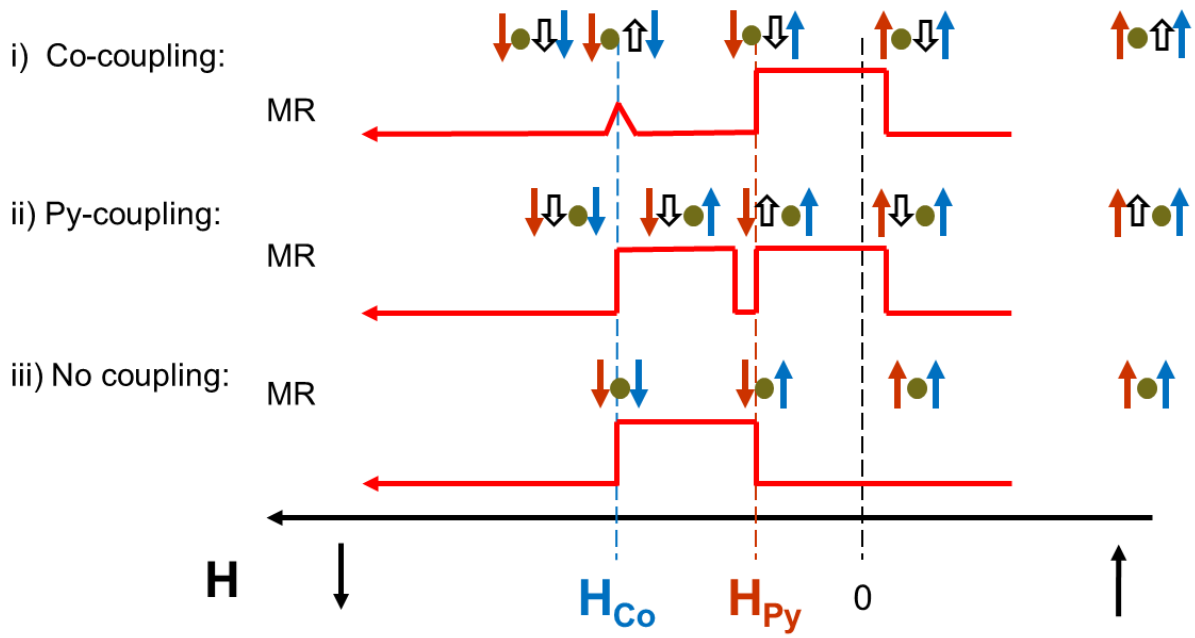

Fig. IV-41 Scenarios in which the tautomer couples anti-ferromagnetically to: i) cobalt , ii) permalloy or iii) neither metal. Based on the behavior shown in Fig. IV-17, scenario i.) is the one observed. Only the downward sweeping magnetic field is shown.

Additionally, the existence of the rectification effect itself means that the tautomer is sensitive to the presence of an electric field in a way that affects its spin dependent states. As discussed above in the I-V section, it was determined that the bias itself can affect the position of the switching fields, as shown in Fig. IV-30. It was not clear from the MR measurements whether the positive bias or the negative bias was causing the switching field to move inwards

towards zero, which based on the AF coupling discussed in the section, indicates a conversion to the high spin state. The toggling of the positive and negative biases happens too quickly to separate the effects. It is known that a converted state will tend to persist because the states themselves are sluggish and hysteretic as seen in the plots, in particular Fig. IV-27.

From the I-V measurements, it did appear that the positive bias was causing the switching fields to switch out, away from zero, and the negative bias was causing the switching fields to switch in towards zero. If such an effect is indeed occurring, this is evidence of electric field control over the tautomeric conversion. Such a control has been theorized in the literature to be a result of the Stark effect.[5] However, other mechanisms could be controlling this conversion behavior, including simple charge transfer as a result of the conduction. More studies will be needed to determine the exact nature of the conversion process.

Conclusion

In summary, a spin valve has been made from a valence tautomer. The magnetotransport behavior of the spin valve is controlled by the tautomeric state. A change in the magnetotransport has been observed to be a function of temperature and light. In the valence tautomer high-spin state, the MR is observed to occur in a window that overlaps zero magnetic field with symmetric switching fields on either side of zero, for both the down and the up magnetic field sweep. When the valence tautomer is in the low-spin state, the switching fields shift or separate and move away from zero, so that there are two distinct MR windows for the down and up magnetic field sweeps. The shifting of the fields can be controlled by

temperature and light, indicating it is a tautomeric behavior. It is believed to be a result of the tautomer anti-ferromagnetically coupling to the cobalt electrode.

Results at 4K confirmed intermolecular anti-ferromagnetic coupling which was expected for the tautomer. The spin valve demonstrated AF behavior at this low temperature. A high applied bias also drove the valve into the low-spin state.

Another feature of the tautomer acting in the interlayer of the spin valve is that there is rectification of the spin transport by the applied bias direction. A parallel resistors model showed that this is an indication of a spin-dependent layer controlled by the direction of the electric field. This implies the valence tautomer has a field-controllable spin-dependence.

It was also shown that the applied bias could control the shifting of the switching fields. It appeared that a positive bias could drive conversion to the low-spin state, whereas a negative bias was driving conversion to the high-spin state. This is possibly the result of charge transfer due to the applied bias or the Stark effect where the electric field has aligned with a preferred crystallographic orientation in the valence tautomer and is driving the transition between low-spin and high-spin.

Tautomeric control over the magnetotransport in a spin valve is a novel result and has never been observed before. Future studies can be designed to better examine the effect of the electric field. The abundance of effects may lead to possible new devices which exploit the new behaviors, especially if molecular transition speeds can be improved possibly by modifications to the device or molecular structure.

Chapter V: Summary and Conclusion

Two unique molecules with characteristics showing promise for use in metal-molecule-metal structures designed for organic electronic and molecular spintronics applications were examined for their transport and magnetotransport behaviors. The design of the metal-molecule-metal structures made it possible to conduct measurements revealing the intrinsic behaviors of the molecules. These intrinsic transport behaviors have not been reported before by any previous experiments. In both molecule-based systems, the findings matched and confirmed some prior theoretical expectations. The findings build a foundation for novel devices to advance the fields of organic electronics and molecular spintronics.

V.1. Alkanedithiols

Alkanedithiols of varying lengths were made into a self-assembled monolayer to act as an insulating barrier layer in a metal-molecule-metal junction. For the formation of the top electrode, a novel method of nanotransfer printing was used. The nTP method is reproducible, stable and does not damage the molecules. The resulting interface of the metal electrode with the molecule makes it possible to explore the transport behavior of the alkane molecular chain and metal-molecule bond of the thiol end group. The MMM junctions produce symmetrical I-V behavior, indicating the nTP interface is identical to the metal-molecule interface beneath the monolayer. Analysis of I-Vs collected by cAFM was performed using the Simmons model. A statistical approach was developed to overcome convergence limitations of the fitting

algorithm in reaching a chi-square minimization to obtain the tunneling barrier parameters. This analysis revealed quantitative tunneling parameters for the molecules, including the tunneling barrier heights, 3.5 ± 0.2 eV (alkane) and 2.4 eV (an upper bound value for thiol), and the corresponding decay coefficients, 1.16 $\pm$ 0.10 $Å^{-1}$ (alkane) and 1.00 $\pm$ 0.14 $Å^{-1}$ (thiol). These values are consistent with theoretical predictions. However, the alkane barrier height and the thiol decay coefficient are higher than those previously observed by other techniques which use different methods for creating electrodes. It is believed the improved interfacial quality between the SAM and the top printed Au electrode using the nTP process enables these more intrinsic measurements.

NTP electrodes could be made to vary in size with results consistent with scaling of resistances. Areas for the top contacts ranged from 80nm to 7 microns. It was determined that the resistances for the varying pad sizes scaled with an effective contact area instead of the actual contact area when the pad sizes exceeded lateral dimensions of hundreds of nanometers. This microscopic effective contact area is produced as a function of the tapping force of the nTP method, the roughness of the electrodes and mechanical properties of the stamps used.

V.2. Cobalt-based Valence Tautomers

Cobalt based valence tautomers were used in developing a magnetically activated spin valve because of their unique capability to transition between two distinct magnetic states as a function of temperature, pressure and light. At high temperature above the molecular

transition of approx.. 150K-180K as observed by SQUID measurements of polycrystalline samples, the molecule is paramagnetic in a high-spin Co(II) form with five unpaired electrons (S=5/2). At low temperature, the molecule is diamagnetic in a low-spin Co(III) form with a single unpaired electron (S=1/2). The transition is driven by entropy resulting from the greater density of states in the high-spin form, and takes place because of an intramolecular ligand-metal charge transfer coupled with a metal-based spin-crossover.

The spin valve was made from a spin-coated valence tautomer intermediate layer. Valves were observed to exhibit magnetoresistance as high as 1%. The magnetotransport behavior of the spin valve is controlled by the tautomeric state. A change in the magnetotransport has been observed as a function of temperature and light. When the VT is in its high-spin state, the MR is observed to occur, in a magnetic field sweep from a maximum, before the field has reached zero magnetic field and changed polarity. The valve exhibits symmetric switching fields, with the anti-parallel alignment windows overlapping on either side of zero, for both magnetic field sweep directions.

In contrast, when the valence tautomer is in the low-spin state, the switching fields have shifted or separated away from zero, so that there are two distinct MR windows for the down and up magnetic field sweeps. The shifting of the fields can be controlled by increasing or decreasing the temperature through the tautomeric transition temperature, or by illuminating the spin valve with light, indicating the magnetotransport change is the result of tautomeric behavior. Specifically, it is believed that the tautomer is anti-ferromagnetically coupling to the cobalt electrode in its high-spin form as a result of the five unpaired electrons.

Results at 4K confirmed intermolecular anti-ferromagnetic coupling which was expected for the tautomer based on prior SQUID measurements in this range. The spin valve demonstrated AF behavior at this low temperature. A high applied bias also drove the valve into the low-spin state.

Another feature of the tautomer acting in the interlayer of the spin valve is that there is rectification of the spin transport as a function of the applied bias direction. A parallel resistors model showed that this is an indication of a spin-dependent layer. In this case, the interlayer is controlled by the direction of the electric field. It was also shown that the applied bias could control the shifting of the switching fields. It appeared that a positive bias could drive conversion to the low-spin state, whereas a negative bias was driving conversion to the high-spin state.

Tautomeric control over the magnetotransport in a spin valve is a novel result and has never been observed before. The diversity of the effects observed, specifically the spin rectification effect and the shifting of the MR window, have great potential for the design and construction of useful applications in molecular spintronics.

References

1 Schmidt, R. D. Investigation of the Electronic and Magnetic Properties of Electron Exchange: Exchange Coupled Donor-Bridge-Acceptor Biradicals and Novel Magnetic Behaviors of Bis(pyridyl) Cobalt Dioxolene Valence Tautomers. *PhD Thesis* (2010).

2 Dediu, V., Murgia, M., Matacotta, F., Taliani, C. & Barbanera, S. Room temperature spin polarized injection in organic semiconductor. *Solid State Communications* **122**, 181-184, doi:10.1016/S0038-1098(02)00090-X (2002).

3 Li, B., Kao, C., Yoo, J., Prigodin, V. & Epstein, A. Magnetoresistance in an All-Organic-Based Spin Valve. *Advanced Materials* **23**, 3382-+, doi:10.1002/adma.201100903 (2011).

4 Li, B. *et al.* Room-temperature organic-based spin polarizer. *Applied Physics Letters* **99**, doi:10.1063/1.3651329 (2011).

5 Droghetti, A. & Sanvito, S. Electric Field Control of Valence Tautomeric Interconversion in Cobalt Dioxolene. *Physical Review Letters* **107**, doi:10.1103/PhysRevLett.107.047201 (2011).

6 Shultz, D. A. Valence Tautomerism in Dioxolene Complexes of Cobalt. In Magnetism: Molecules to Materials II, Miller, J. S.; Drillon, M., Eds. Wiley-VCH: New York, 2001; Vol. 2, pp 281-306.

7 De Teresa, J. *et al.* Role of metal-oxide interface in determining the spin polarization of magnetic tunnel junctions. *Science* **286**, 507-509, doi:10.1126/science.286.5439.507 (1999).

8 Xiong, Z., Wu, D., Vardeny, Z. & Shi, J. Giant magnetoresistance in organic spin-valves. *Nature* **427**, 821-824, doi:10.1038/nature02325|10.1038/nature02325 (2004).

9 Barraud, C. *et al.* Unravelling the role of the interface for spin injection into organic semiconductors. *Nature Physics* **6**, 615-620, doi:10.1038/NPHYS1688 (2010).

10 Jonsson-Akerman, B. *et al.* Reliability of normal-state current-voltage characteristics as an indicator of tunnel-junction barrier quality. *Applied Physics Letters* **77**, 1870-1872 (2000).

11 Zhang, Z. & Rabson, D. Electrical and thermal modeling of the non-Ohmic differential conductance in a tunnel junction containing a pinhole. *Journal of Applied Physics* **95**, 557-560, doi:10.1063/1.1633341|10.1063/1.1633341 (2004).

12 Szulczewski, G., Sanvito, S. & Coey, M. A spin of their own. *Nature Materials* **8**, 693-695, doi:10.1038/nmat2518 (2009).

13 Miller, O., Muralidharan, B., Kapur, N. & Ghosh, A. Rectification by charging: Contact-induced current asymmetry in molecular conductors. *Physical Review B* **77**, doi:10.1103/PhysRevB.77.125427|10.1103/PhysRevB.77.125427 (2008).

14 Wagemans, W., Bloom, F., Bobbert, P., Wohlgenannt, M. & Koopmans, B. A two-site bipolaron model for organic magnetoresistance. *Journal of Applied Physics* **103**, doi:10.1063/1.2828706|10.1063/1.2828706 (2008).

15 Tran, L. A., Le, Q. T., Sanderink, J. G. M., van der Wiel, W. G. & de Jong, M. P. The Multistep Tunneling Analogue of Conductivity Mismatch in Organic Spin Valves. *Advanced Functional Materials* **2012** (2012).